# Impact of Space Weather Events on the Orbit of Low Earth Orbiting Satellites

Bachelor Thesis
Faculty of Science
University of Bern

**Levin Walter**
2024

*Supervised by*
Prof. Dr. Adrian Jäggi, Dr. Daniel Arnold,
Vanessa-Maria Mercea, Prof. Dr. Lucia Kleint
Astronomical Institute

# Erklärung

gemäss Art. 30 RSL Phil.-nat.18

Name/Vorname: Walter Levin

Matrikelnummer: 21-128-509

Studiengang: Physik

Bachelor ☑ Master ☐ Dissertation ☐

Titel der Arbeit: Impact of Space Weather Events on the Orbit of Low Earth Orbiting Satellites

LeiterIn der Arbeit: Prof. Dr. Jäggi Adrian

Ich erkläre hiermit, dass ich diese Arbeit selbständig verfasst und keine anderen als die angegebenen Quellen benutzt habe. Alle Stellen, die wörtlich oder sinngemäss aus Quellen entnommen wurden, habe ich als solche gekennzeichnet. Mir ist bekannt, dass andernfalls der Senat gemäss Artikel 36 Absatz 1 Buchstabe r des Gesetzes vom 5. September 1996 über die Universität zum Entzug des auf Grund dieser Arbeit verliehenen Titels berechtigt ist.
Für die Zwecke der Begutachtung und der Überprüfung der Einhaltung der Selbständigkeitserklärung bzw. der Reglemente betreffend Plagiate erteile ich der Universität Bern das Recht, die dazu erforderlichen Personendaten zu bearbeiten und Nutzungshandlungen vorzunehmen, insbesondere die schriftliche Arbeit zu vervielfältigen und dauerhaft in einer Datenbank zu speichern sowie diese zur Überprüfung von Arbeiten Dritter zu verwenden oder hierzu zur Verfügung zu stellen.

Bern, 27.11.2024

Ort/Datum

Unterschrift

## Abstract

Coronal mass ejections (CME) from the Sun can cause geomagnetic storms which cause the thermosphere to expand. This leads to enhanced air drag for satellites in low Earth orbit (LEO). This work analyses the evaluation of orbital decay with a focus on selected geomagnetic storm events. Using the Bernese GNSS Software (BSW), reduced-dynamic orbits of different LEO satellites are computed from GNSS data of on-board receivers, where non-gravitational accelerations are modelled by means of estimated empirical piecewise-constant accelerations (PCA). The orbital decay is then calculated by using the PCAs, or, in case of the Gravity Recovery and Climate Experiment Follow-On (GRACE-FO) satellites, calibrated accelerometer data, to solve Gauss's perturbation equation for the satellite's semi-major axis. This method is compared to an approach where a fit model is applied to the osculating semi-major axis derived from the reduced-dynamic orbits computed by BSW. The fit model consists of a piece-wise linear model of the time-varying mean orbital decay and the time-varying amplitudes of the most dominant periodic oscillations. The results of both methods are compared and found to be similar for large orbital decays induced by CMEs. The fit model is not able to produce results of adequate quality when dealing with low orbital decays. Moreover, large orbital decay induced by a geomagnetic storm is underestimated by the fit model due to constraining. The Gaussian perturbation equation method can register changes in orbital decay more accurately than the fit model and can react, e.g., quasi-instantaneously to satellite manoeuvres which change the semi-major axis. For satellites equipped with an on-board GNSS receiver but without an on-board accelerometer, PCAs can be estimated and used for the numerical integration. For both methods improvement is possible.

With the Gaussian approach the resulting maximum smoothed orbital decay reached during the geomagnetic storm on 2018-08-26 for GRACE-FO-1 is $-7.35\,\mathrm{m\,d^{-1}}$ when PCAs are used and $-7.51\,\mathrm{m\,d^{-1}}$ when ACC data is used. During the extreme geomagnetic storm starting on 2024-05-10 the maximum smoothed orbital decay obtained with the Gaussian approach with PCAs is $-224.20\,\mathrm{m\,d^{-1}}$ for Swarm-A, $-29.51\,\mathrm{m\,d^{-1}}$ for Sentinel-2A and $-26.99\,\mathrm{m\,d^{-1}}$ for Sentinel-3A.

# Contents

# 1 Introduction

In this work the orbital decay of satellites in low earth orbit (LEO) is studied. With the Bernese GNSS Software (Dach et al., 2015, BSW), reduced-dynamic (RED-DYN) orbits represented by osculating orbital elements for different LEO satellites are determined using Global Navigation Satellite System (GNSS) code and carrier phase measurements. Estimated empirical piecewise constant accelerations (PCA) as well as calibrated accelerometer data from the GRACE-Follow-On (GRACE-FO) mission are used to numerically solve Gauss's perturbation equations to propagate the osculating orbital elements. With this approach, it is possible to precisely evaluate the decrease in the semi-major axis due to the used accelerations representing the non-gravitational accelerations like air drag, solar and Earth radiation pressure. This method is compared with the procedure in which the decrease is evaluated by differentiating a fit model, which is applied to the time series of the osculating semi-major axis obtained from the estimated orbits using the BSW. BSW estimates the orbits with code and carrier phase measurements and the impact of the gravitational and non-gravitational forces is both reflected by the osculating elements.

If an interplanetary coronal mass ejection (CME) with particular characteristics hits the Earth, it influences properties of the thermosphere. This in turn changes the orbital decay of a LEO satellite due to air drag. Thus, in this work, there is a focus on increased orbital decay of LEO satellites due to CME events. In addition, the orbital decay is compared with the *ap* index, the modelled air density at the corresponding LEO height, and the $\beta$ angle. The *ap* index contains information about geomagnetic activity. The air density is explicitly modelled in orbits when other non-gravitational forces are modelled as well, and the $\beta$ angle is the angle between the orbital plane of the LEO satellite and the direction to the Sun.

The goal of this thesis is to evaluate the performance of the two aforementioned methods used to assess the orbital decay of LEO satellites with a focus on geomagnetic storm events. For the Gauss's perturbation equation approach, a comparison between the results obtained with the GRACE-FO accelerometer data and the PCAs is conducted. Because both gravitational and non-gravitational forces are impacting the satellites, they influence the osculating elements obtained from the estimated orbits by BSW. Thus, the recovery of orbital decay from the osculating semi-major axis time series is more difficult with the fit model approach.

## 1.1 Space Weather

A 1995 issue of the US National Space Weather Program, *The Strategic Plan of Space Weather*, defines space weather as "conditions on the Sun and in the solar wind, magnetosphere, ionosphere and thermosphere that can influence the performance and reliability of space-borne and ground-based technological systems and can endanger human life or health" (Miteva et al., 2023). Solar activity is the appearance and dispersal of closed and open magnetic field regions on the Sun. Solar activity varies according to the solar cycle and can be measured with the sunspot number and the radio flux at 10.7 cm wavelength (Gopalswamy, 2022). The solar cycle exhibits a period of 11 years (Stix, 2002), during which a phase of solar maximum and a phase of solar minimum occurs. The occurrence rate of solar flares and CMEs is highly correlated with solar activity (Gopalswamy, 2022).

The main drivers of space weather are:

- Solar flares, due to their electromagnetic emissions;
- CMEs, due to their interaction with Earth's magnetic field;
- High-speed streams, in the form of co-rotating interaction regions and streaming interaction regions;
- Solar energetic particles, in the form of protons, electrons and heavy ions, that originate from solar flares and CMEs (Miteva et al., 2023).

CMEs as well as solar flares are explosive events that mostly occur in active regions. Active regions are regions on the Sun of enhanced and complex magnetic field (Stix, 2002). CMEs and solar flares occur more during solar maximum because there are more active regions. Active regions often contain sunspots. At first, photospheric motions store energy in the magnetic field of the active region, which is later on released explosively (Gopalswamy, 2022). Solar flare photons range from X-rays to UV to visible light (Buzulukova and Tsurutani, 2022). White-light coronagraphs and extreme ultraviolet (EUV) imagers are used to detect and observe CMEs on the Sun (Gopalswamy, 2022). Properties of CMEs and their interaction with Earth's magnetosphere are discussed in more detail in Sect. 1.1.1.

Solar flare emission causes the ionosphere to heat and expand. Ionospheric disturbances impact satellite work performance by delaying, distorting and absorbing radio signals during propagation. Thus, the quality of satellite communication, navigation and positioning is affected. Radio blackouts may occur as well during solar flare emission. Air traffic control problems in Sweden on 2015-11-04 are an example when radar systems were affected by solar flare emission (Miteva et al., 2023).

A high-speed stream is solar plasma that escapes from coronal holes where the magnetic field lines are open (Stix, 2002). Apart from high-speed streams there is the ambient solar wind, that originates from the Sun's corona and which is a continuous stream of particles. The high-speed streams interact with the ambient solar wind, creating streaming interaction regions and co-rotating interaction regions (Gopalswamy, 2022).

Figure 1 shows the Sun on 2024-05-11 at 00:59 UTC before and during the X-class flare at 01:22 UTC. The pictures are taken with the Atmospheric Imaging Assembly (AIA) onboard the Solar Dynamics Observatory (SDO) with a 193 Å filter. The large black shape on the upper right part of the Sun is a coronal hole and the bright spots on the lower right are located in an active region (a sunspot group is located at this location).

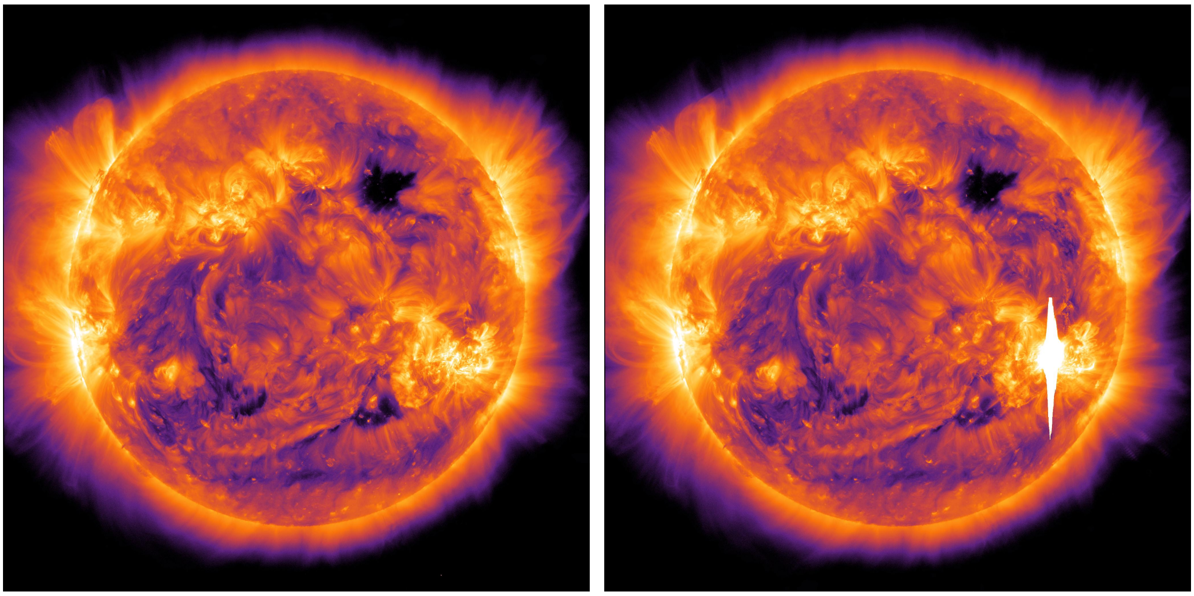

Figure 1: The Sun seen with a 193 Å filter at 2024-05-11 at 00:59:52:843 UTC (left) and at 01:22:40:843 UTC (right). Images are taken with the AIA instrument onboard of SDO and recoloured (image courtesy: Helioviewer.org, accessed on 2024-08-02).

Solar energetic particles pose a hazard to satellite components/material and software. Iucci et al. (2005) show that the severity of hazardous effects depends on the orbit of the satellite. Relativistic electrons can precipitate at the auroral zones to lower altitudes which are crossed by LEO satellites with a high inclination orbit. Possible effects due to solar energetic particle radiation are (Miteva et al., 2023)

- single-event upsets / single-event effects (for example bitflips),
- cumulative radiation effects,
- surface discharges,
- deep dielectric charging and
- solar cell degradation, material aging / surface damage to materials.

An example that demonstrates the danger of solar energetic particles took place on 2002-04-21. A powerful eruption lead to a solar energetic particle event that damaged the communications and power systems of the Nozomi spacecraft. This led to a series of issues that ended the mission without it reaching its

destination Mars (Gopalswamy, 2022).
Another example is linked to the Mars Odyssey mission. The Martian Radiation Environment Experiment was a dedicated energetic charged particle spectrometer onboard the Mars Odyssey mission. When the Halloween solar energetic particle event on 2003-10-28 started, the spacecraft went into a safe mode. When the spacecraft came out of the safe mode, the spectrometer was non-responsive and all attempts to revive the instruments were unsuccessful leading to the instruments abandonment (Gopalswamy, 2022).

### 1.1.1 CMEs and Geomagnetic Storms

Typical CMEs travel at speeds ranging from a few hundreds to a few thousands of kilometres per second. A CME's size expands as it propagates from the Sun through the interplanetary medium and can reach widths of more than 0.5 AU by the time it reaches Earth. As the CME interacts with the interplanetary medium its shape is altered (Buzulukova and Tsurutani, 2022).

CMEs can exhibit different characteristics. Relevant for this study are CMEs that are *geoeffective*, which means that they cause geomagnetic storms upon reaching Earth (Gopalswamy, 2022). A geomagnetic storm ensues when an interplanetary structure contains a southward magnetic field component $B_z < 0$. If such a magnetic field encounters the magnetic field of the Earth, the two magnetic fields undergo a process known as magnetic reconnection (Buzulukova and Tsurutani, 2022; Gopalswamy, 2022). First, a dayside reconnection takes place, which drags the newly reconnected magnetic field lines over the poles to the nightside. Magnetic energy is then stored in the magnetotail until it is explosively released in another magnetic reconnection event, causing the reversed plasma motion from the nightside to the dayside. The stored energy is then released explosively in so called *geomagnetic substorms*. This way, particles are injected into the magnetosphere which enhances the ring current (see also Sect. 1.1.2). This process is known as the Dungey convection cycle (Branduardi-Raymont et al., 2021; Buzulukova and Tsurutani, 2022; Dungey, 1961; Gopalswamy, 2022). For more information about magnetic reconnection see Eastwood et al. (2015), Pontin and Priest (2022) and Koskinen (2011).

Geomagnetic substorms are associated with bright auroral displays in polar regions (Branduardi-Raymont et al., 2021). Substorms are related to the buildup/release of magnetic energy. They are lower in intensity than CME storms. It is worth mentioning that co-rotating interaction regions can induce auroral substorms (Buzulukova and Tsurutani, 2022).

Most geoeffective CMEs exhibit a five part structure. Figure. 2 shows an example of a CME where the five part structure is distinguishable as previously done in Gopalswamy (2022). There is the *bright core* which is the eruptive prominence. Ahead of the bright core is the *dark void* which is interpreted as the magnetic flux rope. The outward motion of the dark void compresses coronal material ahead of it, which is visible as the *bright front* (Gopalswamy, 2022). Compressive waves are launched if there are sudden changes in plasma motion. If the motion occurs faster than the characteristic speed of the medium, the waves will develop into a shock wave. This *shock* is a propagating compression of density (and magnetic field if applicable) (Vourlidas et al., 2013). As the shock wave propagates, a shock *sheath* is formed behind, which consists of the ambient plasma compressed by the shock. Its temperature, density, and magnetic field strength are all higher than those in the ambient medium (Gopalswamy, 2022). The shock and the sheath can be best seen in a difference image (difference between images taken at different epochs) (Gopalswamy, 2022). Distant streamer deflections are a reliable but indirect proxy for shock waves (Vourlidas et al., 2013). Shock sheaths can be best seen if the difference image is displayed with high contrast (Vourlidas et al., 2013).

In Fig. 2 three images are shown, each with superimposed (at the same position in each image) coloured arrows to indicate various structures of the CME. The left coronagraph image is taken before the bright front reaches the occulting disk with only a couple of streamers being visible. The bright core, dark void and the bright front of the CME are visible in the image in the middle. In this image, the left upper streamer is visibly extended (deflected) from the base up to the green arrow, which is caused by the shock. At the location where the green arrow points to, the streamer has a small kink, which marks the presence of the shock. On the right is a processed (contrast, brightness and gamma correction) image produced by taking the difference of the other two images. The lower part of the streamer that is deflected is now visible as white space, indicated by the blue arrow. Between the two red arrows a new layer becomes visible, which is less bright than the rest of the CME but brighter than the background. This is the shock sheath. The outer edge of the sheath can be interpreted as the shock itself. It should be noted that the propagation direction of the CME is slightly inclined towards the viewer, hence the shock sheath does not surround the bright front in a circular manner. The images are taken with the C2 coronagraph of the Large Angle and Spectrometric Coronagraph (LASCO) onboard the Solar and Heliospheric Observatory (SOHO) satellite.

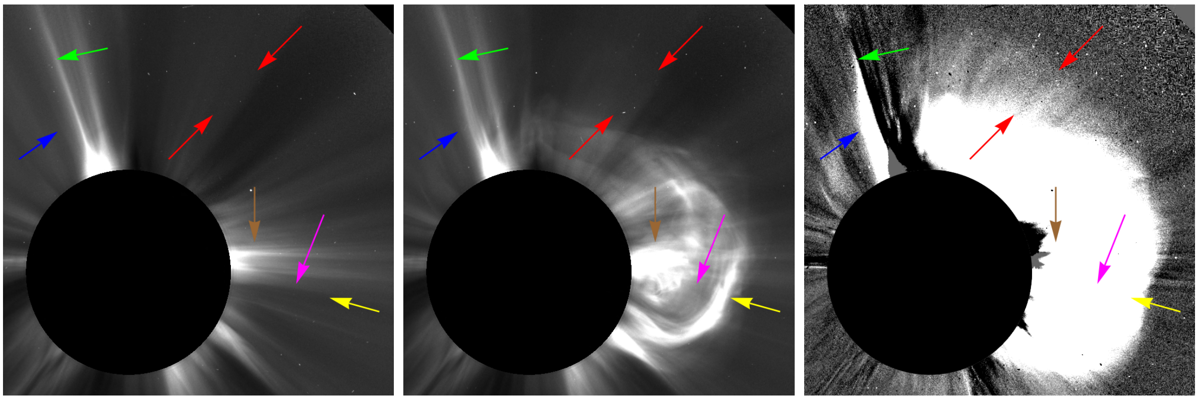

Figure 2: White-light images from the SOHO LASCO C2 coronagraph on 2023-02-25 at 19:24:07:448 UTC (left) and at 20:00:07:422 UTC (middle) and the processed difference image (right), all with superimposed arrows. The green arrow points to the position of the kink in the streamer. The blue arrow points to the lower part of the streamer that gets diffused by the shock wave. The red arrows indicate the region where the shock sheath is visible in the difference image. The brown arrow highlights the bright core of the CME. The magenta arrow shows the dark void structure in the CME. The yellow arrow highlights the bright front. (Image courtesy of the first two images: Helioviewer.org, accessed on 2024-08-23. The third image was produced by the author with Wolfram Mathematica 14.0.0.0.)

The shock sheath and the flux rope are the structures that are able to cause geomagnetic storms as they contain a magnetic field. Based on the helicity and the orientation of the flux rope, not the entire structure may be geoeffective. For example, if both the sheath and the backside of the flux rope contain a negative $B_z$ value, a two-step storm may ensue. Figure 3 is a sketch showing a magnetic cloud containing a flux rope from two perspectives. In this sketch only the front half of the flux rope contains a negative $B_z$ value. According to Kilpua et al., 2017, this would be a left handed bipolar flux rope with south-east-north orientation and slight inclination.

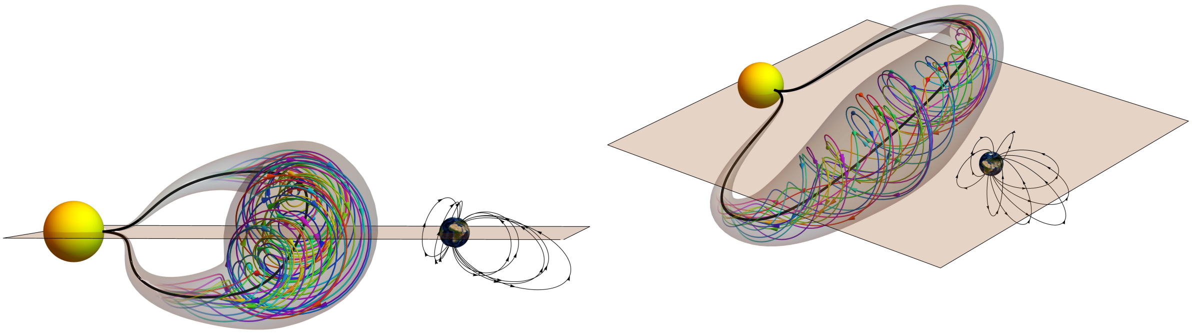

Figure 3: Two sketches showing a flux rope inside a magnetic cloud from two perspectives. The magnetic field lines of the flux rope are winded around the flux rope axis (thick black curve). The flux rope is slightly inclined relative to the reference plane. (The images were produced by the author with Wolfram Mathematica 14.0.0.0.)

Interplanetary CMEs (ICMEs) can be detected based on a variety of signatures. It should be noted that the signatures at 1 AU are highly dependent on the observation geometry. Commonly used proxies are low proton temperature, low plasma beta, increase in magnetic field strength and coherent rotation of the magnetic field components. Plasma beta is the ratio of thermal plasma pressure to magnetic pressure. However, suboptimal positioning against the measuring instrument may lead to the magnetic cloud properties not being detected. In this case additional proxies may be used to assess CME arrival such as the decrease of solar wind speed and the Forbush decrease, which is a transient reduction in galactic cosmic ray intensities due to the magnetic field of a CME. For more information about CME signatures and properties see Kilpua et al., 2017.

A southward magnetic field is necessary for a geomagnetic storm and the strength of the storm depends on solar wind parameters such as the speed and the dynamic pressure (Gopalswamy, 2022). $B_z$ and the solar wind velocity are the main factors contributing to the energy input into Earth's magnetosphere (Buzulukova and Tsurutani, 2022).

A geomagnetic storm increases magnetospheric convection, which causes an increase of energy input into the coupled thermosphere - ionosphere system. Through collisions, ionospheric plasma interacts with neutrals, therefore ionospheric currents generate Joule heating (Buzulukova and Tsurutani, 2022). If the upper atmosphere expands, the occurrence of collisions between spacecraft and neutral particles increases. This atmospheric drag effect leads to a gradual reduction of the altitude of the spacecraft. During intense magnetic storms a loss of spacecraft track may occur. An example for this is the temporary (few days) loss of $1,000$ satellites after five days during the geomagnetic storm of March 1989 (Buzulukova and Tsurutani, 2022).

Another example showing the importance of understanding how geoeffective CMEs influence the atmosphere is the "SpaceX" storm in 2022. Two CMEs each triggering a geomagnetic storm enhanced the density of the atmosphere on 2022-02-03 and 2022-02-04. The increased atmospheric drag aided in the de-orbitation of 38 of 49 previously launched Starlink satellites of SpaceX at an altitude of 210 km (Dang et al., 2022).

Unpredictable increase in satellite drag increases the risk of collisions with other satellites or space debris. This could set off the Kessler effect (Kessler and Cour-Palais, 1978), in which each subsequent collision produces more fragments and thus increases the risk of further collisions (Buzulukova and Tsurutani, 2022). It is thus important to be able to maintain the tracking of satellites and to be able to predict increased satellite drag induced by geomagnetic storms.

### 1.1.2 Geomagnetic Indices

During a prolonged interval (a few hours) of southward $B_z$, a torus-like region of enhanced fluxes of $H^+$, $O^+$ and electrons forms. These particles drift around Earth due to the magnetic field curvature and magnetic field gradient drifts, forming a *ring current* flowing in the space around the Earth. The ring current disturbs the magnetic field strength, which can be detected at the Earth's surface. The disturbance is usually less than 1%. It has a characteristic time dependence and can be detected by ground-based magnetometer stations in a wide range of longitudes, lasting a few hours and then recovering slowly over one half to several days. The disturbance storm-time or $Dst$ index is the measurement of the ring current disturbance at low geomagnetic latitudes (Buzulukova and Tsurutani, 2022).

With the $K$ index, the disturbance in the horizontal component of Earth's magnetic field is quantified. It is derived from the maximum fluctuations of the horizontal components during a three-hour interval. The mean standardised $K$ index from thirteen geomagnetic observatories is called the planetary three-hour-range index $Kp$. The $K$ index takes on values from 0 to 9 according to a quasi-logarithmic scale, which is station-specific. This is done in an attempt to normalise the frequency of occurrence of the different magnitudes of disturbances (gfz-potsdam.de accessed on 2024-08-24). The $A$ index was invented because there is no linear relationship between the $K$ scale and magnetometer fluctuations. Instead the $K$ index is converted back into a linear scale called the "equivalent three-hourly range" $a$ index (for this index upper case letters describe daily indices as in averages of the eight three-hourly indices, which are denoted with lower case lettters). The $Ap$ index is derived from the $Kp$ index in an analogous way. Each individual three-hourly $Kp$ index is converted to an equivalent amplitude three-hourly $ap$ index. To calculate the daily $Ap$ index the average of the eight three-hourly $ap$ indices is calculated (swpc.noaa.gov accessed on 2024-08-24). The possible values for $ap$ lie between 0 and 400. Moreover the $ap$ indices are denoted with an index that indicates the three hours. For example, $ap_2 = 27$ means that between 3 AM and 6 AM (the second three-hour interval in a day) the $ap$ index has a value of 27.

The Auroral Electrojet ($AE$) index is a measure of global electrojet activity in the auroral zone (wdc.kugi.kyoto accessed on 2024-09-06). Because the orbit of the satellites analysed in this work are all polar, this index is also used in this work.

## 1.2 LEO Satellites

A LEO is generally defined as an orbit with an altitude lower than 2,000 km. Because of the low orbital height, the perturbative effects of Earth's gravitational field, as well as non-gravitational effects such as air drag and solar and Earth radiation pressure are important to take into account for precise orbit determination (POD). Orbit perturbations are discussed in more detail in Sect. 2.2.3.

In this work, the orbits of the satellites GRACE-FO-1, Swarm-A (Friis-Christensen et al., 2008), Sentinel-1A (Torres et al., 2012), Sentinel-2A (Drusch et al., 2012) and Sentinel-3A (Donlon et al., 2012) are analysed. All satellites are in high inclination orbits. Moreover, the orbits of the Sentinel satellites are all sun-synchronous, which means that the orbit precession rate is one revolution per year. All satellites are equipped with GPS receivers and star trackers (earth.esa.int accessed on 2023-08-25, gracefo.jpl.nasa.gov accessed on 2023-08-25, sentiwiki.copernicus.eu accessed on 2023-08-25, Jäggi et al., 2024). The GPS receivers allow for POD via GPS satellites. For every satellite the data from the star tracker cameras is used for attitude modelling.

The GRACE-FO (Landerer et al., 2020) satellites are each equipped with a 3-axes accelerometer, which measures non-gravitational accelerations acting on the satellite. Accelerations in the cross-track axis are measured with a lower sensitivity than accelerations in radial and in along-track direction. The Swarm-A satellite also has an onboard accelerometer, but it is not used due to low accuracy and frequent data problems (Bezděk et al., 2018).

The altitude of the Sentinel satellites is frequently corrected with manoeuvres (MAN) (sentiwiki.copernicus.eu accessed on 2023-08-25). MANs are also performed on GRACE-FO-1 and Swarm-A but not on a frequent basis. During the analysed time intervals no MANs are performed by these satellites.

In Tab. 1 the range of the semi-major axis, the inclination and the properties of all the analysed satellites are summarised. The altitude of GRACE-FO-1 ranges from 482 km to 501 km in the analysed time interval in 2018 and it ranges from 476 km to 497 km in the analysed time interval in 2023. The altitude of Swarm-A ranges from 445 km to 468 km in the analysed time interval in 2023 and it ranges from 457 km to 477 km in the analysed time interval in 2024. Sentinel-1A is operated at an altitude of about 695 km. The operation altitude of Sentinel-2A is about 785 km and in the case of Sentinel-3A it is about 800 km.

Table 1: Summary of the important properties of each satellite analysed in this work.

| Satellite | Interval range of Semi-major axis | Inclination | Sun-synch.? | Accelerometer? | Freq. MANs? |
|---|---|---|---|---|---|
| GRACE-FO-1 | [6,860, 6,879] km (2018)<br>[6,854, 6,875] km (2023) | 89° | × | yes | no |
| Swarm-A | [6,823, 6,846] km (2023)<br>[6,835, 6,855] km (2024) | 87.35° | × | yes, but not used | no |
| Sentinel-1A | [7,062, 7,080] km (2023) | 98.18° | ✓ | no | yes |
| Sentinel-2A | [7,155, 7,173] km (2024) | 98.62° | ✓ | no | yes |
| Sentinel-3A | [7,169, 7,187] km (2024) | 98.65° | ✓ | no | yes |

GNSS high-low satellite-to-satellite (hl-SST) tracking allows cm-precise orbit determination (Mao et al., 2021). In the POD both the code measurements and the phase measurements are used. For more information about the process of POD see Jäggi (2007).

# 2 Theory

## 2.1 Equation of Motion

In the gravitational two-body problem the motion of two point masses are analysed. The equation of motion of a satellite in the two-body problem in the quasi-inertial geocentric coordinate system reads:

$$\ddot{\vec{r}}(t) = -\gamma \frac{\vec{r}(t)}{|\vec{r}(t)|^3}, \tag{1}$$

where $\gamma$ is the gravitational constant $G$ multiplied with the mass of the Earth $M_{\text{Earth}}$ and $\vec{r}$ is the position vector of the satellite. If at an epoch $t_0$ the initial values

$$\vec{r}(t_0) \doteq \vec{r}_0 \tag{2}$$

$$\dot{\vec{r}}(t_0) \doteq \vec{v}_0 \tag{3}$$

are known, the trajectory is uniquely defined. Equations (2) and (3) amount to six initial conditions in total. The trajectory is a conic section. For bounded satellite orbits only ellipses are relevant. The main celestial body is located in one of the two focal points of the ellipse. Thus, an alternative to the initial values (2) and (3) are the six Keplerian elements $\{a, e, i, \Omega, \omega, u_0\}$, which describe the position of the satellite on the ellipse as well as the size, shape and orientation of the ellipse:

$$\{\vec{r}_0, \vec{v}_0\} \quad \longleftrightarrow \quad \{a, e, i, \Omega, \omega, u_0\} \tag{4}$$

The six Keplerian elements used in this work are:

1. $a$: Semi-major axis of the ellipse - describes the size of the ellipse.
2. $e$: Numerical eccentricity of the ellipse - defines the shape of the ellipse.
3. $i$: Inclination of the ellipse with respect to a reference plane - in this case the Earth's equatorial plane is the reference plane.
4. $\Omega$: Right ascension of ascending node - it is the angle between a reference direction (here the vernal equinox) and the ascending node. The ascending node is the point where the satellite crosses the reference plane in the ascending direction.
5. $\omega$: Argument of perigee - describes the angle between the ascending node and the perigee, which is the point where the satellite is closest to the Earth.
6. $u_0$: Argument of latitude at time $t_0$ - describes the angle between the ascending node and the satellite position on the ellipse at time $t_0$.

The argument of latitude $u$ is time dependent. For the initial value problem at epoch $t_0$ the corresponding $u(t_0) \doteq u_0$ is used.

Figure 4 illustrates the orbit of a satellite in a Cartesian coordinate system from two viewpoints. The reference plane is the $x$-$y$-plane and the $x$-axis is the reference direction for the definition of the right ascension of the ascending node.

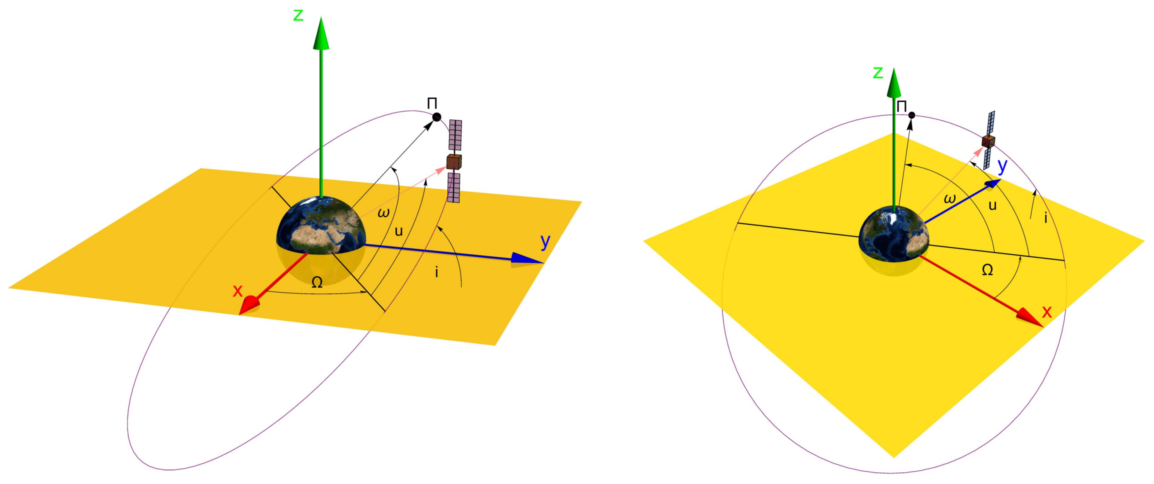

Figure 4: Two viewpoints on the orbital elements characterising the orientation of the ellipse and the position of the satellite in a Cartesian coordinate system: inclination $i$, right ascension of ascending node $\Omega$, argument of perigee $\omega$ and argument of latitude $u$. $\Pi$ marks the perigee. (The images were produced by the author with Wolfram Mathematica 14.0.0.0.)

The actual trajectory of a satellite differs from an ellipse because there are additional perturbations (see Sect. 2.2.3) acting on the satellite aside from the gravitational force of the Earth represented as a point mass. In this case, a term that includes all the perturbations needs to be added on the right hand side of Eq. (1) as will be discussed in Sect. 2.2. Nevertheless, the formulas of the two-body problem can be applied on a set consisting of a position $\vec{r}(t_i)$ and velocity $\vec{v}(t_i)$ at epoch $t_i$ to determine the Keplerian elements. In this case the orbital elements are called osculating elements (Beutler, 2005). The temporal evolutions of the osculating elements show oscillations of a multitude of periods and in some instances drifts.

Figure 5 shows the osculating semi-major axis $a$ of the satellite Swarm-A during 12 hours on 2024-05-01. The semi-major axis oscillates with an amplitude of about 10 km. The spacecraft sinks a couple 10 m during the time interval shown but the drift is not visible due to the large amplitude of the oscillation. The Earth's oblateness is the main driver for the twice-per-revolution periodic oscillations. The small drift is due to air drag.

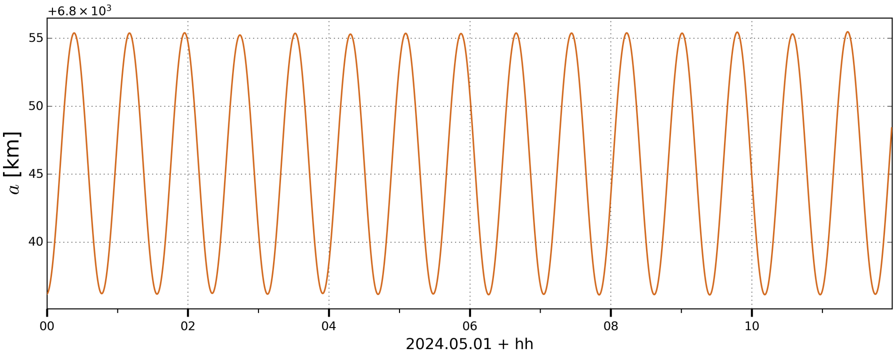

Figure 5: The osculating semi-major axis of the satellite Swarm-A during 12 hours on 2024-05-01.

To describe the motion of a satellite more accurately, more advanced representations for the description of satellite trajectories are presented in Sect. 2.2.

## 2.2 Orbit Representation

In this work the reduced-dynamic (RED-DYN) orbit representation is used. The RED-DYN orbit representation is a continuation of the dynamic (DYN) orbit. In comparison, the DYN orbit has more dynamical stiffness than the RED-DYN orbit because the latter is more data driven due to the estimation of additional empirical parameters from the GNSS data.

Details about the realisation of the RED-DYN orbit representation in the BSW will be given in Sect. 3.1.

### 2.2.1 Dynamic Orbit Representation

With a set of initial conditions

$$\vec{r}(t_0) = \vec{r}(a, e, i, \Omega, \omega, u_0; t_0) \qquad \dot{\vec{r}}(t_0) = \dot{\vec{r}}(a, e, i, \Omega, \omega, u_0; t_0) \tag{5}$$

The equation of motion reads:

$$\ddot{\vec{r}} = -\gamma \frac{\vec{r}}{|\vec{r}|^3} + \vec{f}(t, \vec{r}, \dot{\vec{r}}, Q_1, \ldots, Q_d), \tag{6}$$

where $\vec{f}$ represents the additional perturbations modelled in the dynamic orbit determination. $Q_1, \ldots, Q_d$ denote dynamical parameters appearing in force models. Such force models may be of analytical or numerical nature. An example for an analytical force model is the spherical harmonic representation of the Earth's gravity field. Accelerometer data measuring the sum of all non-gravitational accelerations acting on a satellite is an example of a numerical force model.

In the DYN orbit representation the satellite position reads:

$$\vec{r}(t) = \vec{r}(t; a, e, i, \Omega, \omega, u_0; Q_1, \dots, Q_d). \tag{7}$$

For each arc a set of initial conditions (5) is necessary to numerically integrate Eq. (6). The orbit is a smooth trajectory and orbit positions can be computed at any epoch within the arc. The typical arc length of LEO orbits estimated from GNSS data is one day.

#### 2.2.2 Reduced-Dynamic Orbit Representation

In the RED-DYN orbit representation, the equation of motion reads:

$$\ddot{\vec{r}} = -\gamma \frac{\vec{r}}{|\vec{r}|^3} + \vec{f}(t, \vec{r}, \dot{\vec{r}}, Q_1, \dots, Q_d, P_1, \dots, P_s), \tag{8}$$

where $P_1, \dots, P_s$ are additional pseudo-stochastic orbit parameters (Jäggi, 2007). The pseudo-stochastic orbit parameters are empirical parameters characterised by additional stochastic properties. They are able to compensate deficiencies in dynamic models.

In analogy to the DYN orbit, a set of initial conditions (5) is needed to numerically integrate Eq. (8) for one arc. Within this arc, the RED-DYN orbit representation of the satellite position reads:

$$\vec{r}(t) = \vec{r}(t; a, e, i, \Omega, \omega, u_0; Q_1, \dots, Q_d; P_1, \dots, P_s). \tag{9}$$

#### 2.2.3 Orbit Perturbations

The most important perturbations modelled in Eqs. (6) and (8) are:

- **Gravitational Field of Earth**: The Earth's gravitational potential can be represented by a spherical-harmonic expansion (Heiskanen and Moritz, 1967). It is worth to mention, that the coefficient $C_{2,0}$, which represents the oblateness of Earth, causes the largest perturbation for a LEO satellite orbit. The perturbation is responsible for the large oscillations visible in Fig. 5.
- **Atmospheric Drag**: Analytical as well as empirically driven models can be used to describe the temperature, density, composition as well as horizontal winds in the thermosphere and how air drag acts on a satellite. Models like DTM2013 (Bruinsma, 2015), NRLMSIS-00 (Picone et al., 2002) and JB2008 (Bowman et al., 2008) are often used in POD to model air drag.
- **Radiation Pressure**: Solar radiation pressure (SRP) and Earth radiation pressure (ERP) act on a satellite and decrease if the satellite passes through the Earth's shadow. Radiation acts as a force on a satellite through specular and diffuse reflection as well as absorption. The satellite itself exhibits thermal radiation and on-board antennas can produce thrust as well (however for the analysed LEO satellites this effect is negligible) (Dach, 2023).
- **Other Celestial Bodies**: Apart from Earth, the Sun and Moon are the most important celestial bodies to influence the orbit of a satellite. Their gravitational attraction influences the orbit of a satellite directly. By generating tidal effects on Earth, the gravitational field of the Earth is continuously changing which in turn impacts the orbit of the satellite as well.

The gravitational field of Earth and the gravitation of other celestial bodies act only on the center of mass of the satellite (approximate satellite as a point mass). Perturbations due to atmospheric drag and radiation pressure depend, however, on the material, form, size and mass of the satellite.

Explicit information about which models are implemented in the BSW to account for the various perturbations, can be found in Sect. 3.1.

### 2.3 Local Orbital Frame

In order to study the impact of perturbations on the orbital elements, a convenient coordinate system is needed to decompose the perturbation into three orthogonal directions.

In this work the local orbital frame (RSW) is used to describe forces acting on the satellite. The origin is defined at the center of mass of the satellite. The three axes of the coordinate system are the radial direction $R$, the along-track direction $S$ and the cross-track direction $W$. Because the analysed satellites have orbits with low eccentricity $e \ll 1$, the along-track direction is approximately parallel to the velocity $\vec{v}$. With $\vec{r}$ being the position vector and $\vec{v}$ being the velocity vector of the satellite, the unit vectors of the RSW coordinate system are defined as (Cai et al., 2020)

$$\vec{e_R} = \frac{\vec{r}}{|\vec{r}|}, \qquad \vec{e_W} = \frac{\vec{r} \times \vec{v}}{|\vec{r} \times \vec{r}|}, \qquad \vec{e_S} = \vec{e_W} \times \vec{e_R}. \tag{10}$$

Figure 6 illustrates the RSW coordinate system for a low eccentricity orbit with $e = 0.01$.

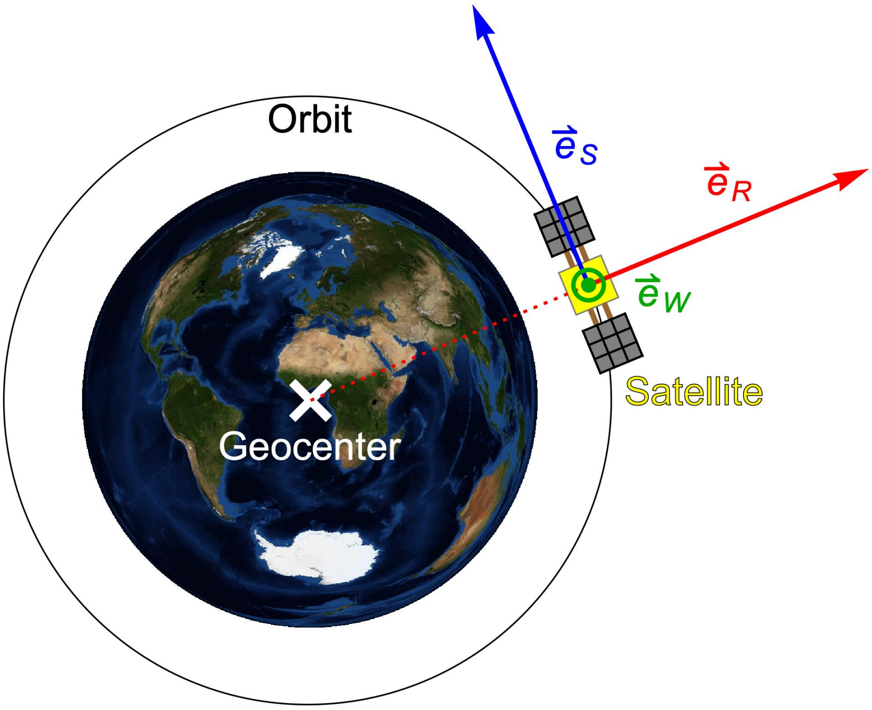

Figure 6: Illustration of the RSW coordinate system for an elliptical orbit of low numerical eccentricity $e = 0.01$. In this illustration $\vec{e}_W$ is pointing out of the plane of projection.

## 2.4 Gauss's Perturbation Equation

If the perturbative force or respectively the acceleration of the satellite is known, the time derivative of the osculating orbital elements can be calculated by means of the Gaussian perturbation equations. If the accelerations acting on the satellite are given in the RSW local orbital frame, the Gauss's perturbation equation for the semi-major axis $a_{\text{Gauss}}$ reads (Jäggi, 2022a):

$$\dot{a}_{\text{Gauss}} = 2\sqrt{\frac{a^3_{\text{Gauss}}}{\gamma(1-e^2)}}\left\{e\sin(u-\omega)R + \left[1 + e\cos(u-\omega)\right]S\right\}. \tag{11}$$

An accelerometer on-board the satellite will only measure non-gravitational forces. If data from the accelerometer is taken to numerically integrate Eq. (11) the obtained time series of the semi-major axis will, e.g., not contain the gravitational perturbation of $C_{2,0}$. Alternatively, estimated PCAs can be used as well as they also mainly absorb non-gravitational accelerations if they are not explicitly modelled in RED-DYN orbit determination using the BSW. However, if the gravitational field is modelled insufficiently, signals with periodicities related to the orbital period are induced in the PCAs. Equation (11) will be solved numerically with the Runge-Kutta Fourth Order (RK4) method as described in Sect. 2.5 and 4.3.

When numerically integrating Eq. (11) with the RK4 method, a first order approximation is applied by letting $e$ and $\omega$ be constant values. To perform the numerical integration, an initial value for $a_{\text{Gauss}}$ and time series for $u$, $R$ and $S$ are needed (more details about the initial values are given in Sect. 4.3). With each integration step a new value for $a_{\text{Gauss}}$ and $\dot{a}_{\text{Gauss}}$ is calculated simultaneously. With this, the Gaussian/integration approach is one of the two methods used in this work to obtain the orbital decay of a satellite if PCA estimates or accelerometer data are available.

## 2.5 Runge-Kutta Fourth Order Method

Equation (11) will be integrated numerically with the RK4 method. Thus in the following, this tool shall be illustrated.

If the differential equation $\dot{x} = \dot{x}(x(t), t)$ cannot be solved analytically, the RK4 method can be applied to obtain a numerical solution as a set of values at epochs $t_n$. The epochs are equidistantly spaced with a fixed step size $\lambda = t_{n+1} - t_n$. Starting with an initial value $x(t_0) = x_0$, the solution is propagated from $x(t_n) = x_n$ to $x(t_{n+1}) = x_{n+1}$ as (Pistillo, 2023)

$$x_{n+1} = x_n + \frac{k_1 + k_4}{6} + \frac{k_2 + k_3}{3} + \mathcal{O}\left(\lambda^5\right), \tag{12}$$

with the $k$-coefficients defined as (Pistillo, 2023):

$$k_1 = \lambda \cdot \dot{x}(x_n, t_n) \tag{13}$$

$$k_2 = \lambda \cdot \dot{x}(x_n + \frac{k_1}{2}, t_n + \frac{\lambda}{2}) \tag{14}$$

$$k_3 = \lambda \cdot \dot{x}(x_n + \frac{k_2}{2}, t_n + \frac{\lambda}{2}) \tag{15}$$

$$k_4 = \lambda \cdot \dot{x}(x_n + k_3, t_n + \lambda). \tag{16}$$

In the case of Eq. (11) $\dot{a}_{\text{Gauss}}$ is the corresponding variable $\dot{x}$. The eccentricity and the argument of perigee are taken as time independent variables (defined at $t_0$). The argument of latitude as well as the acceleration components are taken as time dependent. In this work the sampling of each time dependent variables is the same (if not they are resampled accordingly). This means that, the step size $\lambda$ has to be an integer multiple of twice of the sampling, otherwise the time dependent variables are not defined at each $t_n$. In this work, $\lambda$ is set to be exactly twice the sampling of the time dependent variables.

For the RK4 method the local truncation error is of the order $\mathcal{O}\left(\lambda^5\right)$ while the global truncation error is of the order $\mathcal{O}\left(\lambda^4\right)$. In this work $\lambda$ is either ten seconds or one minute (see Sect. 5) and both types of truncation errors are neglected. As $\dot{a}_{\text{Gauss}}$ is a function of $a_{\text{Gauss}}$, $e$, $\omega$, $u$, $R$ and $S$ an uncertainty in those variables propagates with the solution. Thus, Gauss' law of error propagation (Wurz, 2022) is applied.

$$\sigma^2_{a_{\text{Gauss},n+2}} = \sigma^2_{\text{Gauss},a_n} + \frac{\sigma^2_{k_1} + \sigma^2_{k_4}}{36} + \frac{\sigma^2_{k_2} + \sigma^2_{k_3}}{9}, \tag{17}$$

with

$$\sigma^2_{k_1} = \lambda^2 \sum_{\xi \in \{a_{\text{Gauss}}, e, \omega, u, R, S\}} \left(\frac{\partial \dot{a}_{\text{Gauss}}}{\partial \xi} \sigma_\xi\right)\Bigg|^2_{t=t_n} \tag{18}$$

$$\sigma^2_{k_2} = \lambda^2 \left\{ \left(\frac{\partial \dot{a}_{\text{Gauss}}}{\partial\left(a_{\text{Gauss},n} + \frac{k_1}{2}\right)}\right)^2 \left(\sigma^2_{a_{\text{Gauss},n}} + \frac{\sigma^2_{k_1}}{4}\right) + \sum_{\xi \in \{e, \omega, u, R, S\}} \left(\frac{\partial \dot{a}_{\text{Gauss}}}{\partial \xi} \sigma_\xi\right)\Bigg|^2_{t=t_n+\frac{\lambda}{2}} \right\} \tag{19}$$

$$\sigma^2_{k_3} = \lambda^2 \left\{ \left(\frac{\partial \dot{a}_{\text{Gauss}}}{\partial\left(a_{\text{Gauss},n} + \frac{k_2}{2}\right)}\right)^2 \left(\sigma^2_{a_{\text{Gauss},n}} + \frac{\sigma^2_{k_2}}{4}\right) + \sum_{\xi \in \{e, \omega, u, R, S\}} \left(\frac{\partial \dot{a}_{\text{Gauss}}}{\partial \xi} \sigma_\xi\right)\Bigg|^2_{t=t_n+\frac{\lambda}{2}} \right\} \tag{20}$$

$$\sigma^2_{k_4} = \lambda^2 \left\{ \left(\frac{\partial \dot{a}_{\text{Gauss}}}{\partial\left(a_{\text{Gauss},n} + k_3\right)}\right)^2 \left(\sigma^2_{a_{\text{Gauss},n}} + \sigma^2_{k_3}\right) + \sum_{\xi \in \{e, \omega, u, R, S\}} \left(\frac{\partial \dot{a}_{\text{Gauss}}}{\partial \xi} \sigma_\xi\right)\Bigg|^2_{t=t_n+\lambda} \right\}. \tag{21}$$

It should be noted, that the correlations between the variables $e$, $\omega$, $u$, $R$ and $S$ are neglected. As mentioned above the variables $e(t_n) = e(t_0) = e_0$ and $\omega(t_n) = \omega(t_0) = \omega_0$ are time independent and their uncertainties are time independent as well. However, the uncertainties of the time dependent variables, e.g. $\sigma_u$, are also time dependent. If the components $R$ and $S$ are measured by an on-board accelerometer, one has also to take into account that these are calibrated values (see Sect. 3.2) and the calibration also features uncertainties. Because of the complex nature of the propagation of uncertainty, some simplifications are performed in Sect. 4.3.

## 2.6 Fit Model for the Semi-Major Axis

In Vallado and McClain (2013) the perturbation acceleration caused by zonal (the order is $m = 0$) spherical harmonics of the Earth's gravitational potential is demonstrated. The total disturbing acceleration $F_{\text{total}}$ in the RSW local orbital frame is

$$\vec{F}_{\text{total}} = \sum_{l=2}^{\infty} \vec{F}_l, \qquad \vec{F}_l = \frac{\gamma}{r^2}\left(\frac{R_\oplus}{r}\right)^l C_{l,0} \begin{pmatrix} -(l+1)\mathcal{P}_l(\sin i \sin u) \\ \sin i \cos u \left.\frac{\mathrm{d}\mathcal{P}_l(\Xi)}{\mathrm{d}\Xi}\right|_{\Xi=\sin i \sin u} \\ \cos i \left.\frac{\mathrm{d}\mathcal{P}_l(\Xi)}{\mathrm{d}\Xi}\right|_{\Xi=\sin i \sin u} \end{pmatrix}, \tag{22}$$

where $R_\oplus$ is the mean equatorial radius of the Earth, $r = |\vec{r}|$, $C_{l,0}$ is the zonal spherical harmonic coefficient of degree $l$ and $\mathcal{P}_l$ is the Legendre polynomial of degree $l$:

$$\mathcal{P}_l(\Xi) = \frac{1}{2^l l!}\frac{\mathrm{d}^l}{\mathrm{d}\Xi^l}(\Xi^2 - 1)^l. \tag{23}$$

If the second part in Eq. (22) is evaluated for $l = 2$ the perturbing acceleration caused by $C_{2,0}$ in the local orbital frame is obtained:

$$\vec{F}_2 = \begin{pmatrix} R_2 \\ S_2 \\ W_2 \end{pmatrix} = \frac{3}{2}\frac{\gamma R_\oplus^2 C_{2,0}}{r^4} \begin{pmatrix} 1 - \frac{3}{2}\sin^2 i + \frac{3}{2}\sin^2 i \cos(2u) \\ \sin^2 i \sin(2u) \\ \sin(2i)\sin u \end{pmatrix}. \tag{24}$$

As mentioned before in Sect. 2.2.3 and shown in Fig. 5, the oblateness of the Earth causes the largest oscillation in the semi-major axis with the period being half of the orbital period. This periodicity is also visible in the perturbation accelerations given by Eq. (24) where the argument $2u$ appears in the radial component as the argument of a cosine function and in the along-track component as argument of a sine function (note that the cross-track component does not contribute to the change of the semi-major axis according to Eq. (11)). Equation (24) is evaluated as a function of $u$ in Fig. 7. If Eq. (22) is used to derive the perturbations of higher order zonal harmonics, periodicities with higher order fractions of the orbital period $P$ would be obtained, e.g. $p \propto \frac{P}{l}$. Figure 8 shows the spectrum of the osculating semi-major axis of Swarm-A from 2024-05-01 to 2024-05-05. The perturbation stemming from the oblateness of Earth is visible as the large peak with the period of approximately 48 min. There are many other periods with smaller amplitudes visible caused by all the different spherical harmonic coefficients of the Earth's gravity field.

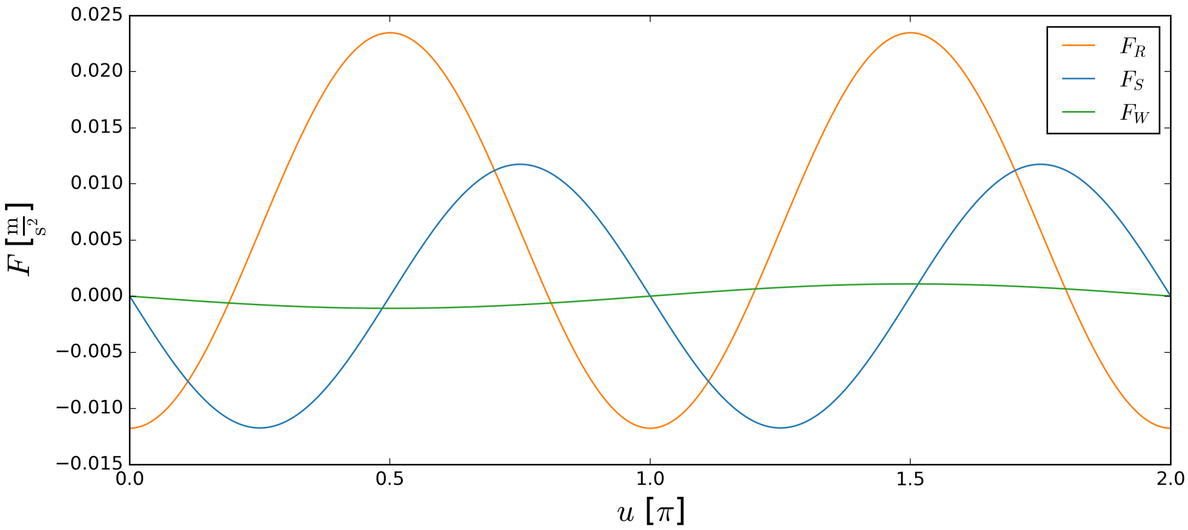

Figure 7: Perturbation acceleration caused by the $C_{2,0}$ term decomposed in the RSW components for an orbit with $i = 87.35°$ and $\gamma = 3.986 \cdot 10^{14}\,\frac{\mathrm{m}^3}{\mathrm{s}^2}$, $R_\oplus = 6{,}378\,\mathrm{km}$ and $r = 6{,}878\,\mathrm{km}$. The coefficient $C_{2,0} = -1.083 \cdot 10^{-3}$ is taken from literature (Jäggi, 2024). The radial acceleration $F_R$ is shown in orange, the along-track acceleration $F_S$ is shown in blue and the cross-track acceleration $F_W$ is shown in green.

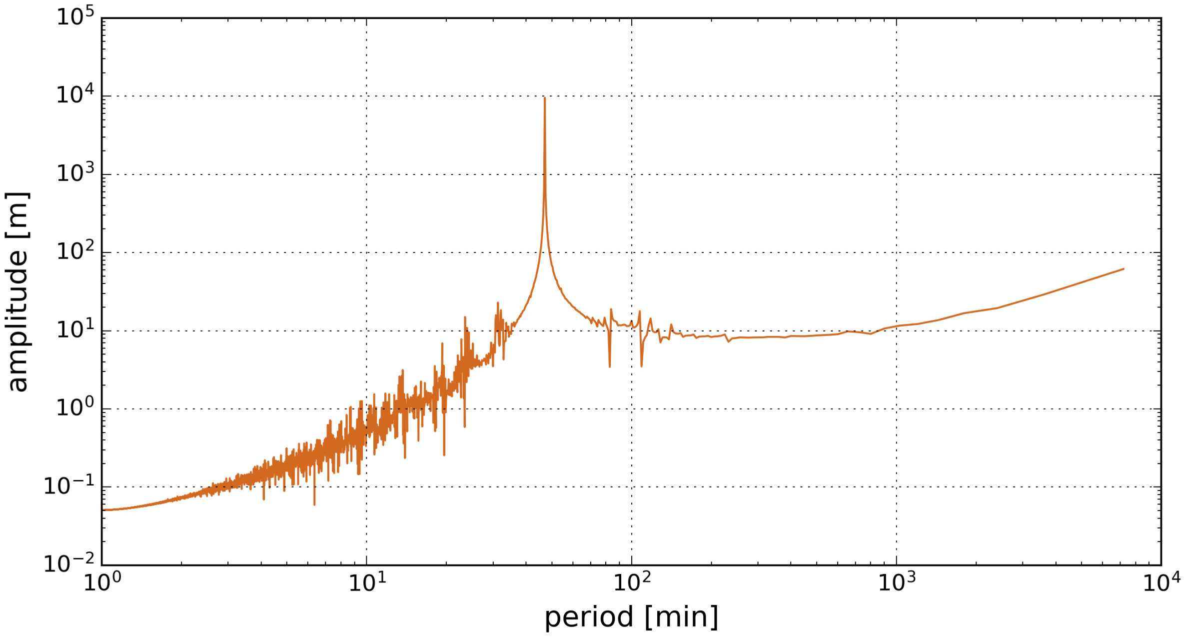

Figure 8: Amplitude spectrum of the semi-major axis of the satellite Swarm-A based on five days in the year 2024. The $C_{2,0}$ perturbation causes the large peak at approximately 48 min.

The fit model splits the signal into a slowly changing function $\bar{a}_{\text{Fit}}(t)$, which is representing the (time-varying) trend, and into a sum of $R$ different sinusoids each with a different period $p_r$, phase $\phi_r$ and amplitude $A_r$, $r = 1, \ldots, R$. If such a fit model is successfully fitted to the time series of the semi-major axis of a satellite, the orbital decay can be easily obtained by differentiating the trend function $\bar{a}_{\text{Fit}}(t)$ with respect to time. The fit model reads:

$$a_{\text{Fit}}(t) = \bar{a}_{\text{Fit}}(t) + \sum_{r=1}^{R} A_r \sin\left(\frac{2\pi}{p_r} t + \phi_r\right). \tag{25}$$

This can also be written as

$$a_{\text{Fit}}(t) = \bar{a}_{\text{Fit}}(t) + \sum_{r=1}^{R} \left(A_r \cos\phi_r \sin\frac{2\pi t}{p_r} + A_r \sin\phi_r \cos\frac{2\pi t}{p_r}\right). \tag{26}$$

In reality, the amplitudes $A_r$, the phases $\phi_r$ and the periods $p_r$ are time dependent: The periods depend on the orbital period which in turn depends on the semi-major axis as described in Kepler's third law of planetary motion (Beutler, 2005). The amplitudes are proportional to the amplitude of the perturbations, whereas most of them (for example the spherical harmonic coefficients of the gravity field of Earth), depend on the altitude of the satellite. It follows naturally that the phases are time dependent as well.

The amplitudes and phases are combined into the variables $\mu_r(t)$ and $\eta_r(t)$:

$$\mu_r(t) = A_r \cos\phi_r, \qquad \eta_r(t) = A_r \sin\phi_r, \qquad r = 1, \ldots, R. \tag{27}$$

This way the fit model reads:

$$a_{\text{Fit}}(t) = \bar{a}_{\text{Fit}}(t) + \sum_{r=1}^{R} \left(\mu_r(t) \sin\frac{2\pi t}{p_r} + \eta_r(t) \cos\frac{2\pi t}{p_r}\right). \tag{28}$$

To estimate the parameters $a_{\text{Fit}}$, $\mu_r$ and $\eta_r$ in a least squares adjustment (LSA), they are implemented in a piecewise linear representation (see Sect. 4.1.1.1). It is worth mentioning, that with $R = 1$ and $p_1$ corresponding to the period of the $C_{2,0}$ perturbation, the fit has already adequate quality.

# 3 Data

## 3.1 Bernese GNSS Software

The orbit estimations are performed with the BSW. The following types of orbits are processed:

- Nominal (NL) RED-DYN orbits with gravitational force modelling: all the non-gravitational forces are absorbed into the PCAs. These PCAs can be used for the numerical integration of Eq. (11) with the RK4 method. The osculating elements as well as the $\beta$ angle are calculated by BSW.
- RED-DYN orbits with gravitational and non-gravitational (NG) force modelling: contains PCAs as well but they are not used for the numerical integration of Eq. (11) with the RK4 method, because they only contain residual non-gravitational accelerations reflecting the deficiencies of the adopted non-gravitational force models. The osculating elements, the $\beta$ angle and the modelled air density $\varrho$ along the orbit are calculated by BSW.

The $\beta$ angle is a geometric variable that characterises the angle between the position of the Sun and the orbital plane. The $\beta$ angle thus provides information about the radiation pressure along the orbit. For example, SRP on a non-rotating surface is constant along the orbit for $\beta = 90°$. For $\beta = 0°$ SRP will (decrease) vanish when the spacecraft enters Earth's (partial) shadow. Additionally, for $\beta = 0°$ ERP will reach a maximum on the dayside and a minimum on the nightside. The $\beta$ angle remains approximately constant (it would be osculating but with no drift) for a sun-synchronous orbit.

BSW estimates one orbit arc per day. The estimated PCAs are estimated for intervals with a length of six minutes. Because daily orbits are estimated, the quality of the PCAs (and the orbit) is generally lower at the beginning and at the end of the daily orbit (day boundary problem). For specifics about time sampling and the choice of orbit type we refer to Sect. 5.

In the NL orbit, the NG forces are fully absorbed into the estimated PCAs. As NG force models are used for the NG orbit, the effect of those forces is not visible in the estimated PCAs (or just to a smaller extend in the case of insufficient force modelling quality). In Fig. 9 the difference in the osculating semi-major axis between the NL orbit and the NG orbit is shown for the time interval from 2023-02-15 to 2023-04-06 for the cases of GRACE-FO-1 and Swarm-A. In addition, CME arrival times are indicated by vertical yellow dotted lines. For this time interval the mean of the difference is 0.11 mm with a standard deviation of 31 mm for GRACE-FO-1 and for Swarm-A the mean of the difference is 16 mm with a standard deviation of 28 mm.

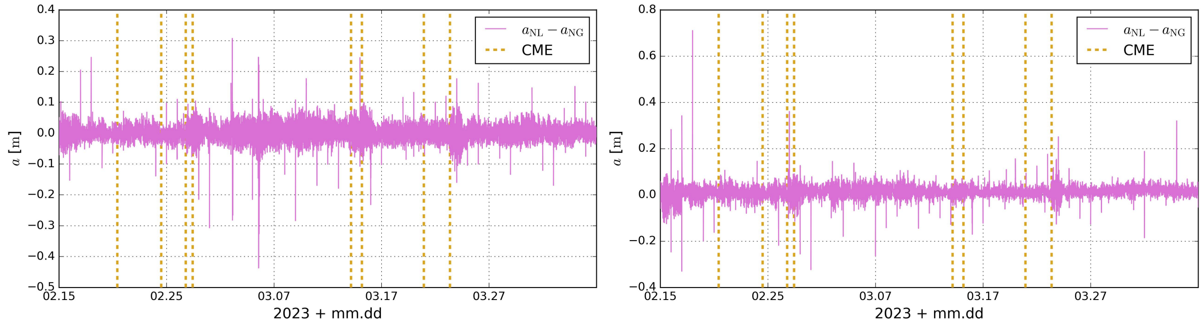

Figure 9: Differences in the osculating semi-major axis between the NL orbits and NG orbits for GRACE-FO-1 (left) and Swarm-A (right). CME arrival times are indicated by vertical yellow dotted lines.

The following list contains the models used for the orbit determination in the BSW. For more information see Mao et al. (2021).

- GOCO06s and GOCO05s (only used for GRACE-FO-1 in 2018) - for Earth's potential coefficients (with linear trends and periodic terms (only in GOCO06s) applied) up to degree and order 120;
- IERS2000 - for the solid Earth tides;
- EOT11A - for the ocean tides up to degree 50;
- DE421 and DE405 - for planetary ephemeris (Jupiter, Venus and Mars are considered);

- DESAI2016 - for subdaily Earth rotation parameters;
- IAU2000R06 - for nutation and precession;
- DTM2013 (NG) - as air density model;
- HWM14 (NG) - as horizontal wind model;
- SRP (NG) - with macro models;
- ERP (NG) - with both reflected and emitted radiation with macro models.

Figure 10 shows the air density evaluated with the DTM2013 model at an altitude of 500 km above a reference ellipsoid on the day before and on the day of the extreme geomagnetic storm in May of 2024. On the day before the geomagnetic storm the modelled air density ranges from $0.9 \cdot 10^{-12}\,\mathrm{kgm}^{-3}$ to $3.2 \cdot 10^{-12}\,\mathrm{kgm}^{-3}$. On the day of the extreme geomagnetic storm the modelled air density ranges from $2.9 \cdot 10^{-12}\,\mathrm{kgm}^{-3}$ to $9.4 \cdot 10^{-12}\,\mathrm{kgm}^{-3}$. The geomagnetic activity on 2024-05-10 is $Ap = 124$ and on 2024-05-11 it is $Ap = 284$.

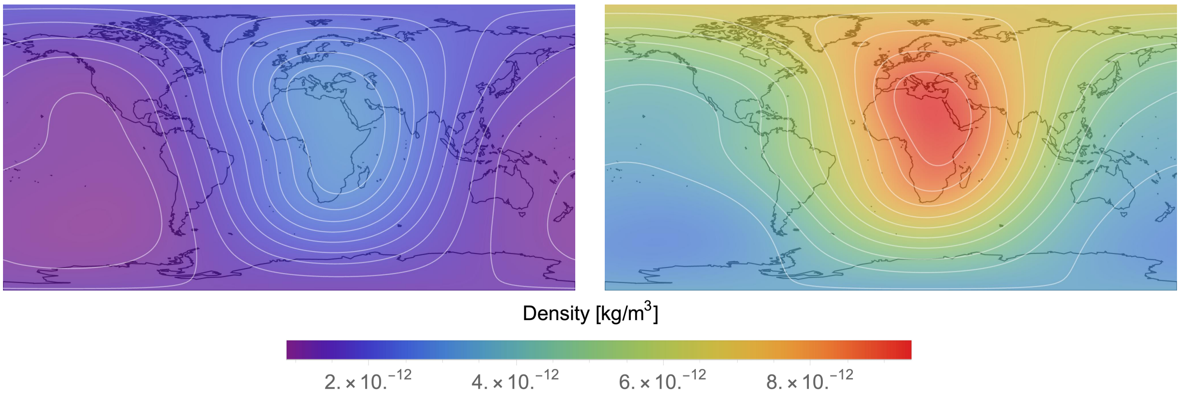

Figure 10: Neutral densities at 500 km altitude, estimated with DTM2013 for 2024-05-10 at 12:00 UTC (left) and for 2024-05-11 at 12:00 UTC (right). The grid resolution is 1° × 1° (latitude and longitude).

## 3.2 GRACE-FO-1 Accelerometer Data

For the year 2018 daily GRACE-FO-1 accelerometer (ACC) data transformed into the local orbital frame were provided by M. Lasser in the local orbital frame. Additionally, for each day, for each direction a scaling factor and a bias, determined in the operational gravity field determination at AIUB (Lasser et al., 2023), were provided as well. To obtain the calibrated accelerometer value $\Gamma_k$ in the direction $\Gamma \in \{\mathrm{R}, \mathrm{S}, \mathrm{W}\}$ at epoch $t_k$ during the day $\varkappa$, the mean value of that day $\overline{\Gamma_\varkappa}$ needs to be calculated and subtracted from the "raw" value $\widehat{\Gamma_k}$. The resulting value has to be multiplied by the corresponding scaling factor $s_{\Gamma,\varkappa}$ and the corresponding bias $b_{\Gamma,\varkappa}$ has to be added:

$$\Gamma_k = \left(\widehat{\Gamma_k} - \overline{\Gamma_\varkappa}\right) \cdot s_{\Gamma,\varkappa} + b_{\Gamma,\varkappa}. \tag{29}$$

The ACC data are provided with a one second sampling. For the analysis in the year 2018 they are down-sampled to five seconds.

The Gaussian perturbations equations are solved by deriving the perturbation accelerations either from the ACC data, or from the estimated PCAs, or from shifted ACC data to study the impact of the different data sources and biases on the estimation of the change of the semi-major axis. The latter is obtained by shifting each component of the ACC data with the difference between the mean value of each PCA component and the mean value of each ACC component. The mean component is calculated over the corresponding time interval of interest. This way, each mean PCA component is the same as the corresponding mean component of the shifted ACC data. Shifted ACC data is also used in the Gaussian approach to investigate the impact of the ACC data not having the same mean components as the PCAs as seen in the following.

In Fig. 11 both the calibrated ACC data as well as the estimated PCAs are shown for GRACE-FO-1 from 2018-08-25 to 2018-08-29. The PCAs are plotted as piecewise constant functions. Additionally, the arrival time of one CME on 2018-08-25 is indicated by the yellow dotted line. The magnitude of the accelerations is of order $10^{-8}\,\mathrm{ms}^{-2}$.

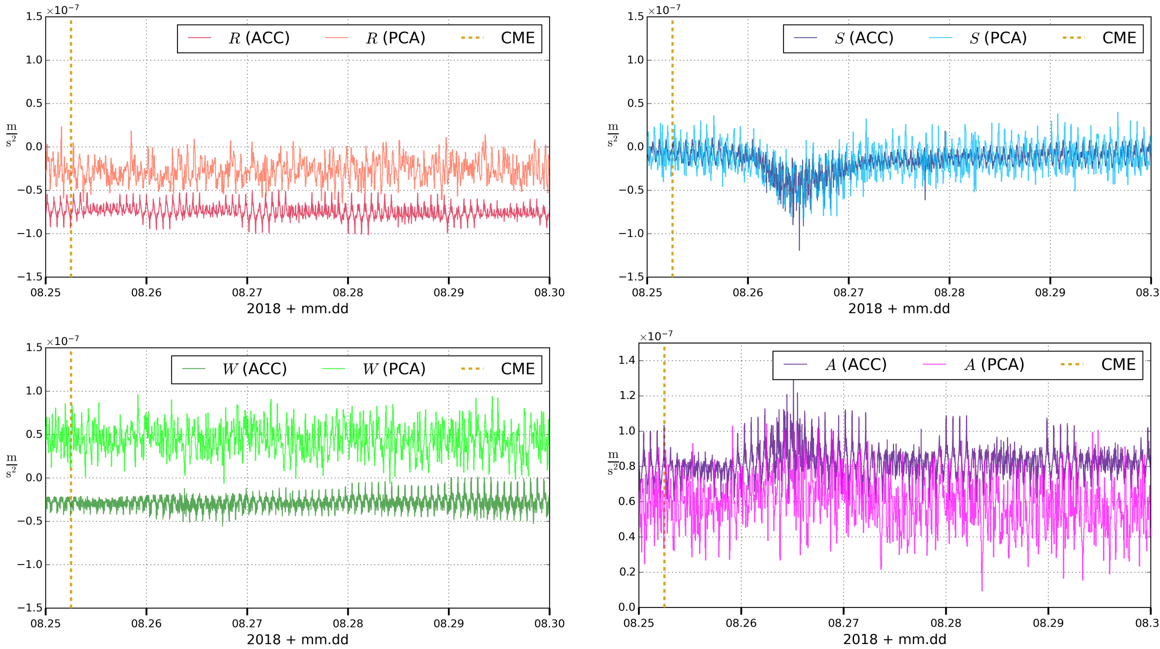

Figure 11: Calibrated ACC data accelerations and PCAs for GRACE-FO-1 in 2018. The accelerations are decomposed into: radial direction (top left); along-track direction (top right); cross-track direction (bottom left); absolute acceleration (bottom right).

The absolute acceleration from the ACC data for the interval 2018-08-25 to 2018-08-29 is shown in a semi-logarithmic plot in Fig. 12. The plot does not coincide with the top panel of Fig. 1 from Krauss et al. (2020). In their work the accelerations are centered around a mean value of about $3 \cdot 10^{-7}\,\frac{\mathrm{m}}{s^2}$ while in our work the mean value is about $8 \cdot 10^{-7}\,\frac{\mathrm{m}}{s^2}$. Moreover, their ACC data exhibits more noise. In our ACC data there are periodically time intervals with smaller oscillations (always starting in the middle of each day) which is not visible in their plot. These differences may need to be further investigated in the future. Nevertheless, with the data used in this work meaningful results are obtained as shown in Sect. 5.

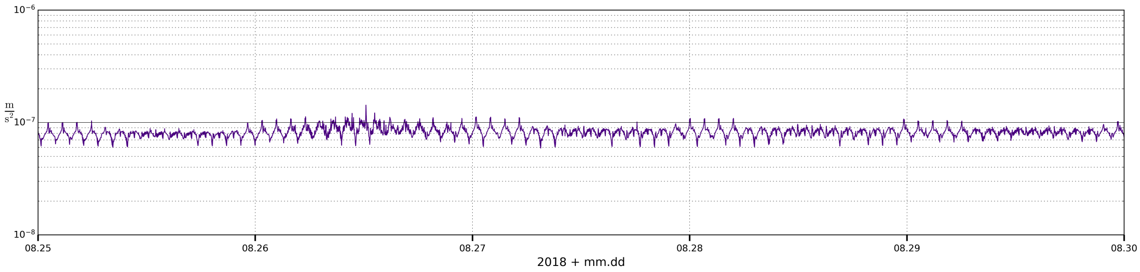

Figure 12: Absolute accelerations from the ACC data.

## 3.3 CME Arrival Times

The arrival times of CMEs are taken from the website CMEscoreboard (accessed on 2024-08-28). Additionally to the arrival times, the website also notes how the arrival time is identified. The identification of the CME arrival times is based on the signatures discussed in 1.1.1.

### 3.4 Additional Data

*Kp* indices from the National Oceanic and Atmospheric Administration (NOAA) of the Space Weather Prediction Center are converted to *ap* indices with a conversion table (see gfz-potsdam.de accessed on 2024-09-03).

*Dst* data is downloaded from the website lasp.colorado.edu (accessed on 2024-08-22).

*AE* data is downloaded from the website wdc.kugi.kyoto (accessed on 2024-08-22). Unfortunately, there is no *AE* index data available for the year 2023.

### 3.5 Data Processing

Computations are performed with Python (Versions 3.9 to 3.10.7). The written code is publicly available in a GitHub repository under https://github.com/coresnprogrammer/ISWEOLEOS.git.

## 4 Methods

The orbital decay is evaluated with two methods: solving numerically Gauss's perturbation equation for the semi-major axis and differentiating the piecewise linearised trend function estimated in a LSA. Originally, the first method used to evaluate the orbital decay was to smooth the time series of the osculating semi-major axis by adopting a Savitzky-Golay (SG) filter (Savitzky and Golay, 1964). Different polynomial degrees and filter lengths were experimented with, but the results were unsatisfactory. Therefore, a more sophisticated approach was developed, which started off with the fit model. Because aside from air drag, other forces (e.g. perturbation due to the $C_{2,0}$ term) impact the osculating semi-major axis, the separation of the orbital decay from the oscillations is not straightforward with the fit model. With the Gaussian approach, the evaluation of increased orbital decay, due to geomagnetic activity, is less difficult because the slope of the semi-major axis is directly derived from the non-gravitational forces which are directly measured by the accelerometer data or compensated by the estimated PCAs.

### 4.1 Least Squares Adjustment

In the following, the least squares adjustment for linearised problems is explained. The derivations and equations are based on the course Jäggi (2022b).

The difference between the observations $\vec{L}$ and the corresponding values $\vec{F}(\vec{x})$ calculated with a functional model $\vec{F}$ with parameters $\vec{x}$ is equal to the corrections $\vec{v}$:

$$\vec{v} = \vec{F}(\vec{x}) - \vec{L} \tag{30}$$

In the LSA of the fit model the time series of the semi-major axis obtained from the estimated orbits of BSW are used as pseudo-observations $\vec{L}$. In this work the functional model is linear and thus the first-design matrix $\boldsymbol{D}$ can be used:

$$\vec{F}(\vec{x}) = \boldsymbol{D} \cdot \vec{x} \qquad \boldsymbol{D} \doteq \frac{\partial \vec{F}(\vec{x})}{\partial \vec{x}}. \tag{31}$$

If the weighted square of the corrections shall be minimised, the following equations arise:

$$\boldsymbol{N} \cdot \vec{x} - \vec{b} = \vec{0} \qquad \boldsymbol{N} \doteq \boldsymbol{D}^{\mathrm{T}} \cdot \boldsymbol{P} \cdot \boldsymbol{D}, \qquad \vec{b} \doteq \boldsymbol{D}^{\mathrm{T}} \cdot \boldsymbol{P} \cdot \vec{L}, \tag{32}$$

where $\boldsymbol{P}$ is the weighting matrix (connected to the covariances of the observations), $\boldsymbol{N}$ is the normal equation matrix and $\vec{b}$ is the right-hand side of the normal equation system. The fitted parameters $\vec{x}$ are therefore obtained with

$$\vec{x} = \boldsymbol{N}^{-1} \cdot \vec{b}. \tag{33}$$

In this work the weighting matrix $\boldsymbol{P}$ is set to be the unit matrix and the a priori standard deviation of unit weight is set to $\sigma_0 = 1\,\mathrm{m}$. The uncertainty of the parameters depends on the total number of observations and the total number of estimated parameters. Its explicit formula will be given in Sect. 4.1.1.2 after implementing the piecewise linear representation.

### 4.1.1 Implementation of the Semi-Major Axis Fit Model

#### 4.1.1.1 Piecewise Linear Fit Model

The parameters $a_{\mathrm{Fit}}$, $\mu_r$ and $\eta_r$ of the fit model (28) for the semi-major axis are implemented in a piecewise linear representation: The time interval of interest is divided into $n_s$ subintervals. The duration of a subinterval is $\Delta\tau$. The boundary epochs of the vertices of the $n$-th subinterval are $\tau_{n-1}$ and $\tau_n$. Each of the variables $\bar{a}_{\mathrm{Fit}}(t)$, $\mu_r(t)$ and $\eta_r(t)$ is represented by a piecewise linear model between the epochs of the vertices. The vertices are estimated in a LSA. With $x$ being a vertex of one of the parameters mentioned before, the piecewise linear representation of $x$ is defined as

$$x(t) = \frac{(\tau_n - t)x_{n-1} + (t - \tau_{n-1})x_n}{\Delta\tau}, \qquad \tau_{n-1} < t < \tau_n, \qquad \forall x \in \{\bar{a}_{\mathrm{Fit}}, \mu_r, \eta_r\}. \tag{34}$$

This means, that there are $(2R+1)\cdot(n_s+1)$ parameters $x$ estimated in total.

According to Gauss's error propagation the error is

$$\sigma_x^2(t) = \frac{(\tau_n - t)^2\sigma_{x_{n-1}}^2 + (t - \tau_{n-1})^2\sigma_{x_n}^2}{\Delta\tau^2} \qquad \tau_{n-1} < t < \tau_n, \qquad \forall x \in \{\bar{a}_{\mathrm{Fit}}, \mu_r, \eta_r\}, \tag{35}$$

if the correlation between the parameters $x_n$ and $x_{n-1}$ is neglected.

The orbital decay can be extracted from $\bar{a}_{\mathrm{Fit}}(t)$ and is obtained by differentiating Eq. (34) with respect to time, if the corresponding parameter is the trend $\bar{a}_{\mathrm{Fit}}$, which yields a piecewise constant function over time:

$$\dot{\bar{a}}_{\mathrm{Fit}}(t) = \frac{\bar{a}_{\mathrm{Fit},n} - \bar{a}_{\mathrm{Fit},n-1}}{\Delta\tau}, \qquad \tau_{n-1} < t < \tau_n. \tag{36}$$

According to Gauss's error propagation the error is

$$\sigma_{\dot{\bar{a}}_{\mathrm{Fit}}}^2(t) = \frac{\sigma_{\bar{a}_{\mathrm{Fit},n}}^2 + \sigma_{\bar{a}_{\mathrm{Fit},n-1}}^2}{\Delta\tau^2} \qquad \tau_{n-1} < t < \tau_n, \tag{37}$$

if the correlation between the parameters $\bar{a}_{\mathrm{Fit},n}$ and $\bar{a}_{\mathrm{Fit},n-1}$ is neglected.

#### 4.1.1.2 LSA for the Piecewise Linear Fit Model and Constraining

In the following, the structure of the design matrix $\boldsymbol{D}$ shall be determined. There are $K$ observations at the epochs $t_k$, $k = 1,\dots,K$. The time span is divided into $n_s$ equally long subintervals with duration $\Delta\tau = \frac{t_K - t_1}{n_s}$. The subintervals are $[\tau_{n-1}, \tau_n]$, $n = 1,\dots,n_s$. The partial derivatives of the piecewise linear representation of Eq. (28) are:

$$\left.\frac{\partial a_{\mathrm{Fit}}}{\partial \bar{a}_{\mathrm{Fit},n-1}}\right|_{t=t_k} = \frac{\tau_n - t_k}{\Delta\tau}\delta_{k,n}, \qquad \left.\frac{\partial a_{\mathrm{Fit}}}{\partial \bar{a}_{\mathrm{Fit},n}}\right|_{t=t_k} = \frac{t_k - \tau_{n-1}}{\Delta\tau}\delta_{k,n}, \tag{38}$$

$$\left.\frac{\partial a_{\mathrm{Fit}}}{\partial \mu_{r,n-1}}\right|_{t=t_k} = \frac{\tau_n - t_k}{\Delta\tau}\delta_{k,n}\cdot\sin\frac{2\pi t_k}{p_r}, \qquad \left.\frac{\partial a_{\mathrm{Fit}}}{\partial \mu_{r,n}}\right|_{t=t_k} = \frac{t_k - \tau_{n-1}}{\Delta\tau}\delta_{k,n}\cdot\sin\frac{2\pi t_k}{p_r}, \tag{39}$$

$$\left.\frac{\partial a_{\mathrm{Fit}}}{\partial \eta_{r,n-1}}\right|_{t=t_k} = \frac{\tau_n - t_k}{\Delta\tau}\delta_{k,n}\cdot\cos\frac{2\pi t_k}{p_r}, \qquad \left.\frac{\partial a_{\mathrm{Fit}}}{\partial \eta_{r,n}}\right|_{t=t_k} = \frac{t_k - \tau_{n-1}}{\Delta\tau}\delta_{k,n}\cdot\cos\frac{2\pi t_k}{p_r}, \tag{40}$$

with $r = 1,\dots,R$ indicating the parameter corresponding to the $r$-th period $p_r$, and

$$\delta_{k,n} \doteq \begin{cases} 1, \tau_{n-1} \le t_k < \tau_n \\ 0, \text{else} \end{cases}. \tag{41}$$

With those partial derivatives the design matrix can be written with block matrices as

$$\boldsymbol{D} = (\boldsymbol{D}_{\bar{a}_{\mathrm{Fit}}}\ \boldsymbol{D}_{\mu_1}\ \dots\ \boldsymbol{D}_{\mu_r}\ \dots\ \boldsymbol{D}_{\mu_R}\ \boldsymbol{D}_{\eta_1}\ \dots\ \boldsymbol{D}_{\eta_r}\ \dots\ \boldsymbol{D}_{\eta_R}), \tag{42}$$

where

$$\boldsymbol{D}_x = \begin{pmatrix} \left.\frac{\partial a_{\mathrm{Fit}}}{\partial x_0}\right|_{t=t_1} & \cdots & \left.\frac{\partial a_{\mathrm{Fit}}}{\partial x_{n_s}}\right|_{t=t_1} \\ \vdots & & \vdots \\ \left.\frac{\partial a_{\mathrm{Fit}}}{\partial x_0}\right|_{t=t_K} & \cdots & \left.\frac{\partial a_{\mathrm{Fit}}}{\partial x_{n_s}}\right|_{t=t_K} \end{pmatrix}, \qquad x \in \{\bar{a}_{\mathrm{Fit}}, \mu_r, \eta_r\}, \qquad r = 1,\dots,R. \tag{43}$$

The design matrix $\boldsymbol{D}$ contains a total of $K$ rows and a total of $(n_s+1)(1+2R)$ columns. The number of columns also represents the number of parameters estimated in the LSA. The degree of freedom is therefore $K-(n_s+1)(1+2R)$ and thus the estimated a posteriori standard deviation of unit weight $m_0$ of the LSA is

$$m_0 = \sqrt{\frac{\vec{v}^{\mathrm{T}} \cdot \boldsymbol{P} \cdot \vec{v}}{K-(n_s+1)(1+2R)}}. \tag{44}$$

It turns out that the establishment of $\boldsymbol{D}$ is computationally expensive. For example, if such a LSA with 2 periods and 10 subintervals per day is executed for observations with a time span of 20 days and a time step of 30 seconds, the design matrix contains 57,888,000 entries. To calculate $\boldsymbol{N}$ by multiplying matrices as in (32) is therefore computationally expensive. It is thus favourable, to compute, e.g. the contribution of an individual observation to the normal equation system and to immediately update the normal equation system without storing the full design matrix.

In this work the covariances between the parameters are neglected when performing the propagation of uncertainty. The squared errors of the parameters are calculated as

$$\sigma_{x_n}^2 = \left(m_0^2 \cdot \boldsymbol{N}^{-1}\right)_{\vartheta\vartheta}, \qquad \vartheta = \begin{cases} n, & x = \bar{a}_{\mathrm{Fit}} \\ (n_s+1)\cdot(1+r)+n, & x = \mu_r \\ (n_s+1)\cdot(1+R+r)+n, & x = \eta_r \end{cases}, \qquad n = 0, \dots, n_s. \tag{45}$$

The following derivations and equations are based on the course Jäggi and Arnold (2024). If $n_s$ is chosen too large relative to $K$, the information content of the observations will not be sufficient to freely estimate all parameters and the scattering of the parameters will increase. However, for this work a rather high time resolution of $\bar{a}_{\mathrm{Fit}}$ is desired, e.g., ten subintervals per day. Thus, a Tikhonov regularisation is applied by constraining the secondary differences (second derivative) because they are not expected to be large:

$$(x_{n+1}-x_n)-(x_n-x_{n-1}) \approx 0, \qquad n = 1, \dots, n_s \qquad x \in \{\bar{a}_{\mathrm{Fit}}, \mu_r, \eta_r\}, \qquad r = 1, \dots, R. \tag{46}$$

This way, the scattering of the parameters is suppressed but the first derivative, which is of primary interest for this work, is not directly affected by the constraint. These equations (46) can be viewed as additional pseudo-observations. They can be written in matrix/vector notation as

$$\boldsymbol{C} \cdot \vec{x} = \vec{0}, \tag{47}$$

with

$$\boldsymbol{C} = \mathrm{diag}\left(\boldsymbol{C}_{\bar{a}_{\mathrm{Fit}}}, \boldsymbol{C}_{\mu_1}, \dots, \boldsymbol{C}_{\mu_r}, \dots, \boldsymbol{C}_{\mu_R}, \boldsymbol{C}_{\eta_1}, \dots, \boldsymbol{C}_{\eta_r}, \dots, \boldsymbol{C}_{\eta_R}\right) \tag{48}$$

and

$$\boldsymbol{C}_x = \begin{pmatrix} 1 & -2 & 1 & 0 & \dots & 0 \\ 0 & 1 & -2 & 1 & 0 & \dots \\ \dots & \dots & \dots & \dots & \dots & \dots \\ 0 & \dots & 0 & 1 & -2 & 1 \end{pmatrix}, \qquad \forall x \in \{\bar{a}_{\mathrm{Fit}}, \mu_r, \eta_r\}, \qquad r = 1, \dots, R. \tag{49}$$

The matrix $\boldsymbol{C}_x$ has $n_s-1$ rows and $n_s+1$ columns. These additional pseudo-observations are weighted with a weighting factor $\psi$ and are superimposed with the normal equation matrix $\boldsymbol{N}$ as

$$\boldsymbol{N} \rightarrow \boldsymbol{N} + \psi \cdot \boldsymbol{N}_{\mathrm{constr}}, \qquad \boldsymbol{N}_{\mathrm{constr}} = \boldsymbol{C}^{\mathrm{T}} \cdot \boldsymbol{C}. \tag{50}$$

With the weighting factor $\psi$ the strength of the constraining can be controlled. The weighting factor is chosen in a way that $\bar{a}_{\mathrm{Fit}}$ does not contain periodic oscillations with large amplitudes but in theory, the *L-curve criterion* (Hansen, 2001) could be used to find an optimal value for the constraining factor. The weighting factor is directly linked to the ratio $\frac{n_s}{K}$ as a LSA with more subintervals requires stronger weighting to produce similar results if $K$ stays the same. With $\psi \rightarrow \infty$ the slope of $x \in \{\bar{a}_{\mathrm{Fit}}, \mu_r, \eta_r\}$ will remain at a constant value throughout the entire time span. With stronger constraining, the magnitude of a temporary change in the slope decreases and the duration is stretched out. The constraining factor also affects the a posteriori standard deviation of unit weight and the errors of the parameters.

## 4.2 Performance of the Piecewise Linear Fit Model in a Simulation

The fit model is tested in a simulation environment, where successively more effects are taken into account that are observed in real data. The objective is to evaluate the ability of the fit model to accurately estimate the trend values $\bar{a}_{\text{Fit}}$ as well as the derived orbital decay according to Eq. (36). Another objective is to evaluate the influence of the weighting factor $\psi$ on the quality of the solution. If the fit model is able to perform well in spite of the disturbing effects mentioned below, the application of the fit model onto satellite data is justified.

The simulation spans a time interval of 20 days consisting of 57,600 equally spaced data points. This corresponds to a cadence of 30 seconds as it is the case for most osculating element data analysed in this work. The amount of subintervals fitted per day is set to $n_{\text{fac}} = 10$, as it will be the case for the fit model applied to the LEO satellites. The weighting factor $\psi$ is successively adjusted throughout the simulation in a way, that appropriate results are obtained. In each simulation LSAs with $R = 1$ and $R = 3$ are performed. This way, the impact of not modelled prominent periodic perturbations on the quality of the results is investigated.

The variables $a_{\text{Sim}}$, $\bar{a}_{\text{Sim}}$ and $\dot{\bar{a}}_{\text{Sim}}$ denote the simulated semi-major axis, its trend function and the slope of the trend function. Similarly, $a_{\text{Fit}}$, $\bar{a}_{\text{Fit}}$ and $\dot{\bar{a}}_{\text{Fit}}$ denote the fitted semi-major axis, its trend function and the slope of the trend function. Additionally, the variable $\sigma_{\text{Fit}}$ denotes the error of the corresponding fit variable (in a plot with $\bar{a}_{\text{Fit}}$ it is the error of the trend function given in Eq. (35) and in a plot with $\dot{\bar{a}}_{\text{Fit}}$ it is the error of the slope given in Eq. (37)). In the figures the variable denotes the range of error (e.g. the area between $a_{\text{Fit}} - \sigma_{\text{Fit}}$ and $a_{\text{Fit}} + \sigma_{\text{Fit}}$).

The successively added effects in the simulation are:

1. Offset, prominent periods and linear drift: This is done to test the fit model in a "standard" environment.
2. Gaussian perturbation: With this effect the influence of a geomagnetic storm is simulated.
3. Time dependency of prominent periods: This effect simulates the influence of orbital decay on modelled periods that are related to the full orbital period.
4. Short periods: With this simulation the impact of not modelled short periods on the quality of the results is evaluated.
5. Long periods: With this simulation the impact of not modelled long periods on the quality of the results is evaluated.

They are explained in more detail in the corresponding sections.

As the fit model gets applied to the simulated data, the following figures are generated:

(a) Spectra of the simulated data, the fitted data, and the trends of both the simulated and the fitted data (the spectra are multiplied by different factors for better visibility) - to check if the estimated trend shows any periodic features (which would be suboptimal);

(b) Plot of the trend of the simulated data and the trend of the fitted data - to control the overall quality of the trend;

(c) Plot of the decay/slope of the simulated and the fitted semi-major axis trend - to evaluate the ability of the model to reproduce the simulation truth.

### 4.2.1 Offset, Prominent Periods and Linear Drift

To produce the data of the simulation an offset of $a_0 = 6,837,491\,\text{m}$ is chosen. This corresponds to the semi-major axis at the beginning of the simulation. Additionally, three prominent periods related to the orbital period are simulated. To obtain the orbital period $P$, Kepler's third law of planetary motion is used (Jäggi, 2022a):

$$P^2 = \frac{4\pi^2}{\gamma} a^3. \tag{51}$$

With this formula and setting $a = a_0$ the orbital period $P$ is obtained (for the numerical value of $\gamma$ see Sect. 4.3). The strongest of the three prominent periods $p_1$ is half of the orbital period ($C_{2,0}$ is the main driver of this period). The second strongest period $p_2$ is the second overtone (or just one third) of the orbital period ($C_{3,0}$ is a driver of this period). The third prominent period $p_3$ should be larger than $p_1$ and is intentionally chosen in such a way, that the ratio $P/p_3$ cannot be expressed as a small-integer ratio. The periods and their corresponding amplitudes $A_r$ and phases $\phi_r$ are given in Tab. 2. Moreover, a linear drift of $d = -61.324\,\mathrm{md}^{-1}$ is added to simulate the impact of air drag.

Table 2: Prominent periods with their corresponding amplitude and phase.

| $r$ | $p_r$ [min] | $A_r$ [m] | $\phi_r$ [rad] |
|---|---|---|---|
| 1 | 46.89 | 7,342.00 | 0.30 |
| 2 | 31.26 | 43.32 | 0.73 |
| 3 | 107.84 | 12.21 | 1.20 |

It should be noted that the simulation environment is partly inspired by the results of Swarm-A in 2023 (see Sect. 5.2.2). The starting value of the semi-major axis is a random number lying inside the corresponding interval given in Tab. 1. The amplitudes are inspired by Fig. 33 and the value for the drift is inspired by the mean value of the slope obtained via the Gaussian approach.

The simulated data is generated according to Eq. (25) with $\bar{a}_{\mathrm{Sim}}(t) = a_0 + d \cdot t$ and thus the slope is simply $\dot{\bar{a}}_{\mathrm{Sim}}(t) = d$. The values for the periods in Tab. 2 are directly used in every LSA (including those performed in the next four sections) as values for the periods in the fit model.

The LSA with $R = 1$ is performed with $\psi = 10^3$ and the estimated a posteriori standard deviation of unit weight is $m_0 = 32.00\,\mathrm{m}$. The results for this LSA are shown in Fig. 13 (first column). The LSA with $R = 3$ is performed with $\psi = 0$ and the estimated a posteriori standard deviation of unit weight is $m_0 = 15.82\,\mathrm{nm}$. The results for this LSA are also shown in Fig. 13 (second column). For the LSA with $R = 1$ the error $m_0$ is much larger than for the LSA with $R = 3$ because of the prominent periods that are not included in the fit model. The low error of the LSA with $R = 3$ shows that the fit model can accurately reproduce the data if the prominent periods are known and there are no other periodic perturbations present. If there are prominent periods that are not modelled, they influence the trend function if $n_{\mathrm{fac}}$ is large enough (a period of, e.g., ten seconds will not induce oscillations if $n_{\mathrm{fac}}$ is of the magnitude of hours).

The top row of Fig. 13 shows the spectra of simulated and fitted data as well as of the trend functions of the simulated and the fitted data, the middle row displays the trend functions and in the bottom row the slopes of the trend functions are shown.
As mentioned before, the LSA with $R = 1$ constraining is necessary to dampen the oscillations absorbed in $\bar{a}_{\mathrm{Fit}}$. The spectrum (top left) shows that a constraining factor of $\psi = 10^3$ is sufficient to dampen the absorption of the not modelled periods in the spectrum of $a_{\mathrm{Fit}}$ into the spectrum of $\bar{a}_{\mathrm{Fit}}$. With both configurations regarding $R$ and $\psi$ the spectra of the trend functions are smooth. When the LSA with $R = 1$ is done without constraining, little spikes are visible in the spectrum of both $a_{\mathrm{Fit}}$ and $\bar{a}_{\mathrm{Fit}}$ (not shown).
In both configurations ($R$ and $\psi$) the resulting trend of the fit $\bar{a}_{\mathrm{Fit}}$ matches the trend function of the simulated data. In the case of $R = 1$ and $\psi = 10^3$, the error of $\bar{a}_{\mathrm{Fit}}$ has to be scaled by a factor of $10^2$ for visibility. In the case of $R = 3$ and $\psi = 0$, a similar level of visibility of the error of $\bar{a}_{\mathrm{Fit}}$ is achieved with a scaling factor of $10^{11}$.
In the case of $R = 3$ and $\psi = 0$, the difference between $\dot{\bar{a}}_{\mathrm{Sim}}$ and $\dot{\bar{a}}_{\mathrm{Fit}}$ lies in the $\mu$m range. The difference is not 0 m because a LSA adjustment cannot be perfect in general (limited number of digits in numerical computation). The estimated error of $\dot{\bar{a}}_{\mathrm{Fit}}$ is in the nm range. In the case of $R = 1$ and $\psi = 10^3$, $\dot{\bar{a}}_{\mathrm{Fit}}$ differs from $\dot{\bar{a}}_{\mathrm{Fit}}$ significantly (up to $10\,\mathrm{md}^{-1}$) at the start and at the end of the time interval. It seems that the fit model needs approximately 12 h to "calibrate" because the first and the last vertices are less accurately determined by the LSA. Apart from that, the difference between $\dot{\bar{a}}_{\mathrm{Fit}}$ and $\dot{\bar{a}}_{\mathrm{Sim}}$ is below $1\,\mathrm{md}^{-1}$. Considering the error of $\dot{\bar{a}}_{\mathrm{Fit}}$, values for the slope range from $-47.5\,\mathrm{md}^{-1}$ to $-76\,\mathrm{md}^{-1}$. If the LSA for $R = 1$ is performed with $\psi = 0$, $\dot{\bar{a}}_{\mathrm{Fit}}$ would show oscillating behaviour, reaching values above $-40\,\mathrm{md}^{-1}$ and below $-80\,\mathrm{md}^{-1}$ (not shown). If the LSA for $R = 1$ is performed with $\psi = 10^2$, $\dot{\bar{a}}_{\mathrm{Fit}}$ would show oscillating behaviour as well, reaching values between $-58.0\,\mathrm{md}^{-1}$ and $-64.5\,\mathrm{md}^{-1}$ (not shown). On the other hand, if the LSA for $R = 3$ is performed with $\psi = 10^3$ the difference between $\dot{\bar{a}}_{\mathrm{Sim}}$ and $\dot{\bar{a}}_{\mathrm{Fit}}$ is usually less than $1\,\mu$m but the estimated error of $\dot{\bar{a}}_{\mathrm{Fit}}$ is larger (not shown).

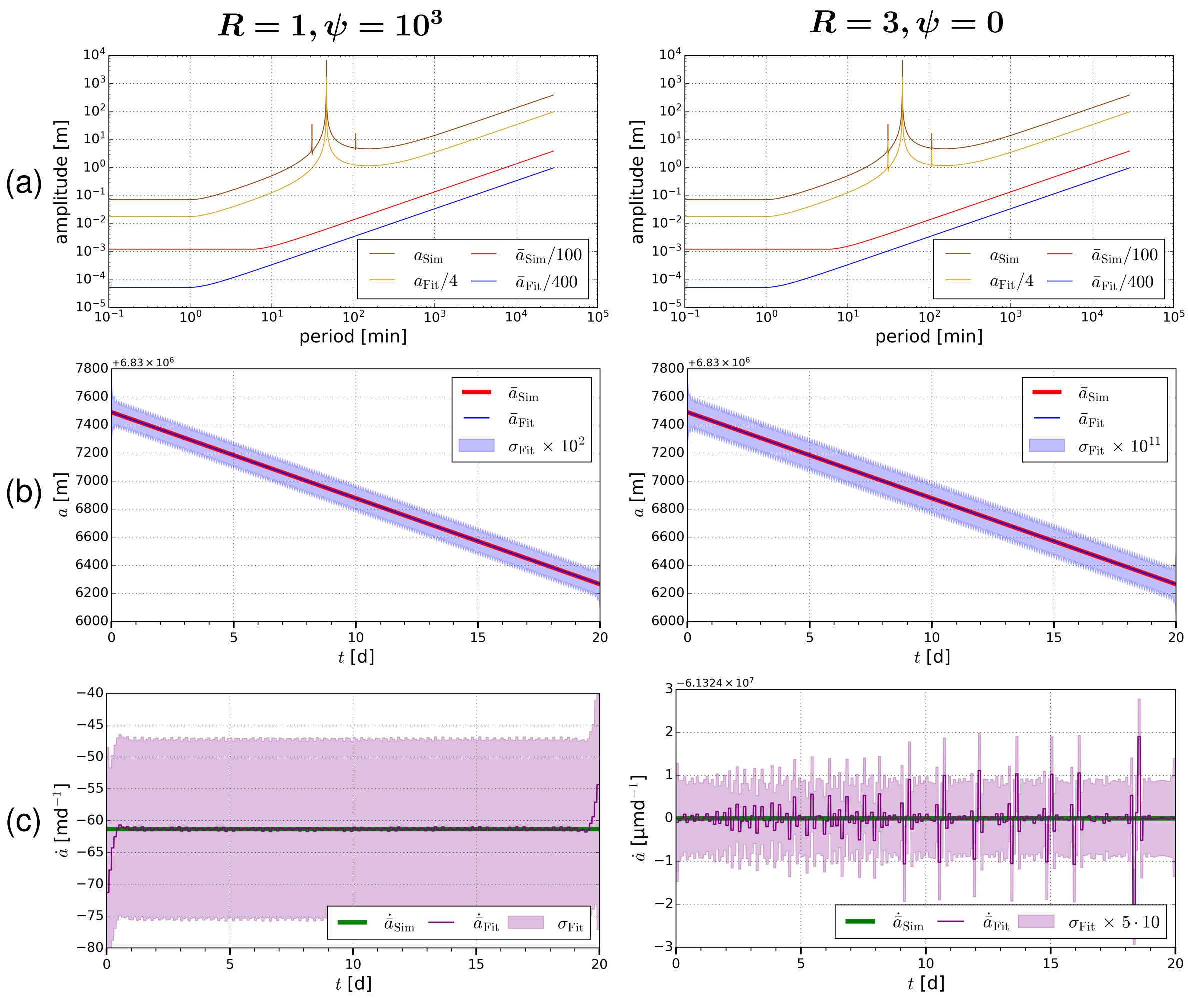

Figure 13: Results from the LSAs performed with $R = 1$ modelled period and constraining factor $\psi = 10^3$ (first column) and with $R = 3$ modelled periods and constraining factor $\psi = 0$ (second column). In (a) the spectra of $a_{\text{Sim}}$ and $a_{\text{Fit}}$, as well as $\bar{a}_{\text{Sim}}$ and $\bar{a}_{\text{Fit}}$ are shown. In (b) the trend function of the simulated data and the trend function of the fitted data along with its error is plotted. In (c) the slopes of the trend functions are shown.

The simulation shows that strong perturbations with periodic nature decrease the quality of the LSA if they are not modelled. In this simulation a constraining factor of $\psi = 10^3$ is necessary to maintain the quality of the LSA if the prominent periods are not modelled. The simulation also shows that the fit model can reproduce a linear drift of $d = -61.324\,\text{md}^{-1}$. Moreover, the accuracy of the fit model decreases at the beginning and at end of the time interval.

### 4.2.2 Gaussian Perturbation

To simulate the influence of a geomagnetic storm a Gaussian perturbation of the form

$$g(t) = -\frac{\mathrm{h}\cdot\mathrm{w}}{4}\left[1+\mathcal{E}\left(\frac{2\sqrt{\pi}}{\mathrm{w}}\cdot(t-\bar{t})\right)\right], \qquad \mathcal{E}(z) = \frac{2}{\sqrt{\pi}}\int_0^z e^{-y^2}dy \tag{52}$$

is added to the previous effects, where $\bar{t}$ is the point in time when the perturbation is the strongest, h is the height factor, w is the width factor and $\mathcal{E}$ denotes the Gauss error function. The derivative is a scaled Gaussian distribution:

$$\dot{g}(t) = -\mathrm{h}\cdot e^{-4\pi\cdot\frac{(t-\bar{t})^2}{\mathrm{w}^2}}. \tag{53}$$

The consequence of such a perturbation is that the semi-major axis decreases by an additional value of $\frac{\mathrm{h}\cdot\mathrm{w}}{2}$ and the magnitude of the slope at $\bar{t}$ is now larger by a value of h. The “significant” duration of the Gaussian perturbation corresponds to the width factor w. This means that for $t < \bar{t} - \frac{\mathrm{w}}{2}$ the functions are $g(t) \approx 0\,\mathrm{m}$ and $\dot{g}(t) \approx 0\,\mathrm{md}^{-1}$ and for $t > \bar{t} + \frac{\mathrm{w}}{2}$ the functions are $g(t) \approx \frac{\mathrm{hw}}{2}$ and $\dot{g}(t) \approx 0\,\mathrm{md}^{-1}$. The target value for the slope due to drift and Gaussian perturbation is $d - \mathrm{h}$ at $t = \bar{t}$.

In Fig. 14 the functions $g(t)$ and $\dot{g}(t)$ are plotted. For the simulation the central epoch is chosen to be $\bar{t} = 6.5\,\mathrm{d}$, while the height factor is set to $\mathrm{h} = 42\,\mathrm{md}^{-1}$ and the width factor is set to $\mathrm{w} = 1.5\,\mathrm{d}$. A target value of $-103.32\,\mathrm{md}^{-1}$ for the slope should be reached at $\bar{t}$ if the fit is able to perfectly follow the Gaussian perturbation. The values of $h$ and w are also inspired by the analysis of Swarm-A in the year 2023 (see Sect. 5.2.2).

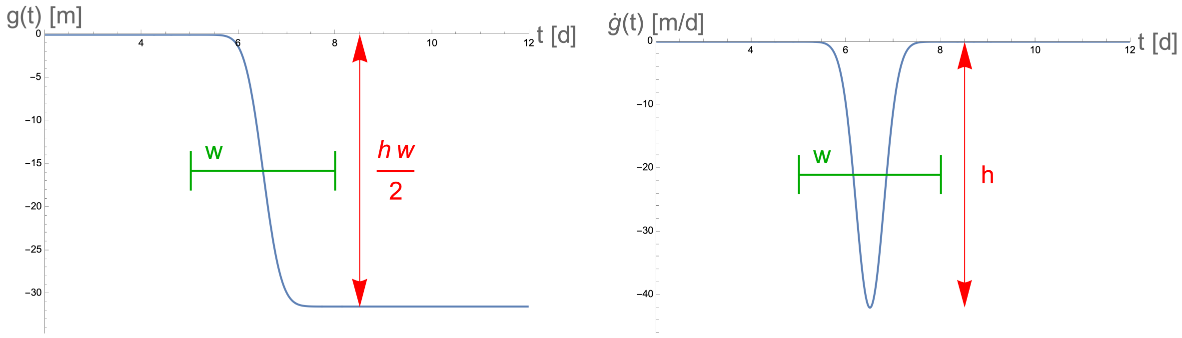

Figure 14: The functions $g(t)$ (left) and $\dot{g}(t)$ (right) with the numerical values used in this simulation.

The LSA with $R = 1$ is performed with $\psi = 10^3$ and the estimated a posteriori standard deviation of unit weight is $m_0 = 32.00\,\mathrm{m}$. The results for this LSA are shown in Fig. 15 (first column). The LSA with $R = 3$ is performed with $\psi = 0$ and the estimated a posteriori standard deviation of unit weight is $m_0 = 1.09\,\mathrm{mm}$. The results for this LSA are also shown in Fig. 15 (second column).

The top row of Fig. 15 shows the spectra of simulated and fitted data as well as of the trend functions of the simulated and the fitted data, the middle row displays the trend functions and in the bottom row the slopes of the trend functions are shown.

Due to the perturbation the spectra do not appear as perfectly straight lines above 1,000 min. Apart from that the spectra are not too different from the previous simulation.

In the case of $R = 3$ and $\psi = 0$ the error of $\bar{a}_{\mathrm{Fit}}$ is now scaled by a factor of $10^6$ for visibility. The trend functions now exhibit a kink around $t = 6.5\,\mathrm{d}$ due to the perturbation. In both cases, the fit model is able to accurately model the kink and still match the trend function of the simulated data.

As in the previous simulation, $\dot{\bar{a}}_{\mathrm{Fit}}$ differs from $\dot{\bar{a}}_{\mathrm{Fit}}$ significantly at the start and at the end of the time interval in the case of $R = 1$ and $\psi = 10^3$. Taking the errors into considerations, the values for the slope range from about $-47.5\,\mathrm{md}^{-1}$ to about $-75\,\mathrm{md}^{-1}$ during quiet times, which are epochs with low geomagnetic activity (start and end of time interval are not included). During the simulated geomagnetic storm $\dot{\bar{a}}_{\mathrm{Fit}}$ reaches $-100\,\mathrm{md}^{-1}$, barely missing the ideal $-103.32\,\mathrm{md}^{-1}$. Taking the error into consideration, the peak value lies between $-85\,\mathrm{md}^{-1}$ and $-115\,\mathrm{md}^{-1}$. In the case of $R = 3$ and $\psi = 0$, $\dot{\bar{a}}_{\mathrm{Fit}}$ accurately matches $\dot{\bar{a}}_{\mathrm{Sim}}$ and reaches a peak value of $-103\,\mathrm{md}^{-1}$ due to the perturbation. The error of $\dot{\bar{a}}_{\mathrm{Fit}}$ is in the mm range.

The results show that the fit model with the given configurations can reproduce increased orbital decay due to a geomagnetic storm if it has the form given in Eq. (52) and if the ratio between interval length ($n_{\mathrm{fac}}^{-1}$) and duration of storm is adequate. However, the peak orbital decay during a magnetic storm is underestimated if constraining is used in the LSA.

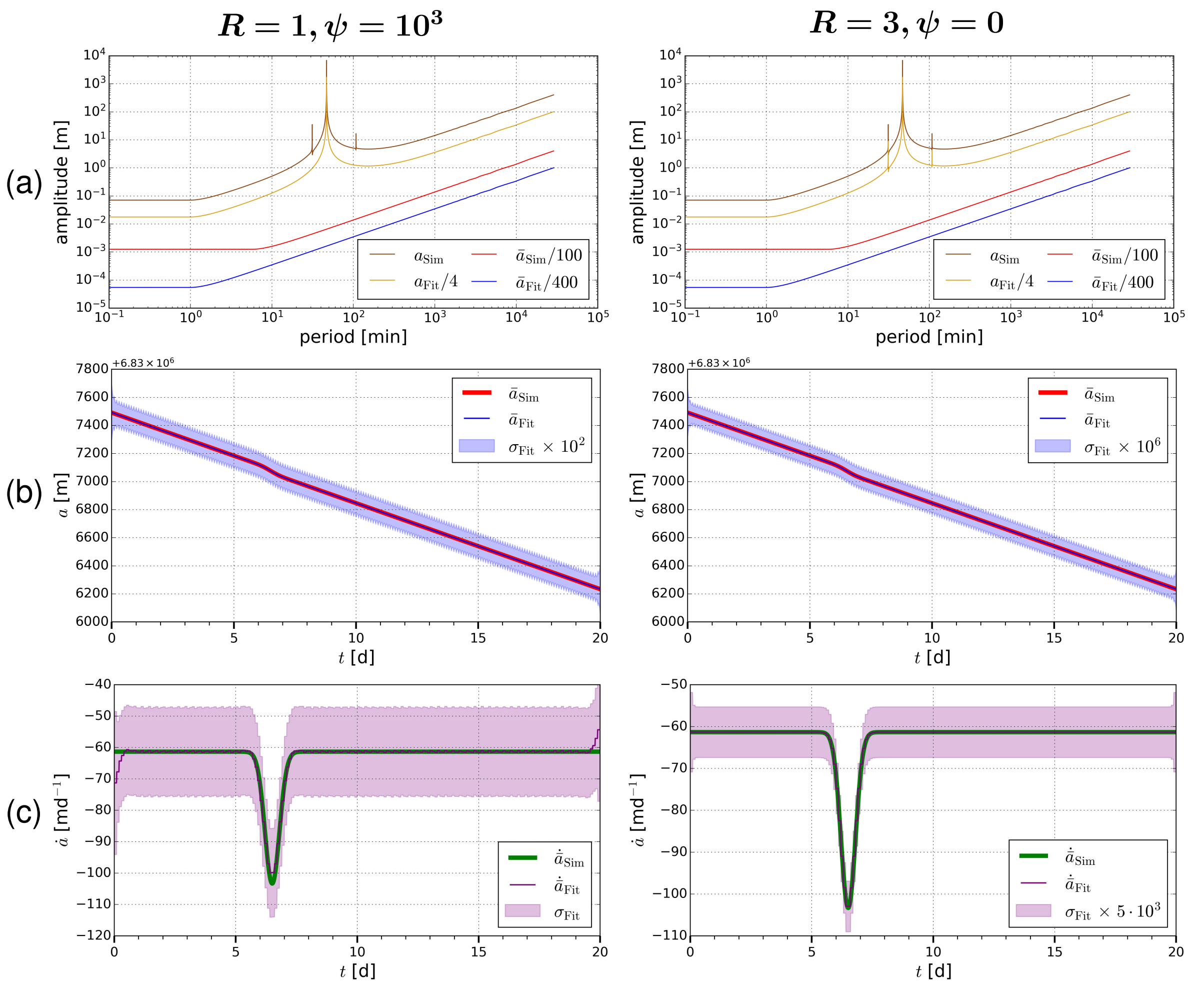

Figure 15: Results from the LSAs performed with $R = 1$ modelled period and constraining factor $\psi = 10^3$ (first column) and with $R = 3$ modelled periods and constraining factor $\psi = 0$ (second column). In (a) the spectra of $a_{\mathrm{Sim}}$ and $a_{\mathrm{Fit}}$, as well as $\bar{a}_{\mathrm{Sim}}$ and $\bar{a}_{\mathrm{Fit}}$ are shown. In (b) the trend function of the simulated data and the trend function of the fitted data along with its error is plotted. In (c) the slopes of the trend functions are shown.

### 4.2.3 Time Dependency of Prominent Periods

This effect is for simplicity only applied to the three prominent periods. Kepler's third law (51) states that $P^2 \propto a^3$. Naturally, Kepler's third law should also apply to the prominent periods from Sect. 4.2.1. With $p_r(t_0) = p_{r,0}$ a prominent period and $a(t_0) = a_0$ the period at a later epoch $t$ is:

$$\left(\frac{p_{r,0}}{p_r(t)}\right)^2 = \left(\frac{a_0}{a(t)}\right)^3 \quad \Longrightarrow \quad p_r(t) = p_{r,0}\left(\frac{a(t)}{a_0}\right)^{\frac{3}{2}} . \tag{54}$$

Strictly speaking, the perturbation of the previous section has to be taken into account because it changes $a(t)$. But because in this simulation the perturbation is of small magnitude and of short duration (note that the kink seen in Fig. 15 (middle row) is small) its impact on the prominent periods is neglected. Moreover, as the satellite sinks, air drag increases due to the spacecraft encountering a higher neutral density. This means that the linear drift $d$ should increase with time and therefore impacts the prominent periods. For simplicity, a constant factor $f \gtrapprox 1$ is multiplied with the linear decrease $d$ in $a(t)$ inside Eq. (54) to account for this effect. Thus, the time dependency of the prominent periods is:

$$p_r(t) = p_{r,0}\left(1 + \frac{d \cdot t}{a_0} \cdot f\right)^{\frac{3}{2}} . \tag{55}$$

For the simulation the factor is set to $f = 1.01$. This means that after 20 d $p_1$ is smaller by 0.76 s, $p_2$ is smaller by 0.51 s and $p_3$ is smaller by 1.76 s.

The LSA with $R = 1$ is performed with $\psi = 10^3$ and the estimated a posteriori standard deviation of unit weight is $m_0 = 31.99\,\mathrm{m}$ differing only little from the $m_0$ obtained in the previous section. The results for this LSA are shown in Fig. 16 (first column). The LSA with $R = 3$ is performed with $\psi = 0$ and the estimated a posteriori standard deviation of unit weight is $m_0 = 10.09\,\mathrm{mm}$. The results for this LSA are also shown in Fig. 16 (second column).

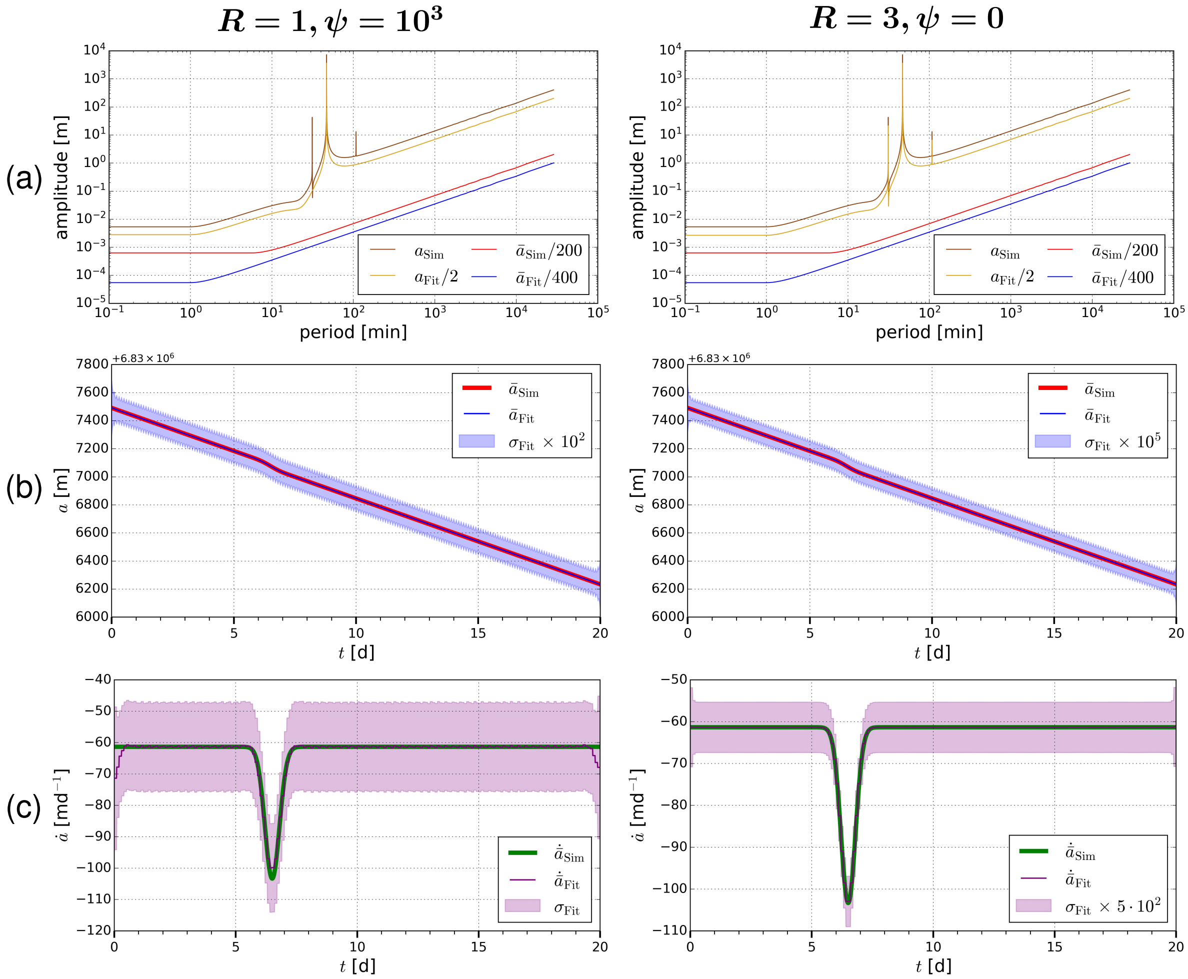

Figure 16: Results from the LSAs performed with $R = 1$ modelled period and constraining factor $\psi = 10^3$ (first column) and with $R = 3$ modelled periods and constraining factor $\psi = 0$ (second column). In (a) the spectra of $a_{\mathrm{Sim}}$ and $a_{\mathrm{Fit}}$, as well as $\bar{a}_{\mathrm{Sim}}$ and $\bar{a}_{\mathrm{Fit}}$ are shown. In (b) the trend function of the simulated data and the trend function of the fitted data along with its error is plotted. In (c) the slopes of the trend functions are shown.

The top row of Fig. 16 shows the spectra of simulated and fitted data as well as of the trend functions of the simulated and the fitted data, the middle row displays the trend functions and in the bottom row the slopes of the trend functions are shown.

The new time dependency of the prominent periods deforms the spectra of the simulated and the fitted data. The spectra are generally a little lower in amplitude but a change in amplitude of the prominent periods is not noticeable and above $10^3$ min the spectra look identical to those of the previous section. As the spectrum of $a_{\mathrm{Fit}}$ is deformed in the same way like the spectrum of $a_{\mathrm{Sim}}$ shows, that the fit model is able to adapt to a time dependency of the prominent periods.

Regarding the trend functions, for the case of $R = 3$ and $\psi = 0$, the only difference to the plots of the previous section is that the error of $\bar{a}_{\mathrm{Fit}}$ is scaled by one order of magnitude less than in Sect. 4.2.2 to improve the readability.

In the case of $R = 1$ and $\psi = 10^3$ the results for the slope of the trend function do not differ noticeably to those obtained in the previous section. In the case of $R = 3$ and $\psi = 0$ the error of $\dot{\bar{a}}_{\mathrm{Fit}}$ is now in the cm range. Otherwise the results do not differ from those obtained in the previous section.

The results show that the fit model is able to handle the time dependency of the prominent periods given in Eq. (55). In the case where no constraining is applied in the LSA, the errors in the results increase by one order of magnitude if the time dependency of the modelled periods is not taken into account in the fit model. In the case where constraining is applied, no change in the results is noticeable.

### 4.2.4 Short Periods

In this work, periods are considered as short if they are shorter than half of the orbital period. Short periods $p_{\mathrm{hf}}$, their amplitudes $A_{\mathrm{hf}}$ and phases $\phi_{\mathrm{hf}}$ are randomly generated with a uniform distribution. The periods are generated as $p_{\mathrm{hf}} = 1,440 \cdot 10^{\rho}$ min, with $\rho$ being a random (uniformly distributed) number in the interval $[-2.5, -1.8]$. The amplitudes are random (uniformly distributed) numbers in the interval $[0.5, 5]$ m. The phases are random (uniformly distributed) numbers inside the interval $[0, 2\pi]$. 50 short periods are generated this way.

The random numbers are generated via the *numpy.random.default_rng()* function from NumPy in Python. With *seed=None* a fresh, unpredictable entropy is pulled from the operating system (Numpy.org, accessed on 2024.08.03). This means that in each run of simulating data, the numbers are different, as they are generated with a different seed. Multiple simulations showed, that different seeds do not require a different constraining factor and barely impact the a posteriori standard deviation of unit weight (not shown).

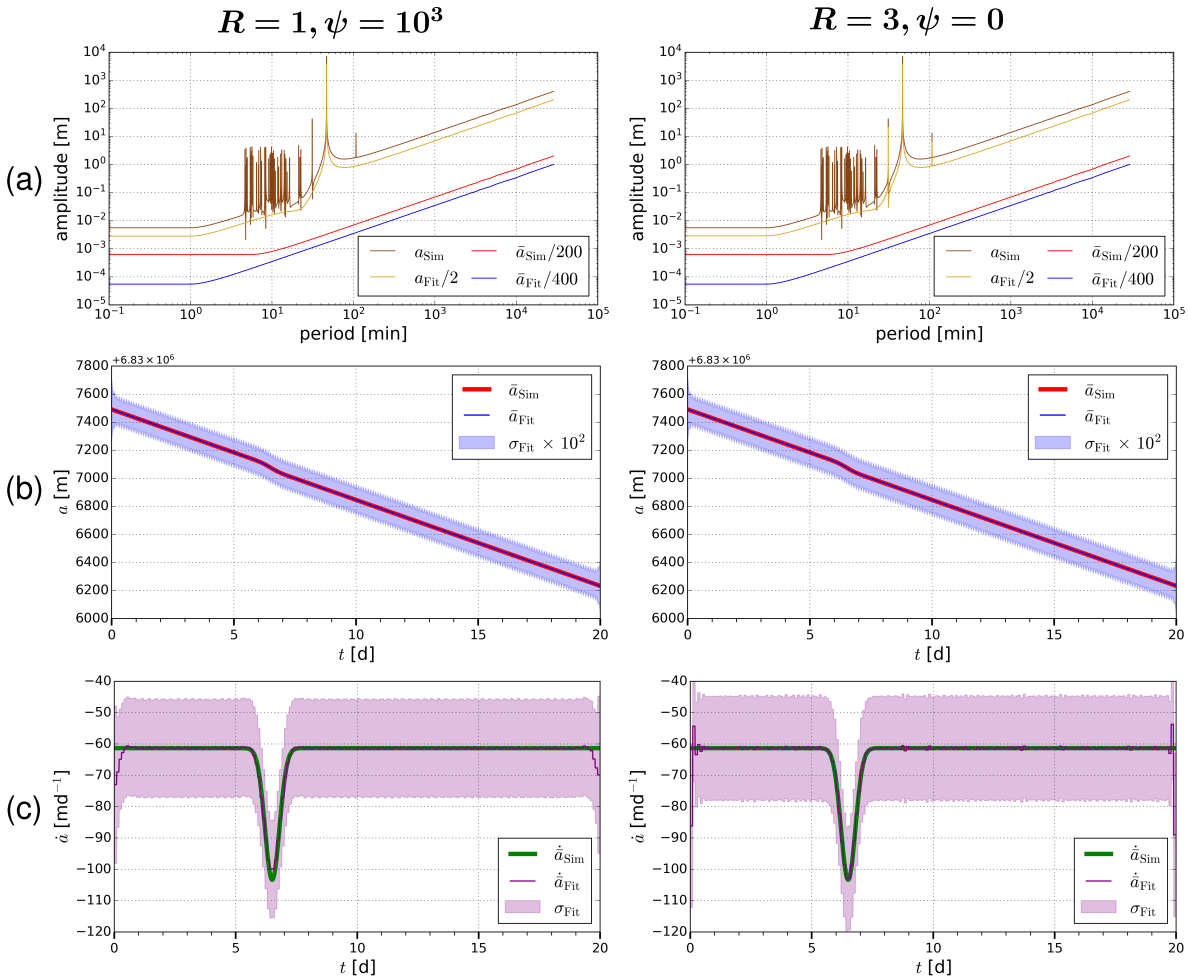

Figure 17: Results from the LSAs performed with $R = 1$ modelled period and constraining factor $\psi = 10^3$ (first column) and with $R = 3$ modelled periods and constraining factor $\psi = 0$ (second column). In (a) the spectra of $a_{\mathrm{Sim}}$ and $a_{\mathrm{Fit}}$, as well as $\bar{a}_{\mathrm{Sim}}$ and $\bar{a}_{\mathrm{Fit}}$ are shown. In (b) the trend function of the simulated data and the trend function of the fitted data along with its error is plotted. In (c) the slopes of the trend functions are shown.

The LSA with $R = 1$ is performed with $\psi = 10^3$ and the estimated a posteriori standard deviation of unit weight is $m_0 = 35.28\,\mathrm{m}$. It is larger by a factor of 1.1 than the $m_0$ obtained in the previous section which shows that even though the short periods influence the results, their impact is suppressed by the constraining factor. The results for this LSA are shown in Fig. 17 (first column). The LSA with $R = 3$ is performed with $\psi = 0$ and the estimated a posteriori standard deviation of unit weight is with $m_0 = 14.97\,\mathrm{m}$ larger by a factor of 1.484 than the $m_0$ obtained in the previous section. The results for this LSA are also shown in Fig. 17 (second column).

The top row of Fig. 17 shows the spectra of simulated and fitted data as well as of the trend functions of the simulated and the fitted data, the middle row displays the trend functions and in the bottom row the slopes of the trend functions are shown.
The new short periods are prominently visible in the spectrum of $a_{\mathrm{Sim}}$. They do not seem to affect the spectra of $a_{\mathrm{Fit}}$ and $\bar{a}_{\mathrm{Fit}}$.
Regarding the trend function, for the case of $R = 3$ and $\psi = 0$ the only difference to the plot of the previous section is that the error of $\bar{a}_{\mathrm{Fit}}$ is now scaled by the same factor as in the case of $R = 1$ and $\psi = 10^3$. The error of $\bar{a}_{\mathrm{Fit}}$ is similar for both cases.
In both cases the error band of $\dot{\bar{a}}_{\mathrm{Fit}}$ now ranges from about $-45\,\mathrm{md}^{-1}$ to about $-77.5\,\mathrm{md}^{-1}$ during quiet times and $\dot{\bar{a}}_{\mathrm{Fit}}$ itself does not differ greatly from $\dot{\bar{a}}_{\mathrm{Sim}}$. The fit model for $R = 3$ and $\psi = 0$ now also needs some time to calibrate as indicated by the large deviations from $\dot{\bar{a}}_{\mathrm{Fit}}$ to $\dot{\bar{a}}_{\mathrm{Sim}}$ at the beginning and at the end of the time interval.

The results from this simulation show that the quality of an unconstrained LSA suffers from the disturbances caused by short periods. Additionally, the results indicate that the error of the LSA with $R = 1$ and $\psi = 10^3$ slightly increases as well.

### 4.2.5 Long Periods

In this work, periods are considered as long if they are longer than half of the orbital period. Long periods $p_{\mathrm{lf}}$, their amplitudes $A_{\mathrm{lf}}$ and phases $\phi_{\mathrm{lf}}$ are randomly generated with a uniform distribution characteristic similarly to the short periods from the previous section. The periods are generated as $p_{\mathrm{lf}} = 1,440 \cdot 10^{\rho}\,\mathrm{min}$, with $\rho$ being a random (uniformly distributed) number in the interval $[-1.15, -0.5]$. The amplitudes are rather larger and are random (uniformly distributed) numbers lying inside the interval $[1, 10]\,\mathrm{m}$. The phases are random (uniformly distributed) numbers inside the interval $[0, 2\pi]$. 10 long periods are generated this way.

The LSA with $R = 1$ is performed with $\psi = 10^3$ and the estimated a posteriori standard deviation of unit weight is $m_0 = 37.80\,\mathrm{m}$. The results for this LSA are shown in Fig. 18 (first column). The LSA with $R = 3$ is also performed with $\psi = 10^3$ (to obtain results of adequate quality) and the estimated a posteriori standard deviation of unit weight is $m_0 = 19.38\,\mathrm{m}$. The results for this LSA are also shown in Fig. 18 (second column).

The top row of Fig. 18 shows the spectra of simulated and fitted data as well as of the trend functions of the simulated and the fitted data, the middle row displays the trend functions and in the bottom row the slopes of the trend functions are shown.
The new long periods are visible in the spectrum of $a_{\mathrm{Sim}}$. Interestingly, in the case of $R = 3$ two long periods of 115 min and 127 min are also visible (the second long period is only barely visible) in the spectrum of $a_{\mathrm{Fit}}$, but $\bar{a}_{\mathrm{Fit}}$ does not change. This may be connected with the fact, that these two long periods are very close to the third prominent period $p_3$ because they are not visible in the spectrum of $\bar{a}_{\mathrm{Fit}}$ but further simulations may be performed to investigate this interesting feature.
Regarding the trend functions, for the case of $R = 3$ the error is slightly smaller than in the previous section due to the constraining. For the case of $R = 1$ the error is slightly larger than in the previous section due to the new long periods.
The slope $\dot{\bar{a}}_{\mathrm{Fit}}$ with $R = 1$ looks similar to the slope $\dot{\bar{a}}_{\mathrm{Fit}}$ with $R = 3$. The error band of $\dot{\bar{a}}_{\mathrm{Fit}}$ ranges from about $-40\,\mathrm{md}^{-1}$ to about $-82.5\,\mathrm{md}^{-1}$ during quiet times in the case of $R = 1$. In the case of $R = 3$ the error band of $\dot{\bar{a}}_{\mathrm{Fit}}$ ranges from about $-47.5\,\mathrm{md}^{-1}$ to about $-75\,\mathrm{md}^{-1}$ during quiet times. In both cases of $R$, $\dot{\bar{a}}_{\mathrm{Fit}}$ reaches a peak value of $-101\,\mathrm{md}^{-1}$ during the Gaussian perturbation. Interestingly, during quiet times the pattern of the values of $\dot{\bar{a}}_{\mathrm{Fit}}$ are similar to a beat pattern with a beat period of approximately 4 days. $\dot{\bar{a}}_{\mathrm{Fit}}$ deviates from $\dot{\bar{a}}_{\mathrm{Sim}}$ up to about $-6\,\mathrm{md}^{-1}$ during quiet times. If the LSA with $R = 3$ is performed with $\psi = 0$ values of $\dot{\bar{a}}_{\mathrm{Fit}}$ deviate up to several $100\,\mathrm{md}^{-1}$ from $d$.

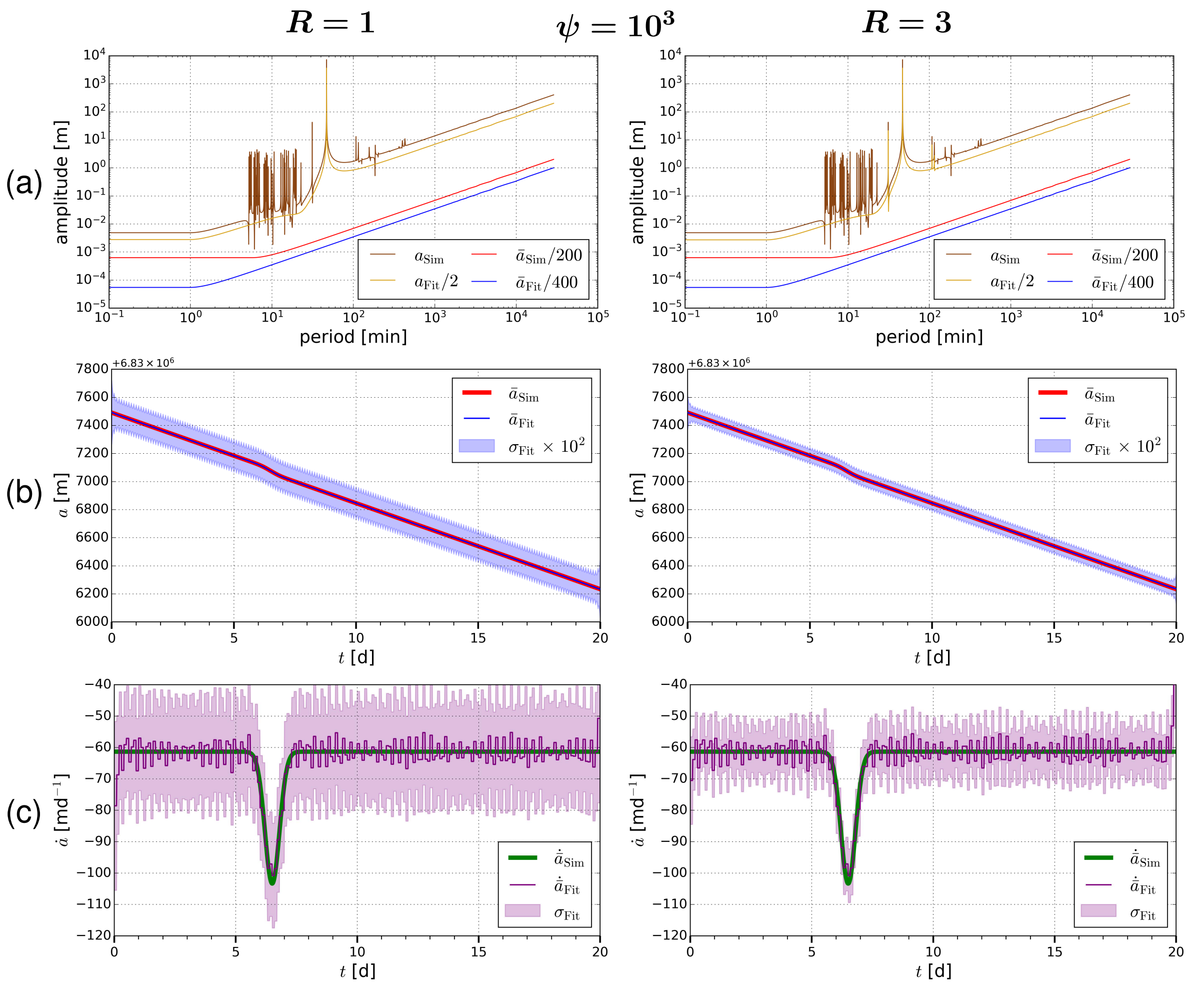

Figure 18: Results from the LSAs performed with $R = 1$ modelled period and constraining factor $\psi = 10^3$ (first column) and with $R = 3$ modelled periods and constraining factor $\psi = 10^3$ (second column). In (a) the spectra of $a_{\mathrm{Sim}}$ and $a_{\mathrm{Fit}}$, as well as $\bar{a}_{\mathrm{Sim}}$ and $\bar{a}_{\mathrm{Fit}}$ are shown. In (b) the trend function of the simulated data and the trend function of the fitted data along with its error is plotted. In (c) the slopes of the trend functions are shown. In both cases of $R$ there is scattering visible in the slopes of the trend functions.

The results show that the quality of the LSAs suffers greatly from the disturbances caused by long periods with rather large amplitudes. Additionally, modelling more prominent periods lowers the errors of both the trend function and its slope. Of course this comes with the cost of increased computation time. Alternatively, a higher constraining factor can be used to suppress the impact of long periods on the results.

Therefore, additional LSAs for $R = 1$ and $R = 3$ are performed with $\psi = 10^5$. The error of the fit is $m_0 = 37.88\,\mathrm{m}$ for $R = 1$ and for $R = 3$ it is $m_0 = 20.35\,\mathrm{m}$. In Fig. 19 the results are shown for $R = 1$ (first column) and $R = 3$ (second column) are shown.

The top row of Fig. 19 shows again the spectra of the simulated data and its trend function as well as the spectra of the fitted data and its trend function with the new setting of the constraining. The middle row displays the trend functions and in the bottom row the slopes of the trend functions are shown.
In the case of $R = 3$ the two long periods of 115 min and 127 min are not visible anymore in the spectrum of $a_{\mathrm{Fit}}$.
In both cases of $R$ the kink in $\bar{a}_{\mathrm{Fit}}$ due to the Gaussian perturbation is significantly smaller due to the stronger constraining.
The slope $\dot{\bar{a}}_{\mathrm{Fit}}$ with $R = 1$ looks identical to the slope $\dot{\bar{a}}_{\mathrm{Fit}}$ with $R = 3$. The error band of $\dot{\bar{a}}_{\mathrm{Fit}}$ ranges from about $-52.5\,\mathrm{md}^{-1}$ to about $-70\,\mathrm{md}^{-1}$ during quiet times in the case of $R = 1$. In the case of $R = 3$ the error band of $\dot{\bar{a}}_{\mathrm{Fit}}$ ranges from about $-55\,\mathrm{md}^{-1}$ to about $-65\,\mathrm{md}^{-1}$ during quiet times. In

both cases of $R$, $\dot{\bar{a}}_{\mathrm{Fit}}$ reaches a peak value of $-82.5\,\mathrm{md}^{-1}$ during the Gaussian perturbation. Due to the stronger constraining of neighbouring slopes the reproduced slope during the Gaussian perturbation is damped in intensity and stretched in duration. Interestingly, at the roots (beginning and end) of the Gaussian perturbation $\dot{\bar{a}}_{\mathrm{Fit}}$ increases by approximately $1\,\mathrm{md}^{-1}$ before it drops down.

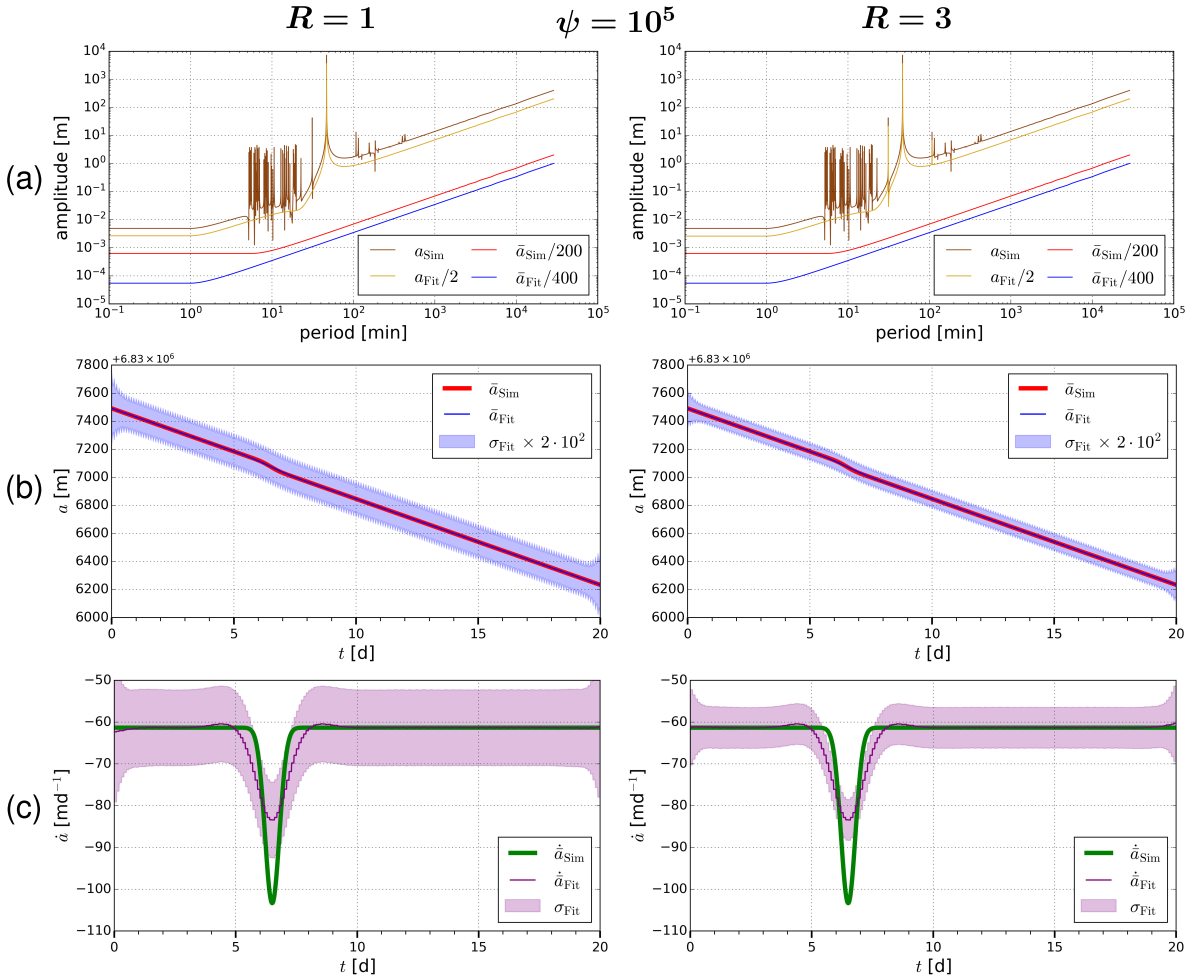

Figure 19: Results from the LSAs performed with $R = 1$ modelled period and constraining factor $\psi = 10^5$ (first column) and with $R = 3$ modelled period and constraining factor $\psi = 10^5$ (second column). In (a) the spectra of $a_{\mathrm{Sim}}$ and $a_{\mathrm{Fit}}$, as well as $\bar{a}_{\mathrm{Sim}}$ and $\bar{a}_{\mathrm{Fit}}$ are shown. In (b) the trend function of the simulated data and the trend function of the fitted data along with its error is plotted. In (c) the slopes of the trend functions are shown.

The results show that the quality of the orbital slope during quiet times greatly increases with stronger constraining. In addition, the error of $\bar{a}_{\mathrm{Fit}}$ and $\dot{\bar{a}}_{\mathrm{Fit}}$ decrease with stronger constraining. However, a stronger constraining leads to greater underestimation of the peak value of orbital decay achieved during a magnetic storm and the duration of the storm is overestimated. Moreover, at the roots of a Gaussian perturbation there is slight increase in the orbital slope before the large decrease due to the storm.

## 4.3 RK4 Method Applied to Gauss's Perturbation Equation for the Semi-Major Axis

The numerical integration starts with the initial value $a_{\mathrm{Gauss}}(t_0)$, which corresponds to the osculating element from the orbit estimated by BSW at the epoch $t_0$. To directly compare the results $\bar{a}_{\mathrm{Fit}}$ and $a_{\mathrm{Gauss}}$, the latter has to be shifted. This is because $\bar{a}_{\mathrm{Fit}}$ corresponds to the mean semi-major axis but $a_{\mathrm{Gauss}}(t_0)$ taken from the orbit estimated by the BSW corresponds to the osculating semi-major axis, which is impacted by all the gravitational perturbations such as the strong perturbation caused by $C_{2,0}$ (see Fig. 5 as example). It is thus useful to shift $a_{\mathrm{Gauss}}$ in such a way that $a_{\mathrm{Gauss}}(t_0)$ is the same as $\bar{a}_{\mathrm{Fit}}$

at $t_0$. When several LSAs with different settings are performed (in the results 5, always multiple LSAs with different constraining factors are performed) $a_{\mathrm{Gauss}}(t_0)$ is shifted to the mean of all $\bar{a}_{\mathrm{Fit}}$ at $t_0$:

$$a_{\mathrm{Gauss}}(t) \quad \rightarrow \quad a_{\mathrm{Gauss}}(t) + \langle \bar{a}_{\mathrm{Fit}} \rangle (t_0) - a_{\mathrm{Gauss}}(t_0) \tag{56}$$

As $a_{\mathrm{Gauss}}$ is propagated values for $\dot{a}_{\mathrm{Gauss}}$ are obtained simultaneously from Eq. (11). It should be noted that it is not reasonable to simply take the time series of the osculating elements and plug them with the acceleration values $R$ and $S$ (taken from the PCAs or ACC data) into Eq. (11) to obtain a time series for $\dot{a}_{\mathrm{Gauss}}$ because the time series of the osculating semi-major axis contains also gravitational perturbations (e.g., due to $C_{2,0}$).

The numerical value used for $\gamma$ (assumed as error-free) is

$$\gamma = G \cdot M_{\mathrm{Earth}} = 2.975319 \cdot 10^{24} \frac{\mathrm{m}^3}{\mathrm{d}^2}. \tag{57}$$

The eccentricity $e$ and the argument of perigee $\omega$ are taken as constant. In both cases the constant is defined as the first value in the time series of the osculating elements obtained from the orbits estimated by BSW. As BSW estimates daily orbits, the errors of $e$, $\omega$ and the starting error of $a_{\mathrm{Gauss}}$ is taken as the mean of the daily errors in the time interval.

The values for the time dependent argument of latitude $u$ is taken from the orbits estimated by BSW. For simplicity, the error $\sigma_u$ is neglected. The values for the accelerations in radial direction and in along-track direction are taken from the ACC data or the PCA data, respectively. Their errors are neglected as well for simplicity.

It should again be emphasised, that for the orbit propagation only PCAs from the NL orbits are to be used. PCAs from the NG orbits do not contain (or only traces of) the air drag as it is already explicitly modelled. In the case of the osculating elements $a$, $e$, $\omega$ and $u$ the choice between NL and NG orbits is less important as the differences are small (see Fig. 9 as example for $a$).

In the following, the partial derivatives of Eq. (11) with respect to $a_{\mathrm{Gauss}}$, $e$ and $\omega$ are listed explicitly:

$$\left(\frac{\partial \dot{a}_{\mathrm{Gauss}}}{\partial a_{\mathrm{Gauss}}}\right)^2 = \frac{9 a_{\mathrm{Gauss}}}{\gamma(1-e^2)} \Big\{ e \sin(u-\omega) R + \big[1 + e\cos(u-\omega)\big] S \Big\}^2 \tag{58}$$

$$\left(\frac{\partial \dot{a}_{\mathrm{Gauss}}}{\partial e}\right)^2 = \frac{4 a_{\mathrm{Gauss}}^3}{\gamma(1-e^2)^3} \Big\{ \sin(u-\omega) R + \big[e + \cos(u-\omega)\big] S \Big\}^2 \tag{59}$$

$$\left(\frac{\partial \dot{a}_{\mathrm{Gauss}}}{\partial \omega}\right)^2 = \frac{4 a_{\mathrm{Gauss}}^3 e^2}{\gamma(1-e^2)} \Big\{ \cos(u-\omega) R - \sin(u-\omega) S \Big\}^2. \tag{60}$$

These partial derivatives (evaluated at time $t_n$) are then inserted into Eq. (18):

$$\sigma_{k_1}^2 = \lambda^2 \left\{ \left(\frac{\partial \dot{a}_{\mathrm{Gauss}}}{\partial a_{\mathrm{Gauss}}}\right)^2 \cdot \sigma_{a_{\mathrm{Gauss}}}^2 + \left(\frac{\partial \dot{a}_{\mathrm{Gauss}}}{\partial e}\right)^2 \cdot \sigma_e^2 + \left(\frac{\partial \dot{a}_{\mathrm{Gauss}}}{\partial \omega}\right)^2 \cdot \sigma_\omega^2 \right\}. \tag{61}$$

The partial derivatives in (19), (20) and (21) are analogous.

# 5 Results

Different intervals during the years 2018, 2023 and 2024 are analysed in this work. GRACE-FO-1 data from the years 2018 and 2023 are analysed. Swarm-A is analysed in the years 2023 and 2024. Sentinel-1A is only analysed in the year 2023. Sentinel-2A and Sentinel-3A are only analysed in the year 2024. In all figures the CME arrival times are indicated with vertical yellow dotted lines and black bars show the three-hourly *ap* index. In the case of the Sentinel satellites, the starting time (they are usually of short duration) of MANs are indicated with vertical brown dotted lines.

For the years 2018 and 2023 both NL and NG orbits have been estimated. For those years the osculating elements from the NG orbit are used for the fit model approach and the Gaussian approach. For these years the $\beta$ angle and the modelled air density have also been provided. For the analysis in the year

2024 only NL orbits are used. Thus, for 2024 the osculating elements from the NL orbits are used for both the fit model approach and the Gaussian approach. Moreover, for 2024 the $\beta$ angle is not analysed and since the NL orbits do not model non-gravitational accelerations the air density is not modelled.

Usually, the sampling of the osculating elements, the modelled air density and the $\beta$ angle is 30 s. As PCAs are constant for a duration of 6 min, resampling them to 30 s is straightforward. However, for the integration approach in the case of GRACE-FO-1 in the year 2018 the osculating elements are calculated with a sampling of 5 s (the argument of latitude $u$ is needed for integration) and the PCAs are resampled to 5 s as well because the 1 s sampled ACC data is down-sampled to this value (to reduce computation load). For the fit model approach the osculating elements are then down sampled to 30 s to reduce the computation load.

The fit model approach is always executed with $n_{\mathrm{fac}} = 10$ (ten subintervals are fitted per day). For most satellites only one period is fitted $R = 1$. This one period always corresponds to half of the orbital period. For GRACE-FO-1 in the year 2018 an additional period is fitted (see Sect. 5.1.1). The fit model is applied three times with different constraining factors. The three constraining factors are always $\psi_1 = 10^3$, $\psi_2 = 10^4$ and $\psi_3 = 10^5$. As mentioned before, the observations are not weighted and the a priori standard deviation of unit weight is set to $\sigma_0 = 1\,\mathrm{m}$.

Let $k \in \{1, 2, 3\}$ and let $\Lambda \in \{\mathrm{PCA}, \mathrm{ACC}, (\mathrm{ACC{,}shifted})\}$. The variable $\bar{a}_{\psi_k}$ denotes the extracted trend function from the fit model, that is estimated with $\psi_k$. Similarly, $\dot{\bar{a}}_{\psi_k}$ denotes the orbital slope evaluated with the fit model with weighting factor $\psi_k$. For the integration approach, $a_\Lambda$ indicates the numerically integrated semi-major axis with $\Lambda$ as input for the accelerations in Eq. 11 and $\dot{a}_\Lambda$ denotes the corresponding slope. The variable $\sigma$ denotes the corresponding error. For example, in a plot showing the slope, $\sigma_{\mathrm{PCA}}$ denotes the error band of $\dot{a}_{\mathrm{PCA}}$ and $\sigma_{\psi_1}$ denotes the error band of $\dot{\bar{a}}_{\psi_1}$. And in a plot where the semi-major axis is shown, $\sigma_{\mathrm{PCA}}$ denotes the error band of $a_{\mathrm{PCA}}$ and $\sigma_{\psi_1}$ denotes the error band of $\bar{a}_{\psi_1}$.

The slope obtained with the integration approach always exhibits large oscillations. These oscillations stem from the $R$ and the $S$ accelerations in Eq. (11). Results where the slopes (obtained with the Gaussian approach) as well as their error bands are smoothed are also shown to enable easier interpretation of the results. The smoothing is done with a SG filter of degree 0, i.e., with a moving average, and an optimally determined window length. The whole procedure (finding the optimal smoothing period and the smoothing process itself) is explained in the Appendix A. The smoothing periods are determined explicitly in Sect. A.3.1. The smoothed slope is denoted as $\tilde{\dot{a}}_\Lambda$ and the corresponding error band is denoted as $\tilde{\sigma}_\Lambda$. For all satellites there are spikes observable at day boundaries in $\tilde{\dot{a}}_{\mathrm{PCA}}$. This is probably due to the quality of PCAs decreasing at day boundaries (see Sect. 3.1).

For GRACE-FO-1 and Swarm-A additional figures show the rough ratio of increase in orbital decay during a geomagnetic storm compared to usual orbital decay. The ratio is simply the slope divided by the mean value of the slope calculated over the corresponding entire time interval. The mean values are listed in a corresponding table or explicitly stated. This procedure is not done for the Sentinel satellites because MANs heavily distort the mean values.

## 5.1 Results for the Year 2018

Figure 20 shows the time series of the *Dst* and the *AE* index from 2018-08-10 to 2018-10-22. Additionally, the arrival times of two consecutive CMEs on Earth are shown. After the second CME event on 2018-08-25, a sharp decrease from about 20 nT on 2023-08-25 to about −175 nT is observed for the *Dst* index on 2023-08-26. The *AE* index is about 50 nT on 2023-08-25 and on 2023-08-26 it reaches 1,200 nT twice. On 2018-09-11 the *Dst* Index drops below −50 nT and the *AE* index reaches values above 1,200 nT without any prior CME arrival. Many drops in the *Dst* index are in accordance with spikes in the *AE* index. However, these take place without any prior CME arrival.

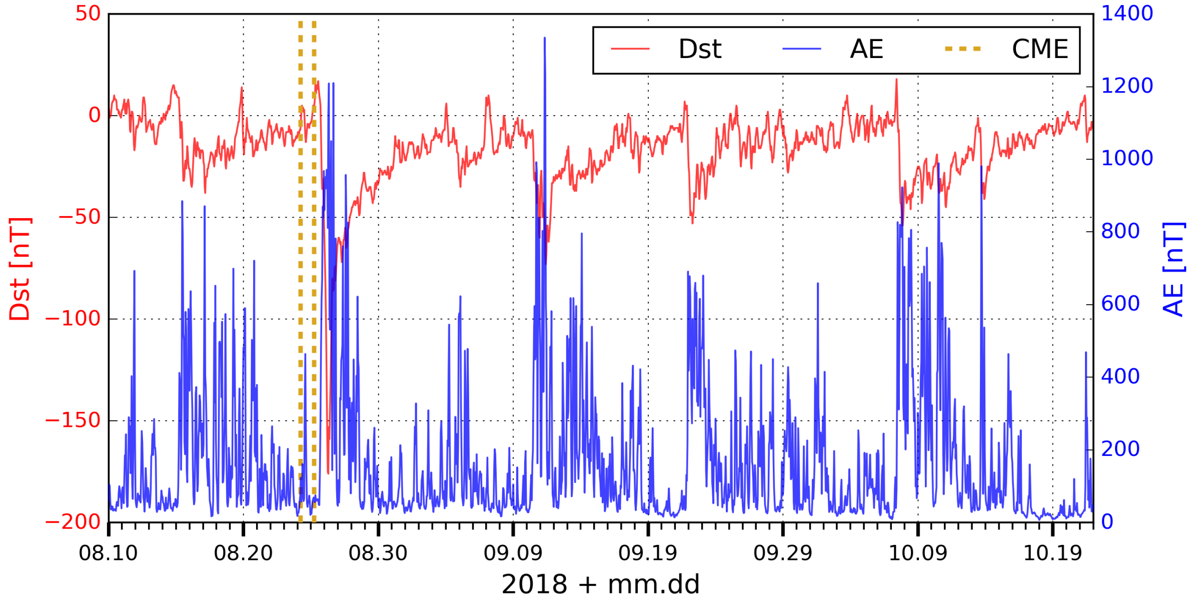

Figure 20: *Dst* and *AE* index in 2018. CME arrival times are indicated with vertical yellow dotted lines.

### 5.1.1 GRACE-FO-1

#### 5.1.1.1 Fit Model Approach

The fit model is applied to the time interval 2018-08-10 to 2018-10-10. In Fig. 21 (left) a main peak at $p_1 = 47.30\,\mathrm{min}$ is visible in the spectrum of the osculating semi-major axis. The main driver of this period is the $C_{2,0}$ perturbation. When the fit model is applied with $R = 1$, the results of the fit model are of bad quality. It turns out, that a very long ($p \gtrsim 1\,\mathrm{d}$) period $p_2 = 7.99 \cdot 10^3\,\mathrm{min}$ ($= 5.55\,\mathrm{d}$) causes major disturbances. An increase in $\psi$ would suppress this perturbation but this would also suppress local trends induced by potential geomagnetic storms. For this reason the fit model is applied with $R = 2$ and $p_2$ being the very long period mentioned before. An interval length of 61 days is chosen because this duration is close to an integer multiple of $p_2$ and therefore $p_2$ is easier to detect in the spectrum seen in Fig. 21 (left) which simplifies the determination of its numerical value.

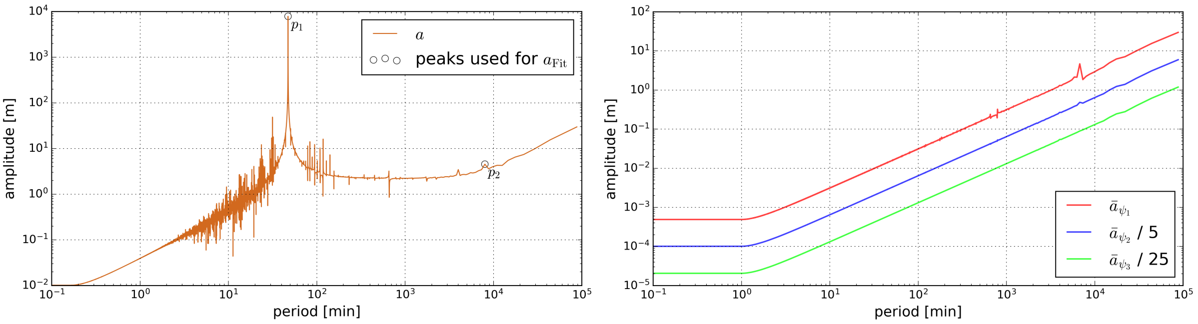

Figure 21: Spectrum of the semi-major axis of GRACE-FO-1 from 2018-08-10 to 2018-10-10 (left) and the spectra of the trend functions of the fit model approach (right). In the spectrum of the semi-major axis the two periods used for the LSA are marked with black circles.

Table 3 shows for each LSA the estimated a posteriori standard deviations of unit weight and the mean slope of the semi-major axis. For each choice of $\psi$ a value of $m_0 \approx 60\,\mathrm{m}$ is obtained.

In Fig. 21 (right) the spectra of the extracted $\bar{a}_{\mathrm{Fit}}$ of the LSAs are shown, which appear as almost flat curves in the shown period range. For $\psi_1$ there are multiple periods below $10^3\,\mathrm{min}$ that stick out and a major period between $6 \cdot 10^3\,\mathrm{min}$ and $7 \cdot 10^3\,\mathrm{min}$ is visible.

Table 3: Errors of the LSAs of the fit model and mean slope of the semi-major axis with different constraining factors $\psi$ for GRACE-FO-1 in the year 2018.

| $\psi$ | $m_0$ [m] | $\langle \dot{a} \rangle$ $[\frac{\text{m}}{\text{d}}]$ |
|---|---|---|
| $\psi_1$ | 59.87 | -1.41 |
| $\psi_2$ | 60.12 | -1.45 |
| $\psi_3$ | 60.15 | -1.48 |

In Fig. 22 (top row) the function $\bar{a}_{\text{Fit}}$ is shown for the different choices of $\psi$ for the entire time interval as well as for a shorter time interval from 2018-08-24 to 2018-08-29. Oscillations are visible for $\psi_1$. For $\psi_2$ and $\psi_3$ these oscillations are damped in a way that the two curves almost overlap with the exception at the beginning and at the end of the time interval. The orbital decay of GRACE-FO-1 amounts to about 90 m during the time interval of 61 d.

In Fig. 22 (bottom) the slope of the semi-major axis is shown on the left, whereas on the right it is divided by the mean value of the slope of the semi-major axis (calculated over the time interval from 2018-08-10 to 2018-10-10). For $\psi_1$ oscillations lead to positive values of $\dot{\bar{a}}$. For $\psi_2$ and $\psi_3$ the values are always negative (disregarding the beginning and the end of the time interval) but the error band always reaches positive values. There is no or only little correlation observable between the behaviour of the slopes and the behaviour of the *ap* index for any choice of $\psi$. It should be noted, that increases in the *ap* index, increases in the *AE* index and decreases in the *Dst* index tend to happen simultaneously.

During the geomagnetic storm starting on 2018-08-26 the largest orbital decays are $\dot{\bar{a}}_{\psi_2} = -3.59\,\text{md}^{-1}$ and $\dot{\bar{a}}_{\psi_3} = -2.57\,\text{md}^{-1}$ (for $\dot{\bar{a}}_{\psi_1}$ oscillations prevent an adequate statement).

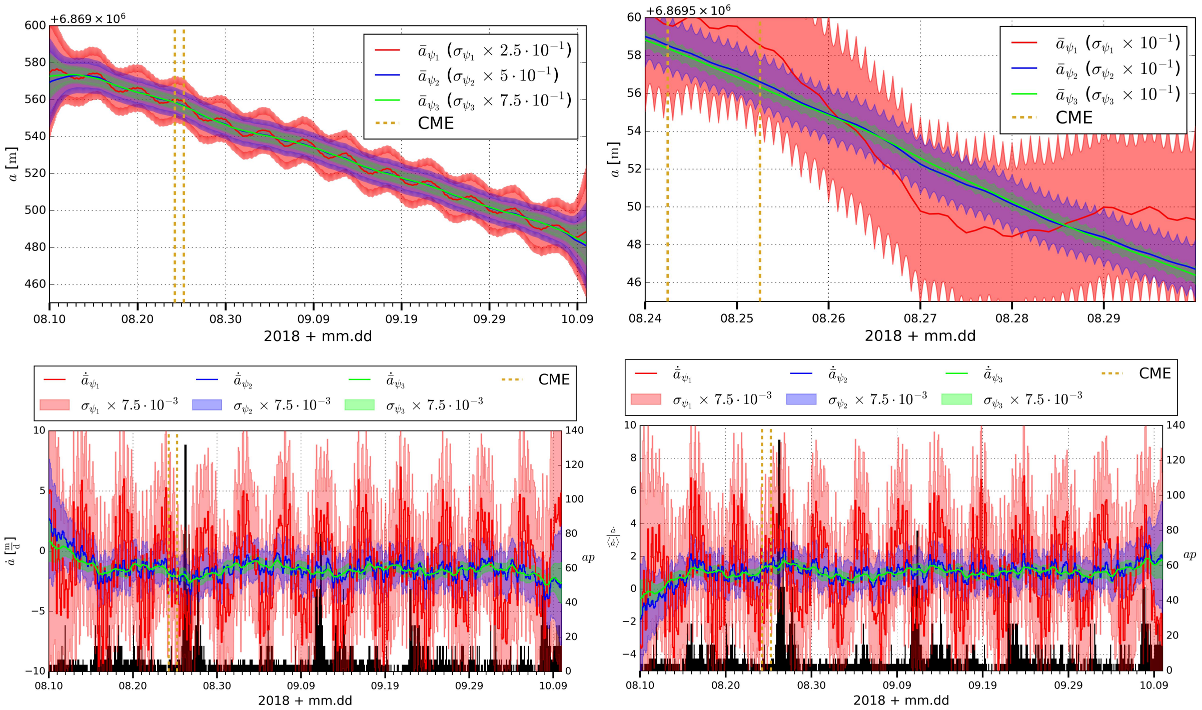

Figure 22: Results of the fit model approach for GRACE-FO-1 in the year 2018. CME arrival times are indicated with vertical yellow dotted lines. Black bars show the *ap* index. The top row shows the trend functions of the fit model approach and a zoom view focused on the time after the arrival of two CMEs. The bottom row shows the calculated slope of the trend function as well as the slope of the trend function divided by the mean value.

It is not yet clear why there is a very long period of $p_2 = 5.55\,\text{d}$ appearing in the spectrum of GRACE-FO-1 in the year 2018. This period is not visible anymore 4.5 years later (see Fig. 28 in Sect. 5.2.1).

As mentioned before, the fit model approach was performed with $R = 2$ because with $R = 1$ the very long period $p_2$ is corrupting the trend functions (not shown here). Interestingly, if $p_2$ is taken into account in the fit model a new prominent very long period $p_3 = 4.69\,\text{d}$ is visible in the spectrum shown in Fig. 21

(right). $p_3$ produces the oscillation behaviour observed in $\bar{a}_{\psi_1}$ seen in Fig. 22 (top, left). It also manifests itself in the slope $\dot{\bar{a}}_{\psi_1}$ seen in Fig. 22 (bottom, left). However this period is not visible in the spectrum of $a$ in Fig. 21 (left) but in the spectrum of the trend in Fig. 21 (right). One possible explanation is that $p_3$ is not visible because of bad period resolution in this range. This is because the spectra are produced for interval length of only 61 d. Another possible explanation is that $p_3$ arises because the numerical value of $p_2$ is determined inaccurately. In another attempt (not shown here) LSAs with $R = 3$ and modelling $p_3$ were executed for a time interval of 30 d (a shorter time interval was chosen due to reasons concerning computation time). But the results were of bad quality as well and no reasonable analysis was possible. To further inspect $p_2$ and $p_3$ they should be determined with more accuracy. Additionally, the evolution of the amplitude of $p_2$ may be researched to investigate its missing presence in the results of 2023. Moreover, it may be advantageous to detrend the time series before computing the spectra.

#### 5.1.1.2 Gaussian Approach

For the Gaussian approach the time interval 2018-08-22 to 2018-10-22 is chosen, because the ACC data is of inadequate quality before 2018-08-22. The interval length is set to 61 days to check if the period $p_2$ from the fit model also appears in any spectrum related to the Gaussian approach. The mean values of $\Gamma \in \{\mathrm{R}, \mathrm{S}, \mathrm{W}\}$ are shown in Tab. 4. The mean values differ between the ACC and PCA cases mainly in the radial and the cross-track direction.

Table 4: Mean accelerations in the local orbital frame for the different data sets.

| | ACC | PCA | ACC, shifted |
|---|---|---|---|
| $\langle \mathrm{R} \rangle\ [\frac{\mathrm{nm}}{\mathrm{s}^2}]$ | -79.740 | -14.632 | -14.632 |
| $\langle \mathrm{S} \rangle\ [\frac{\mathrm{nm}}{\mathrm{s}^2}]$ | -10.738 | -10.736 | -10.736 |
| $\langle \mathrm{W} \rangle\ [\frac{\mathrm{nm}}{\mathrm{s}^2}]$ | -14.803 | 38.743 | 38.743 |

In Fig. 23 the spectrum of $a_{\mathrm{Gauss}}$ is shown for the ACC data, the PCAs and the shifted ACC data (differently scaled to separate the spectra for better visibility). In all spectra two periods of about 94.61 min and 47.30 min are sticking out. These periods correspond to the full and half orbital period, mainly reflecting the once- and twice-per-revolution periodicity of the air drag affecting the satellite. They are of much weaker intensity compared to the spectrum in Fig. 21 (left) because the on-board accelerometer and the PCAs do not measure gravitational accelerations. The spectrum of $a_{\mathrm{PCA}}$ also shows various little spikes between 16 min and 33 min. Apart from that, all spectra appear smooth at the scaling used for the figure.

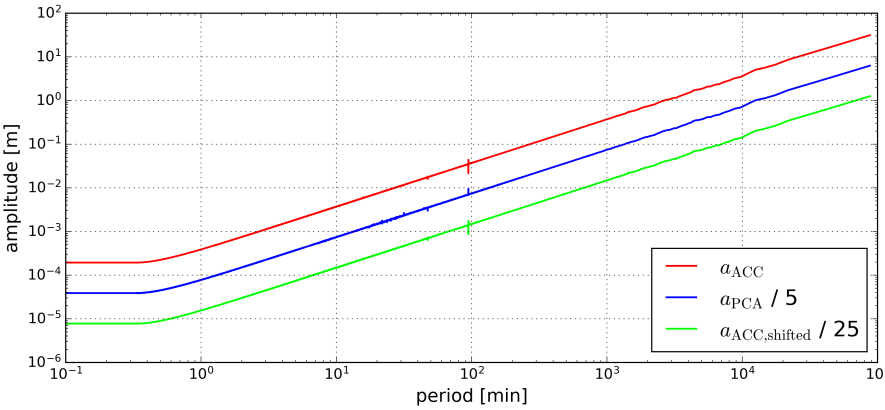

Figure 23: Spectrum of the semi-major axis obtained with the Gaussian approach. The spectrum of the semi-major axis propagated with PCAs and the spectrum of the semi-major axis propagated with shifted ACC values are shifted for better visibility.

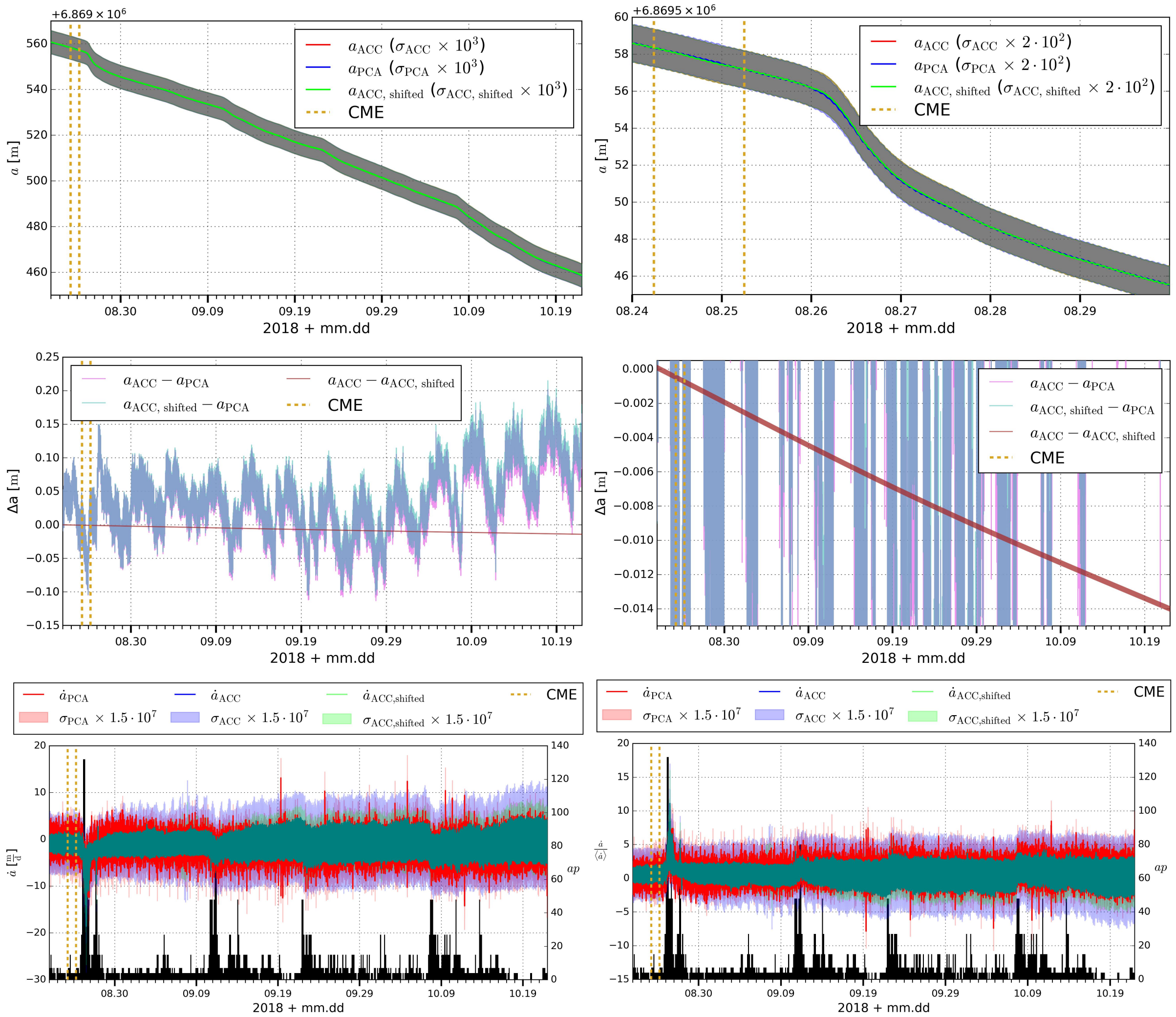

Figure 24: Results of the Gaussian approach for GRACE-FO-1 in the year 2018. The time series of the semi-major axis is shown in the top row. The differences in the semi-major axis are shown in the middle row. The resulting slopes of the semi-major axis and the ratio to its mean value are shown in the bottom row. CME arrival times are indicated with vertical yellow dotted lines. Black bars show the *ap* index.

In Fig. 24 (top, left) $a_{\mathrm{Gauss}}$ is shown for all three data sets for the entire time interval. A major kink is observed on 2018-08-26 and additional minor kinks can be seen on 2018-09-11, 2018-09-22 and 2018-10-07. All curves overlap and the errors have to be scaled for better visibility. The Gaussian approach suggests, that GRACE-FO-1 lost about 100 m of altitude during the time interval.

Figure 24 (top, right) shows $a_{\mathrm{Gauss}}$ during a shorter time interval from 2018-08-24 to 2018-08-29 which encloses the major kink. The curves of $a_{\mathrm{ACC,shifted}}$ and $a_{\mathrm{ACC}}$ still overlap but $a_{\mathrm{PCA}}$ differs from the other two curves. All curves exhibit oscillations but for $a_{\mathrm{PCA}}$ the amplitudes are a little larger. The oscillations of $a_{\mathrm{PCA}}$ are not in phase with those of $a_{\mathrm{ACC}}$ and $a_{\mathrm{ACC,shifted}}$. This may seem a little strange at first but if Fig. 11 (top, right) is inspected more closely, the same pattern can be observed in the S component of the accelerations. The reason for this phase shift is not clear yet. $a_{\mathrm{PCA}}$ is during the second half of the day 2018-08-24 above and during the first half of the day 2018-08-26 (during the major kink) below $a_{\mathrm{ACC}}$ and $a_{\mathrm{ACC,shifted}}$.

Figure 24 (middle row) shows the differences and a vertical cutout in the differences between the different $a_{\mathrm{Gauss}}$ obtained with the three data sets. The differences $a_{\mathrm{ACC}} - a_{\mathrm{PCA}}$ and $a_{\mathrm{ACC,shifted}} - a_{\mathrm{PCA}}$ range from −12 cm to +22 cm. The difference $a_{\mathrm{ACC}} - a_{\mathrm{ACC,shifted}}$ contains oscillations (the difference appears as a thick line because the oscillations are of short-periodic nature) and decreases from 0 mm to −14 mm during the time interval.

In Fig. 24 (bottom row) the slopes $\dot{a}$ and $\frac{\dot{a}}{\langle \dot{a} \rangle}$ are shown. $\dot{a}_{\mathrm{Gauss}}$ exhibits large oscillations for each data set with $\dot{a}_{\mathrm{PCA}}$ showing the largest oscillation behaviour. Due to the large oscillations positive values are consistently reached. The errors have to be scaled by a factor of $1.5 \cdot 10^7$ for visibility. Drops in $\dot{a}_{\mathrm{Gauss}}$ appear on the dates when kinks are visible in $a_{\mathrm{Gauss}}$ for all three data sets. These drops are in accordance with large *ap* values. $a_{\mathrm{ACC}}$ and $a_{\mathrm{ACC,shifted}}$ always overlap.

Table 5: Mean slopes of the semi-major axis obtained with the Gaussian approach for GRACE-FO-1 in the year 2018.

| | $\langle \dot{a} \rangle$ $[\frac{\mathrm{m}}{\mathrm{d}}]$ | $\langle \tilde{\dot{a}} \rangle$ $[\frac{\mathrm{m}}{\mathrm{d}}]$ |
|---|---|---|
| ACC | -1.68 | -1.68 |
| PCA | -1.67 | -1.67 |
| ACC, shifted | -1.67 | -1.67 |

In Tab. 5 the mean values of the slope are listed for $\dot{a}_{\mathrm{Gauss}}$ and $\tilde{\dot{a}}_{\mathrm{Gauss}}$ and are both on average $-1.67\,\mathrm{md}^{-1}$.
The smoothed slope of the semi-major axis $\tilde{\dot{a}}_{\mathrm{Gauss}}$ and the ratio over the mean is shown in Fig. 25. All $\tilde{\dot{a}}_{\mathrm{Gauss}}$ exhibit mainly 1 d periodic oscillations of low amplitude. No positive values are reached even if the errors are taken into account, which have to be scaled for visibility. Additional small drops on 2018-09-05, 2018-10-02, 2018-10-10 and 2018-10-13 can be observed. This means, that with the Gaussian approach, the impact of geomagnetic activity of down to $ap = 30$ on orbital decay can be observed. The *ap* index occasionally reaches values $ap > 40$ even though there are no prior CMEs arriving at Earth. The reason for the increased geomagnetic activity during the previously mentioned dates is not clear yet. $\tilde{\dot{a}}_{\mathrm{PCA}}$ exhibits occasional spikes. $\tilde{\dot{a}}_{\mathrm{ACC}}$ and $\tilde{\dot{a}}_{\mathrm{ACC,shifted}}$ overlap, because the impact on the semi-major axis is mainly driven by the S-component which has almost the same offset in both the ACC data and the shifted ACC data. Because the R-component of the ACC data has a larger magnitude than the one of the PCA data or the shifted ACC data (see top left of Fig. 11) the error $\tilde{\sigma}_{\mathrm{ACC}}$ is the largest of all three and is about two times as large as the error $\tilde{\sigma}_{\mathrm{PCA}}$. At the beginning the error $\tilde{\sigma}_{\mathrm{ACC,shifted}}$ is half as large as $\tilde{\sigma}_{\mathrm{PCA}}$ but increases steadily until it is slightly larger than $\tilde{\sigma}_{\mathrm{PCA}}$ at the end. This phenomenon has yet to be investigated.
On 2018-08-26 the slope is about 4.5 times larger than on average for each data set. Apart from the geomagnetic storm on 2018-08-26, values of $ap > 40$ are often correlated with $\tilde{\dot{a}}_{\mathrm{Gauss}}$ reaching values that are 1.5 to 2.5 times larger than the average value. During the geomagnetic storm starting on 2018-08-26 the largest orbital decays are $\tilde{\dot{a}}_{\mathrm{PCA}} = -7.35\,\mathrm{md}^{-1}$, $\tilde{\dot{a}}_{\mathrm{ACC}} = -7.51\,\mathrm{md}^{-1}$ and $\tilde{\dot{a}}_{\mathrm{ACC,shifted}} = -7.51\,\mathrm{md}^{-1}$.

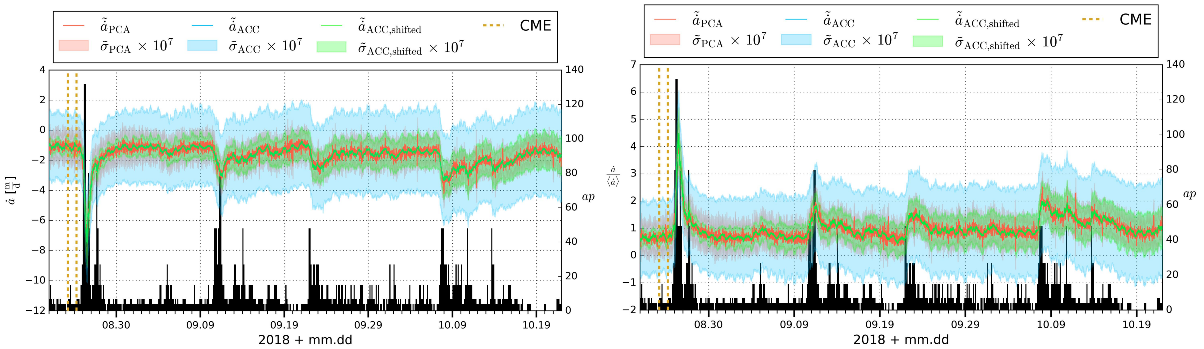

Figure 25: Smoothed slope of the semi-major axis of all three data sets for the Gaussian approach for GRACE-FO-1 in the year 2018. CME arrival times are indicated with vertical yellow dotted lines. Black bars show the *ap* index. After the arrival of two CMEs at the beginning of the interval the orbital decay visibly increases in accordance with elevated *ap* values.

The time interval considered for the modelled air density $\varrho$ and the $\beta$ angle is 2018-08-10 to 2018-10-22 and thus envelops both the time interval used for the fit model approach and the time interval used for the Gaussian approach. Figure 26 shows the modelled air density and the $\beta$ angle. Values for $\varrho$ range from about $0.15 \cdot 10^{-13}\,\mathrm{kgm}^{-3}$ to about $5.24 \cdot 10^{-13}\,\mathrm{kgm}^{-3}$. The $\beta$ angle starts at approximately 75° and decreases to about 10°. The modelled air density shows strong correlations with the *ap*, *Dst* and *AE* index (shown in previous figures).

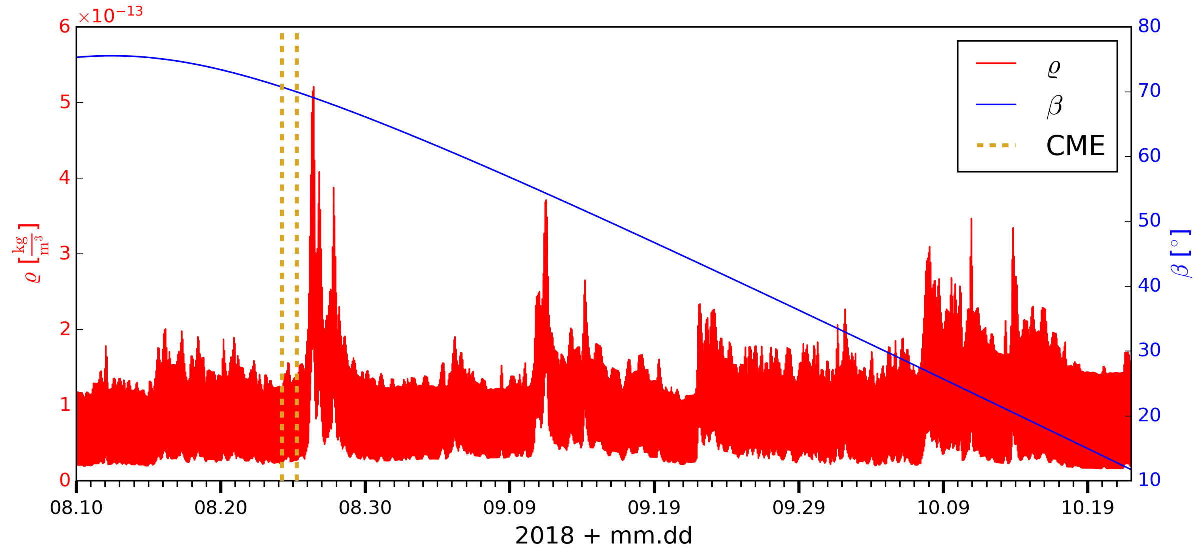

Figure 26: Time series of the modelled DTM2013 air density along the orbit and the $\beta$ angle. CME arrival times are indicated with vertical yellow dotted lines. Increased air density is visible on 2018-08-26 after the arrival of two CMEs.

## 5.2 Results for the Year 2023

For each satellite the time span from 2023-02-15 to 2023-04-06 (50 days) is analysed for both the fit model approach and the integration approach.

Figure 27 shows the time series of the *Dst* index. There is no time series of the *AE* index available for the considered time interval. The *Dst* index drops from about 15 nT on 2023-02-26 to about −130 nT on 2023-02-27. Similarly, after a CME arrives, the *Dst* index reaches a peak value of about −160 nT on 2023-03-24. Large drops in the *Dst* index are generally in accordance with a CME arrival.

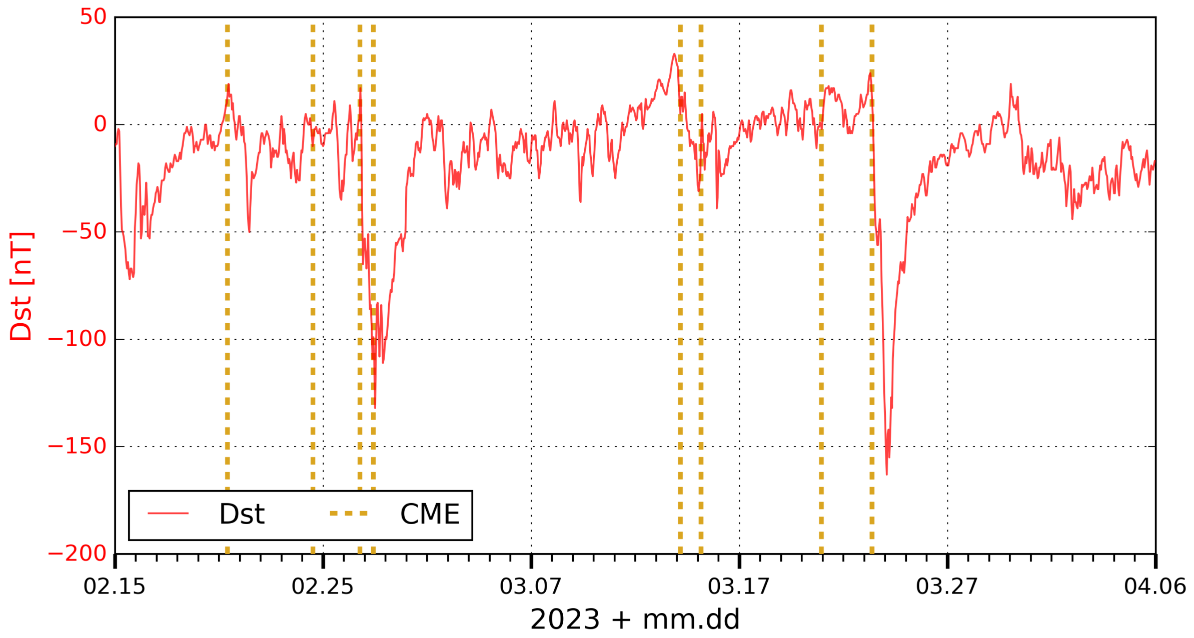

Figure 27: *Dst* index in 2023. CME arrival times are indicated with vertical yellow dotted lines. On both days 2023-02-27 and 2023-03-24 the *Dst* index reaches peak negative values after CMEs arrived.

### 5.2.1 GRACE-FO-1

Only one period $p_1 = 47.24\,\mathrm{min}$ marked in Fig. 28 is modelled for the analysis of the data in 2023. The errors of the LSAs are given in the second column of Tab. 6 and range from 63.33 m to 63.52 m. In the third column of Tab. 6 the mean orbital slope is given for each choice of $\psi$, ranging from $-33.30\,\mathrm{md}^{-1}$ to $-33.32\,\mathrm{md}^{-1}$.

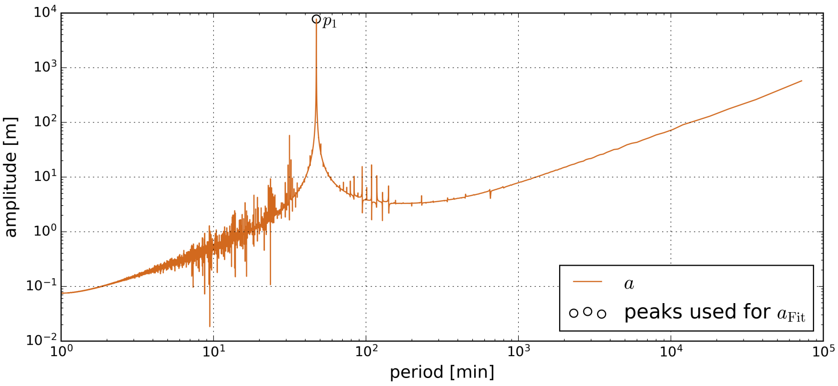

Figure 28: Spectrum of the semi-major axis of GRACE-FO-1 in the year 2023. The marked peak at 47.24 min is caused by the $C_{2,0}$ perturbation and is modelled in the LSA.

Table 6: Errors of the LSAs of the fit model and mean slope of the semi-major axis with different constraining factors $\psi$ for GRACE-FO-1 in the year 2023.

| $\psi$ | $m_0$ [m] | $\langle\dot{a}\rangle$ $[\frac{\mathrm{m}}{\mathrm{d}}]$ |
|---|---|---|
| $\psi_1$ | 63.33 | -33.32 |
| $\psi_2$ | 63.49 | -33.32 |
| $\psi_3$ | 63.52 | -33.30 |

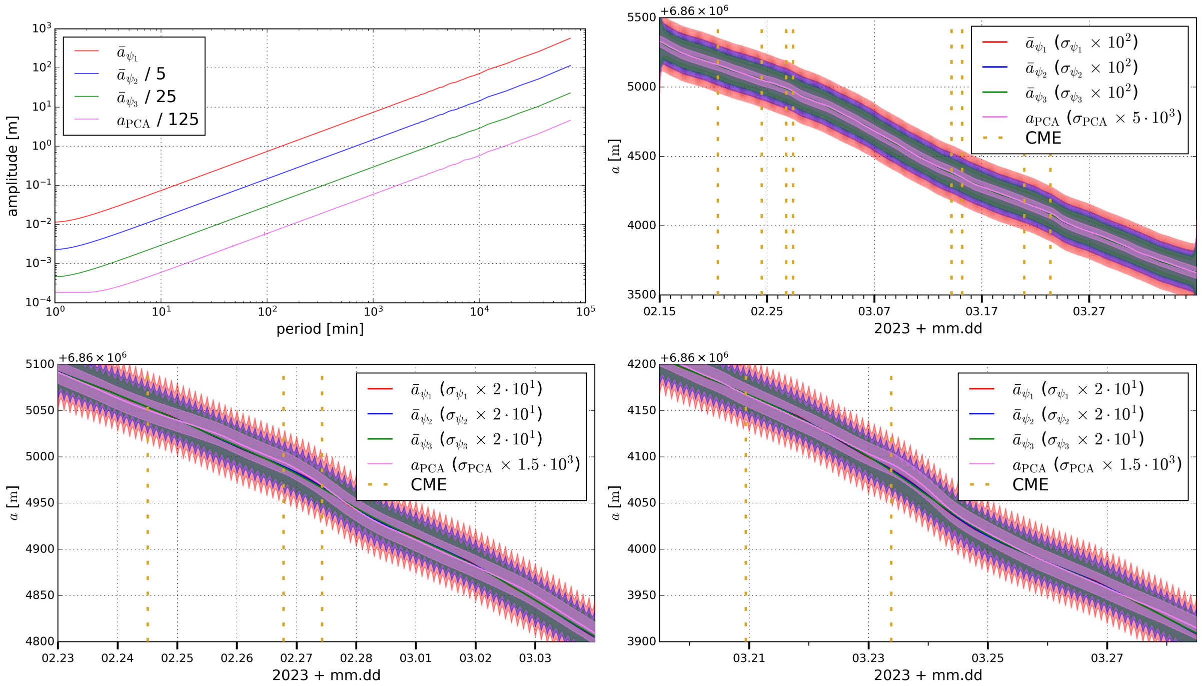

Figure 29: The spectra of the different $\bar{a}_{\mathrm{Fit}}$ and the spectrum of $a_{\mathrm{Gauss}}$ are shown in the upper left panel. In the upper right panel the time series of $\bar{a}_{\mathrm{Fit}}$ and $a_{\mathrm{Gauss}}$ along with scaled errors are shown. In the bottom row cut-outs centered around the geomagnetic storm on 2023-02-27 (left) and on 2023-03-24 (right) are shown. CME arrival times are shown as vertical yellow dotted lines.

The spectra of each $\bar{a}_{\mathrm{Fit}}$ and the spectrum of $a_{\mathrm{PCA}}$ is shown in Fig. 29 (top, left). The spectra appear smooth, but in the spectrum of $a_{\mathrm{PCA}}$ two periods between 43 min and 100 min are sticking out with small amplitude.
The time series of $\bar{a}_{\mathrm{Fit}}$ and $a_{\mathrm{PCA}}$ are shown in Fig. 29 (top, right). The curves from the fit model approach overlap with each other and differ from $a_{\mathrm{PCA}}$ only little. The errors have to be scaled for visibility. The error of $\bar{a}_{\mathrm{Fit}}$ is smaller with larger $\psi$. The error of $a_{\mathrm{PCA}}$ is the smallest. Soft kinks can be observed on 2023-02-27 and on 2023-03-23. The results suggest that the mean semi-major axis of GRACE-FO-1 decreased by about 1.7 km during the observed time interval.
In Fig. 29 (bottom row) zoom views centred around the two aforementioned kinks are shown. It is now visible that the curves of the fit model approach do not always overlap. The two kinks are better visible in the curve of the Gaussian approach.

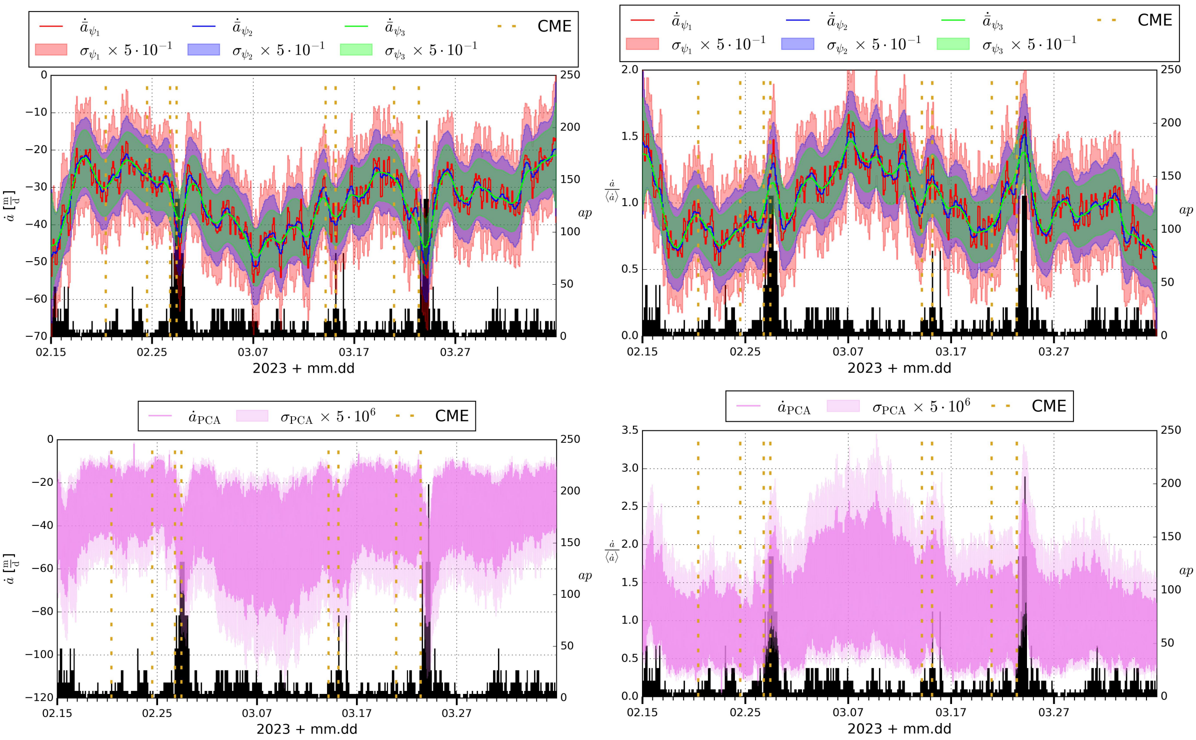

Figure 30: Resulting slope of the semi-major axis (left) and its ratio to the mean slope (right) for the fit model approach is shown in the top row. The same is shown for the Gaussian approach in the bottom row. CME arrival times are indicated with vertical yellow dotted lines. Black bars show the *ap* index.

In Fig. 30 (top row) the slope of the semi-major axis and its ratio to the mean is shown for the fit model approach, and the same is shown for the integration approach (bottom row). During the observed time interval the values of the slope of the semi-major axis range from $-15\,\mathrm{md}^{-1}$ to $-55\,\mathrm{md}^{-1}$ for the fit model approaches (errors not included) and they range from about $-10\,\mathrm{md}^{-1}$ to $-90\,\mathrm{md}^{-1}$ (the spike on 2023-02-22 not included) for the Gaussian approach. By including errors, $\dot{\bar{a}}_{\psi_1}$ is the only result, where positive values are reached occasionally. $\dot{\bar{a}}_{\psi_1}$ shows oscillations that are suppressed for higher $\psi$. Distinctive increases in orbital decay are visible on the dates mentioned before for all methods, which is in accordance with large *ap* values on these dates. The intensity of the drop in the slope of the semi-major axis on these dates decreases with stronger constraining. During the geomagnetic storm starting on 2023-02-26 the largest orbital decays reached are $\dot{\bar{a}}_{\psi_1} = -49.18\,\mathrm{md}^{-1}$, $\dot{\bar{a}}_{\psi_2} = -43.34\,\mathrm{md}^{-1}$ and $\dot{\bar{a}}_{\psi_3} = -38.38\,\mathrm{md}^{-1}$. During the geomagnetic storm starting on 2023-02-23 the largest orbital decays reached are $\dot{\bar{a}}_{\psi_1} = -54.22\,\mathrm{md}^{-1}$, $\dot{\bar{a}}_{\psi_2} = -50.48\,\mathrm{md}^{-1}$ and $\dot{\bar{a}}_{\psi_3} = -46.04\,\mathrm{md}^{-1}$. From 2023-03-02 to 2023-03-16 a larger orbital decay is visible for all methods without exceptionally large *ap* values. For the fit model approaches, the largest orbital decay is reached during the time interval on 2023-03-07. The same holds true for the Gaussian approach but the peak value is reached two days later. The reason for this is not yet clear. The mean orbital decay is $-33.38\,\mathrm{md}^{-1}$ for the Gaussian approach. On the dates 2023-02-27, 2023-03-07 and 2023-03-23 the orbital decay evaluated with $\dot{\bar{a}}_{\psi_1}$ is about 1.5 times larger than on average. $\dot{a}_{\mathrm{PCA}}$ is on 2023-02-27 2.25 times, on 2023-03-23 about 2.5 times and on 2023-03-09 about 2.75 times larger than on average. For the Gaussian approach, increased orbital decay is also in accordance with medium *ap* values.

The spectrum of the semi-major axis of GRACE-FO-1 in the year 2018 generally looks different compared to the one in 2023. This is due to GRACE-FO-1 being in a lower orbit in 2023, which means that there is more air drag and thus a stronger orbital decay. The spectrum of the semi-major axis of GRACE-FO-1 starts to increase in amplitude at 3 d in the year 2018 and it already starts to increase at 0.2 d in the year 2023. Thus, the spectrum in the year 2023 is already higher in amplitude at long periods possibly rendering $p_2$ not visible in the spectrum. Variations with periodicity of $p_2$ are also not visible in the trend functions $\bar{a}_{\mathrm{Fit}}$ in 2023, which may be because its amplitude is relatively low compared to the average orbital decay in this year.

The mean values of the smoothed and the "unsmoothed" slope are identical. Figure 31 shows the time series of $\tilde{\dot{a}}_{\mathrm{PCA}}$ and the ratio to its mean value. The mean value is with $\langle\tilde{\dot{a}}\rangle = -33.38\,\mathrm{md}^{-1}$ the same as for the "unsmoothed" version. In the considered time interval the values for the slope of the semi-major axis range from about $-20\,\mathrm{md}^{-1}$ to about $-61.90\,\mathrm{md}^{-1}$, the latter value reached during the geomagnetic storm starting on 2023-03-23. During the geomagnetic storm starting on 2023-02-26 the largest orbital decay is $\tilde{\dot{a}}_{\mathrm{PCA}} = -51.46\,\mathrm{md}^{-1}$. $\tilde{\dot{a}}_{\mathrm{PCA}}$ is on 2023-02-27 1.5 times, on 2023-03-23 about 1.9 times and on 2023-03-09 about 1.5 times larger than on average.
The orbital decay during quiet times is about $-25\,\mathrm{md}^{-1}$. This implies that the orbital decay during the geomagnetic storm on 2023-02-27 is 2.0 times larger and during the storm on 2023-03-24 2.5 times larger than during quiet times.

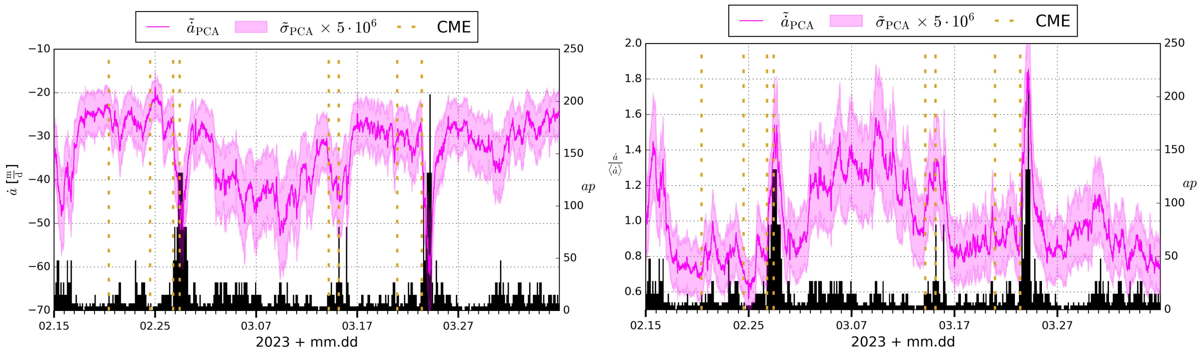

Figure 31: Slope of the semi-major axis obtained with the Gaussian approach after smoothing is applied. The smoothed slope of the semi-major axis is shown on the left. The ratio of the smoothed slope to the mean smoothed slope is shown on the right. CME arrival times are indicated with vertical yellow dotted lines. Black bars show the *ap* index.

In Fig. 32 the time series of the modelled air density and the $\beta$ angle are shown. The value of $\beta$ starts at 35° and decreases to −15° during the time interval. Values of $\varrho$ range from about $0.5 \cdot 10^{-12}\,\mathrm{kgm}^{-3}$ to about $5.5 \cdot 10^{-12}\,\mathrm{kgm}^{-3}$. Larger air density is observed on 2023-02-27 and on 2023-03-23. Additionally, from 2023-03-02 to 2023-03-14 a prolonged increase in air density is observable. This is remarkable because there is no increased geomagnetic activity taking place during this time interval. The modelled air density does not always correlate with the *ap* and the *Dst* index. Orbital decay from 2023-02-17 to 2023-02-19 correlates more with the *ap* index than with the modelled air density (there is low orbital decay and low *ap* values but increased modelled air density). After the geomagnetic storm on 2023-03-23 the orbital decay decreases, which is in accordance with a decrease in the *ap* index and a decrease in modelled air density. On 2023-03-30 the orbital decay increases again which is also in accordance with an increase in the *ap* index. However, the modelled air density decreases further.

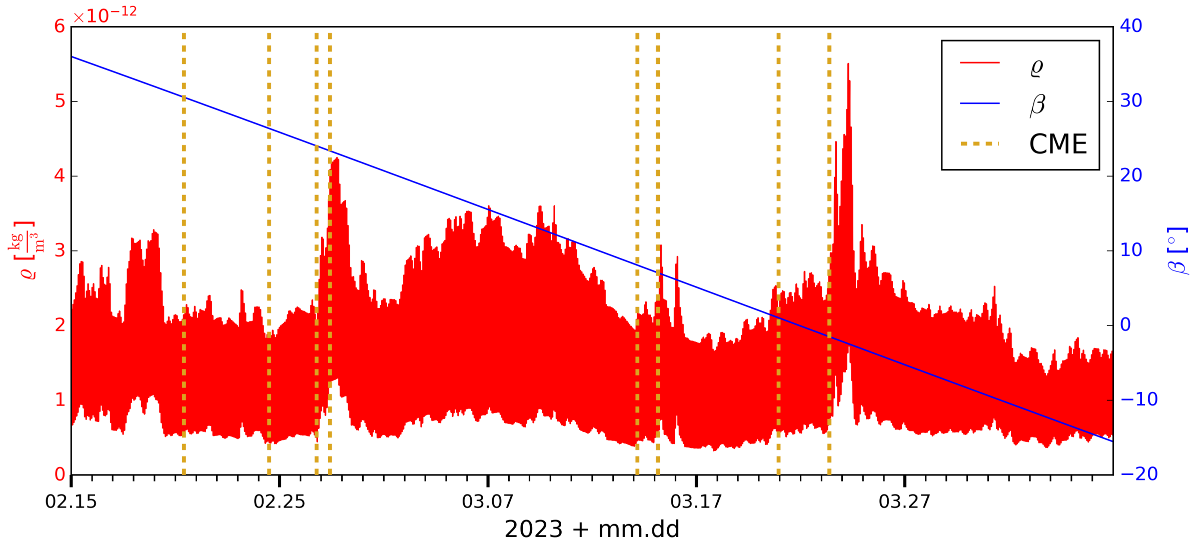

Figure 32: Time series of the modelled DTM2013 air density along the orbit and the $\beta$ angle. CME arrival times are shown as vertical yellow dotted lines.

### 5.2.2 Swarm-A

Only the period $p_1 = 46.93\,\text{min}$ marked in Fig. 33 is modelled subsequently to analyse the data from the Swarm-A satellite. The errors of the LSAs are given in the second column of Tab. 7 and range from 46.53 m to 46.94 m. For the fit model approach the mean values of the orbital decay range from $-61.54\,\text{md}^{-1}$ to $-61.57\,\text{md}^{-1}$ and are given in the third column of Tab. 7.

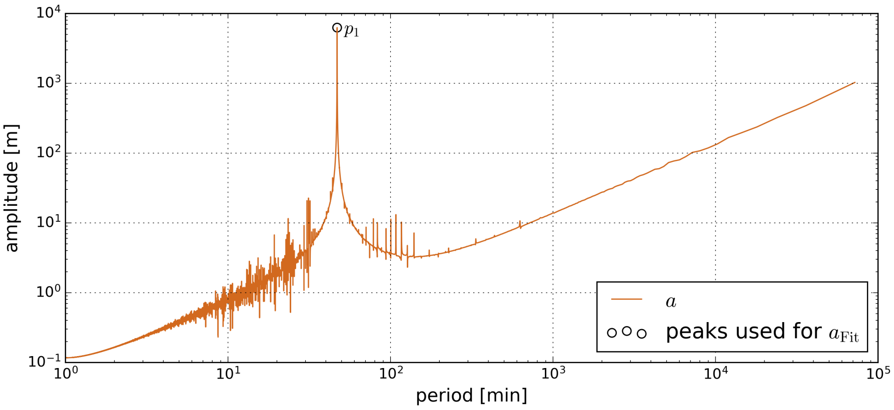

Figure 33: Spectrum of the semi-major axis of Swarm-A in the year 2023. The modelled period of 46.93 min is marked with a black circle. The period is induced by the $C_{2,0}$ perturbation.

Table 7: Errors of the LSAs of the fit model and mean slope of the semi-major axis with different constraining factors $\psi$ for Swarm-A in the year 2023.

| $\psi$ | $m_0$ [m] | $\langle\dot{a}\rangle$ $[\frac{\text{m}}{\text{d}}]$ |
|---|---|---|
| $\psi_1$ | 46.528 | -61.541 |
| $\psi_2$ | 46.856 | -61.553 |
| $\psi_3$ | 46.938 | -61.570 |

The spectra of each $\bar{a}_{\text{Fit}}$ and the spectrum of $a_{\text{PCA}}$ is shown in Fig. 34 (top, left). All spectra appear smooth at the scale used for the plot.
The time series of $\bar{a}_{\text{Fit}}$ and $a_{\text{PCA}}$ are shown in Fig. 34 (top, right). All curves are in accord with each

other and the errors have to be scaled for visibility. The error of $\bar{a}_{\text{Fit}}$ is smaller with larger $\psi$. The error of $a_{\text{PCA}}$ is the smallest. Slight kinks are observed on 2023-02-27 and on 2023-03-23. The results suggest that the mean semi-major axis of Swarm-A decreased approximately 3 km during the observed time interval.

In Fig. 34 (bottom row) zooms of the two kinks are shown. At this zoom level it can be seen that the curves do not perfectly overlap anymore.

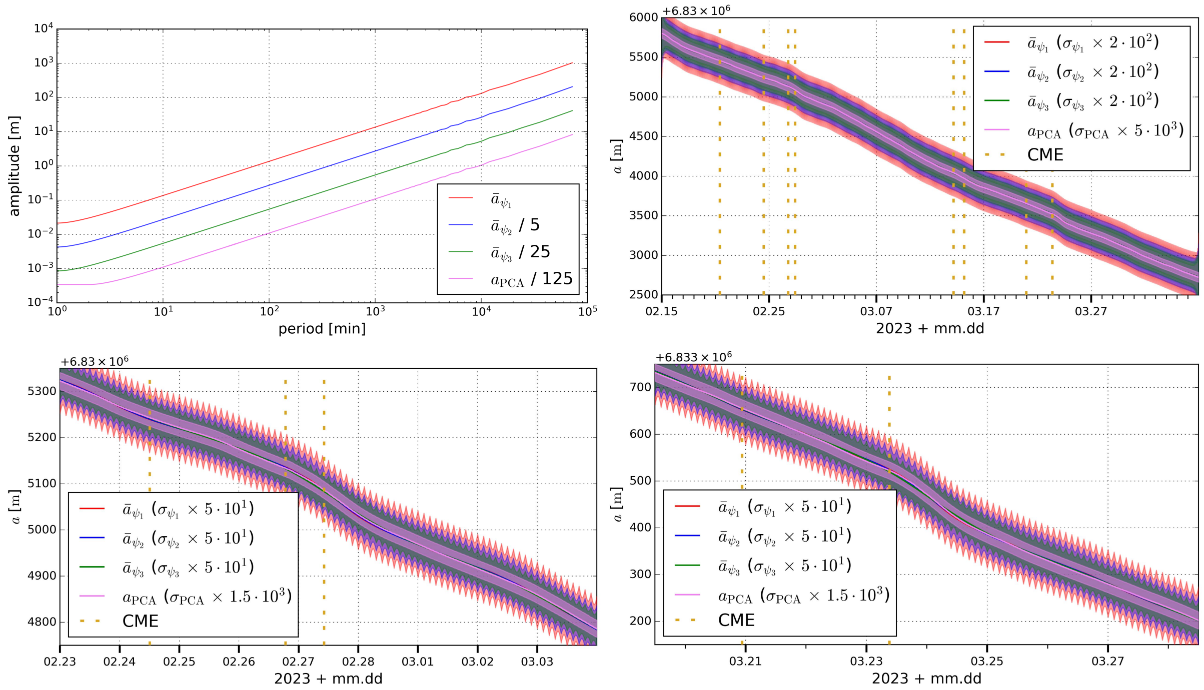

Figure 34: The spectra of the different $\bar{a}_{\text{Fit}}$ and the spectrum of $a_{\text{Gauss}}$ are shown in the upper left panel. In the upper right panel the time series of $\bar{a}_{\text{Fit}}$ and $a_{\text{Gauss}}$ along with scaled errors are shown. In the bottom row cut-outs centred around the geomagnetic storm on 2023-02-27 (left) and on 2023-03-24 (right) are shown. CME arrival times are marked with vertical yellow dotted lines.

In Fig. 35 (top row) the slope of the semi-major axis and its ratio to the mean is shown for the fit model approach, and the same is shown for the integration approach (bottom row). During the observed time interval the values for the slope of the semi-major axis range from $-15\,\text{md}^{-1}$ to about $-130\,\text{md}^{-1}$ for the fit model approaches (errors included) and they range from about $-10\,\text{md}^{-1}$ to about $-160\,\text{md}^{-1}$ for the Gaussian approach. $\dot{\bar{a}}_{\psi_1}$ shows oscillations that are suppressed for higher $\psi$. Distinctive increases in orbital decay are visible on the dates mentioned before for all methods, which is in accordance with high *ap* values on these dates. The intensity of the drop in the slope of the semi-major axis on these dates decreases with stronger constraining. During the geomagnetic storm starting on 2023-02-26 the largest orbital decays are $\dot{\bar{a}}_{\psi_1} = -101.36\,\text{md}^{-1}$, $\dot{\bar{a}}_{\psi_2} = -96.87\,\text{md}^{-1}$ and $\dot{\bar{a}}_{\psi_3} = -86.10\,\text{md}^{-1}$. During the geomagnetic storm starting on 2023-03-23 the largest orbital decays are $\dot{\bar{a}}_{\psi_1} = -108.74\,\text{md}^{-1}$, $\dot{\bar{a}}_{\psi_2} = -101.39\,\text{md}^{-1}$ and $\dot{\bar{a}}_{\psi_3} = -89.13\,\text{md}^{-1}$. Like it was the case for GRACE-FO-1, from 2023-03-02 to 2023-03-16 a larger orbital decay is visible for all methods without extraordinary large *ap* values. For the fit model approaches, the largest orbital decay is reached on 2023-03-23. The same holds true for the Gaussian approach. The mean orbital decay is $-61.61\,\text{md}^{-1}$ for the Gaussian approach. The orbital decay evaluated with $\dot{\bar{a}}_{\psi_1}$ is on 2023-02-27 and on 2023-03-09 about 1.6 times and on 2023-03-23 about 1.8 times larger than on average. $\dot{a}_{\text{PCA}}$ is on 2023-02-27 and on 2023-03-09 about 2.2 times and on 2023-03-23 about 2.5 times larger than on average. For the Gaussian approach, increased orbital decay is also in accordance with medium *ap* values.

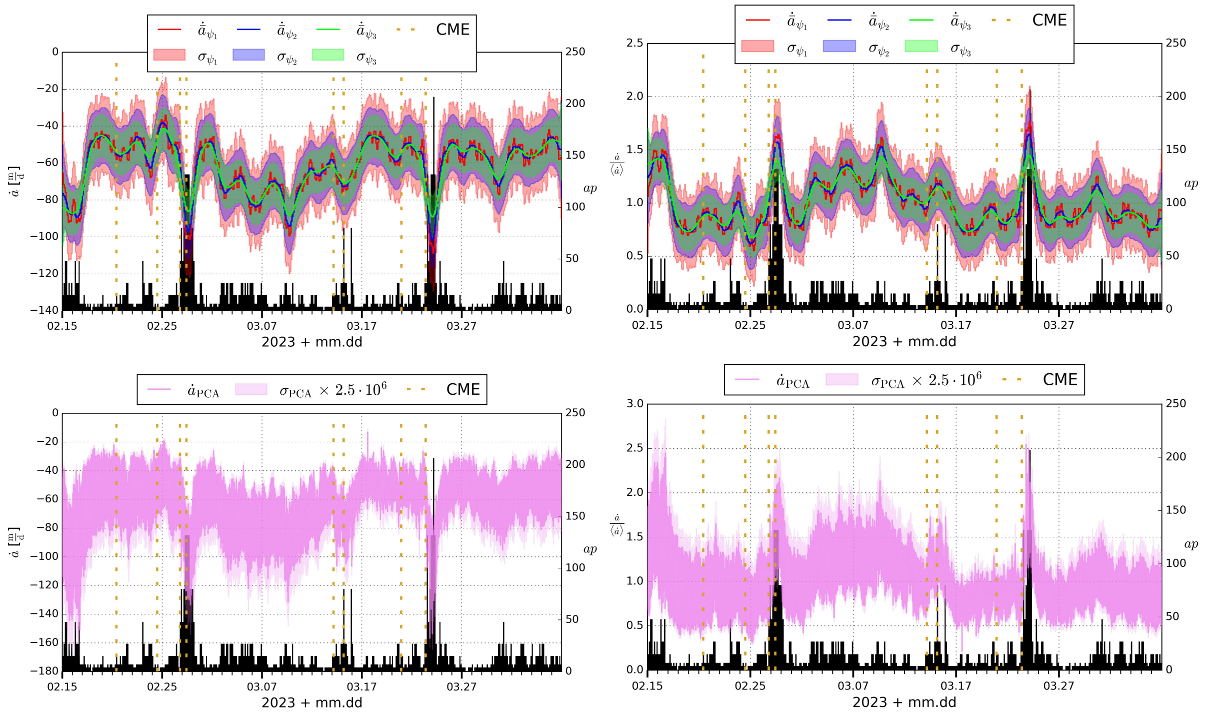

Figure 35: Resulting slope of the semi-major axis (left) and its ratio to the mean slope (right) for the fit model approach is shown in the top row. The same is shown for the Gaussian approach in the bottom row. CME arrival times are indicated with vertical yellow dotted lines. Black bars show the *ap* index.

Figure 36 shows the time series of $\tilde{\dot a}_{\mathrm{PCA}}$ and the ratio to its mean value. The mean value of the smoothed slope is $\langle \tilde{\dot a} \rangle = -66.62\,\mathrm{md}^{-1}$. In the considered time interval the values for the slope of the semi-major axis range from about $-40\,\mathrm{md}^{-1}$ to about $-110\,\mathrm{md}^{-1}$. During the geomagnetic storm starting on 2023-02-26 the largest orbital decay is $\tilde{\dot a}_{\mathrm{PCA}} = -98.59\,\mathrm{md}^{-1}$ and during the geomagnetic storm starting on 2023-03-23 the largest orbital decay is $\tilde{\dot a}_{\mathrm{PCA}} = -111.68\,\mathrm{md}^{-1}$. $\tilde{\dot a}_{\mathrm{PCA}}$ is on 2023-02-27 and on 2023-03-09 about 1.5 times and on 2023-03-23 about 1.7 times larger than on average.
If the quiet times are taken as epochs when the orbital decay is the smallest, the orbital decay is $-40\,\mathrm{md}^{-1}$ during low geomagnetic activity. This means that during the geomagnetic storm on 2023-02-27 the orbital decay is larger by factor of 2.5 and one day after the arrival of the CME on 2023-03-23 the orbital decay is larger by a factor of 2.8 when compared to orbital decay during quiet times.

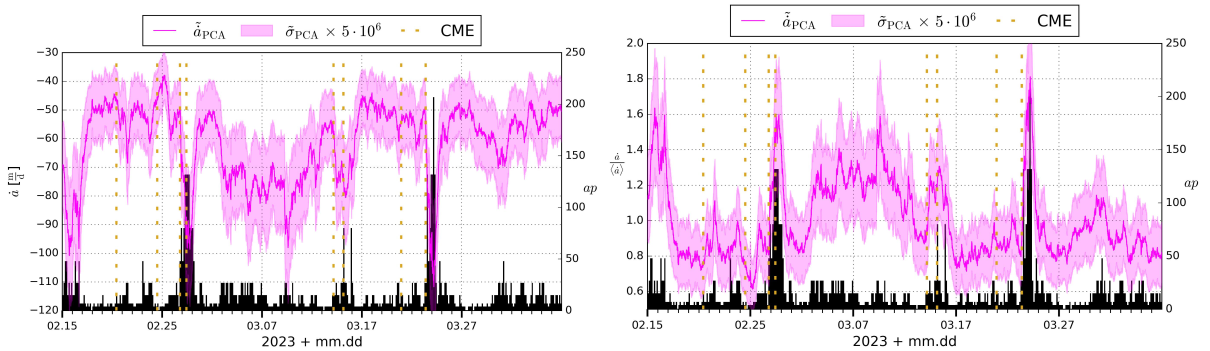

Figure 36: Slope of the semi-major axis obtained with the Gaussian approach after smoothing is applied. The smoothed slope of the semi-major axis is shown on the left. The ratio of the smoothed slope to the mean smoothed slope is shown on the right. CME arrival times are indicated with vertical yellow dotted lines. Black bars show the *ap* index.

In Fig. 37 the time series of the modelled air density and the $\beta$ angle are shown. The value of $\beta$ starts at 10° and increases to 75° during the time interval. Values of $\varrho$ range from $0.75 \cdot 10^{-12}\,\mathrm{kgm}^{-3}$ to about

$4.75 \cdot 10^{-12}\,\mathrm{kgm}^{-3}$. The behaviour of the modelled air density is similar to the one found in the case of GRACE-FO-1.

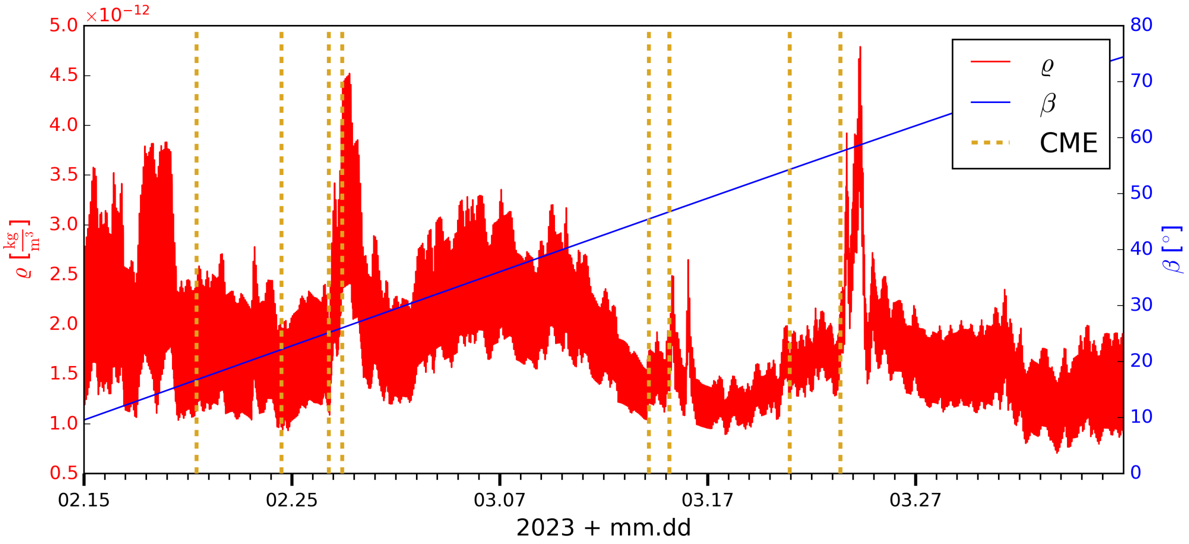

Figure 37: Time series of the modelled DTM2013 air density along the orbit and the $\beta$ angle. CME arrival times are indicated with vertical yellow dotted lines. On 2023-02-27 and 2023-03-24 the air density reaches peak values after CME arrivals.

### 5.2.3 Sentinel-1A

There is one prominent period $p_1 = 49.38\,\mathrm{min}$ marked in Fig. 38 (left) which is modelled with the fit model. As opposed to the satellite data analysed in the previous sections, there are some unusually high peaks between $3,000\,\mathrm{min}$ ($\approx 2\,\mathrm{d}$) and $13,000\,\mathrm{min}$ ($\approx 9\,\mathrm{d}$) visible in the Sentinel-1A data. These peaks are mostly related to the fact that regular MANs are executed to keep the orbit of Sentinel-1A according to the mission specifications. The starting epochs of the MANs are marked with brown dotted lines. The errors of the LSAs are given in the second column of Tab. 8 and range from 41.89 m to 42.42 m. In the third column of Tab. 8 the mean slopes are listed and range from $0.18\,\mathrm{md}^{-1}$ to $0.34\,\mathrm{md}^{-1}$. The mean orbital decay is $0.82\,\mathrm{md}^{-1}$ for the Gaussian approach.
The spectra of each $\bar{a}_{\mathrm{Fit}}$ and the spectrum of $a_{\mathrm{PCA}}$ are shown in the left panel of Fig. 38 (right). Each $\bar{a}_{\mathrm{Fit}}$ spectrum has a certain structure centred around 144 min which repeats itself in the form of overtones for smaller periods. This structure and its overtones is damped with higher $\psi$. $\bar{a}_{\mathrm{Fit}}$ is spiky above 432 min with $\psi_1$, spiky above 576 min with $\psi_2$ and spiky above 864 min with $\psi_3$. The spectrum of $a_{\mathrm{PCA}}$ is complicated and noisy. While the spectra for the different $\bar{a}_{\mathrm{Fit}}$ are similar to each other above 288 min, the spectrum of $a_{\mathrm{PCA}}$ is quite different in this range. Additionally, in contrast to the spectra of $\bar{a}_{\mathrm{Fit}}$, the spectrum of $a_{\mathrm{PCA}}$ contains two "bulges" centred around 5.76 min. These two bulges are visible in a smaller form as an overtone at 2.88 min. Another bulge is visible at approximately 2.16 min. The bulges are probably an artefact because the PCAs have a duration of 6 min and are resampled to 30 s. It should be noted, that the amplitudes of $a_{\mathrm{PCA}}$ are unusually large (the scaling factor skips a power) compared to the fit model approaches.

Table 8: Errors of the LSAs of the fit model and mean slope of the semi-major axis with different constraining factors $\psi$ for Sentinel-1A in the year 2023.

| $\psi$ | $m_0$ [m] | $\langle\dot{a}\rangle$ $[\frac{\mathrm{m}}{\mathrm{d}}]$ |
|---|---|---|
| $\psi_1$ | 41.89 | 0.34 |
| $\psi_2$ | 42.30 | 0.21 |
| $\psi_3$ | 42.42 | 0.18 |

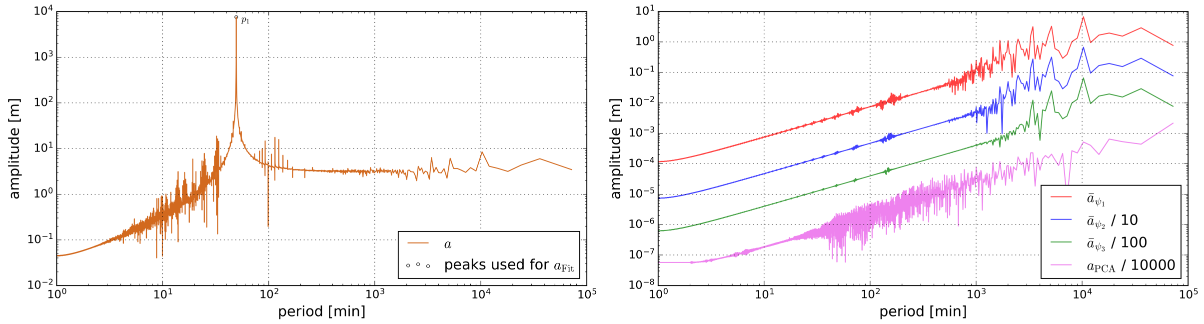

Figure 38: The spectrum of the semi-major axis is shown on the left. The marked period of 49.38 min, induced by the $C_{2,0}$ perturbation, is modelled in the LSA. On the right the spectra of the different $\bar{a}_{\mathrm{Fit}}$ and the spectrum of $a_{\mathrm{PCA}}$ are shown. The spectra are shifted for better visibility.

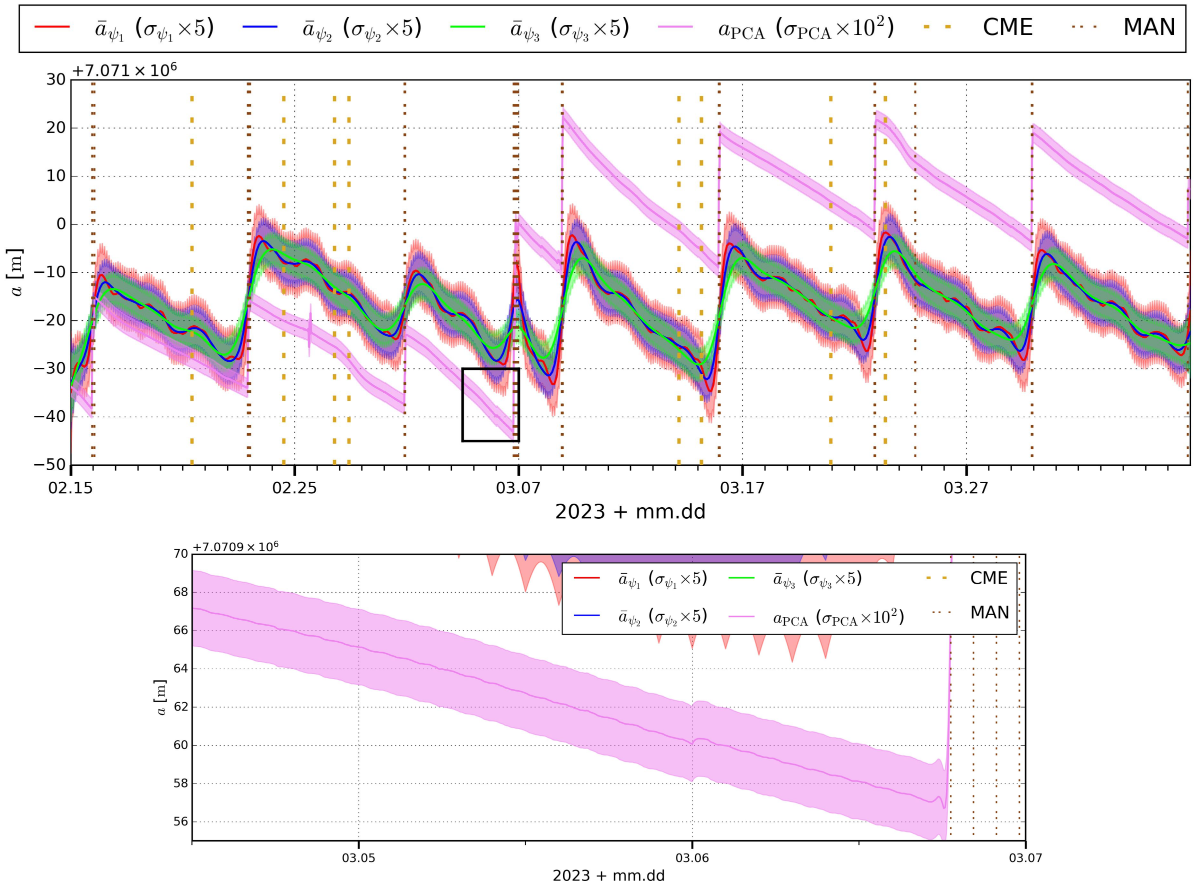

Figure 39: In the upper panel the trend functions $\bar{a}_{\mathrm{Fit}}$ of the fit model approach and the the numerically integrated semi-major axis $a_{\mathrm{PCA}}$ are shown. In the lower panel a zoom view is shown. The zoom view corresponds to the black rectangle frame visible in the upper plot. Vertical yellow dotted lines mark CME arrival times and black bars represent the *ap* index. Vertical brown dotted lines mark the start time of a MAN.

The time series of $\bar{a}_{\mathrm{Fit}}$ and $a_{\mathrm{PCA}}$ are shown in the top of Fig. 39. In the bottom of Fig. 39 a zoom view is shown. The borders of the zoom view are marked with a black rectangle frame in the top of Fig. 39. MANs take place (if a MAN line is thicker, there is more than one MAN) on 2023-02-16, 02-23, 03-02, 03-06, 03-08, 03-15, 03-22, 03-24, 03-29 and on 04-05. The curves of the fit model approach are somewhat in accord. Reactions on orbital increase due to MANs succeed with different response times based on the choice of $\psi$. All fit model curves exhibit oscillations between MANs but only in the case of $\psi_3$ these oscillations are sufficiently damped to prohibit temporarily increases in $\bar{a}_{\mathrm{Fit}}$ (except due to

MANs). The error of $\bar{a}_{\mathrm{Fit}}$ is smaller with larger $\psi$. The error of $a_{\mathrm{PCA}}$ is the smallest. In contrast to the fit model curves where MANs are not explicitly taken into account (e.g., by allowing for a jump in the mean semi-major axis), the reaction of $a_{\mathrm{PCA}}$ on a MAN is a sharp jump, so that the curve of the Gaussian approach is jagged similar to a sawtooth wave form. The curve of $a_{\mathrm{PCA}}$ is temporarily steeper around 2023-02-27 and around 2023-03-23. On 2023-02-25 there is an instance, when $a_{\mathrm{PCA}}$ is suddenly 3 m lower and also 4 m higher than before and after, even though there is no MAN at that time. Further analysis revealed that the POD of Sentinel-1A was exceptionally bad on that day as indicated by a significantly increased level of the fit of the GPS carrier phase data. It should be noted that the phase measurement RMS of daily POD performed with phase measurements is usually larger on days that contain a MAN (not shown). PCAs probably do not model MANs with sufficient quality.

With the exception of the MANs on 2023-02-16 and 2023-03-24, on the beginning of days of MANs there is a minor “dislocation” in $a_{\mathrm{PCA}}$ visible (the ones on 2023-03-02 and on 2023-04-04 are barely visible). A small dislocation is also visible shortly before the MAN on 2023-03-08. As the dislocations are barely visible, the case of the MANs on 2023-03-06 is shown as an example in the lower panel of Fig. 39.

Interestingly, the reaction of $a_{\mathrm{PCA}}$ onto a MAN deviates from the reactions of the fit model approaches. After the first MAN on 2023-02-15, $a_{\mathrm{PCA}}$ is about 5 m below $\bar{a}_{\psi_3}$ but after the MAN on the end of the day 2023-02-22, $a_{\mathrm{PCA}}$ is about 15 m below $\bar{a}_{\psi_3}$. Moreover, during the MAN at the end of the day 2023-03-06, $a_{\mathrm{PCA}}$ executes a significantly larger jump than the fit model approaches. After this MAN, $a_{\mathrm{PCA}}$ is alway about 25 m above $\bar{a}_{\psi_3}$. A reason for this strange behaviour could involve integration problems regarding the PCAs.

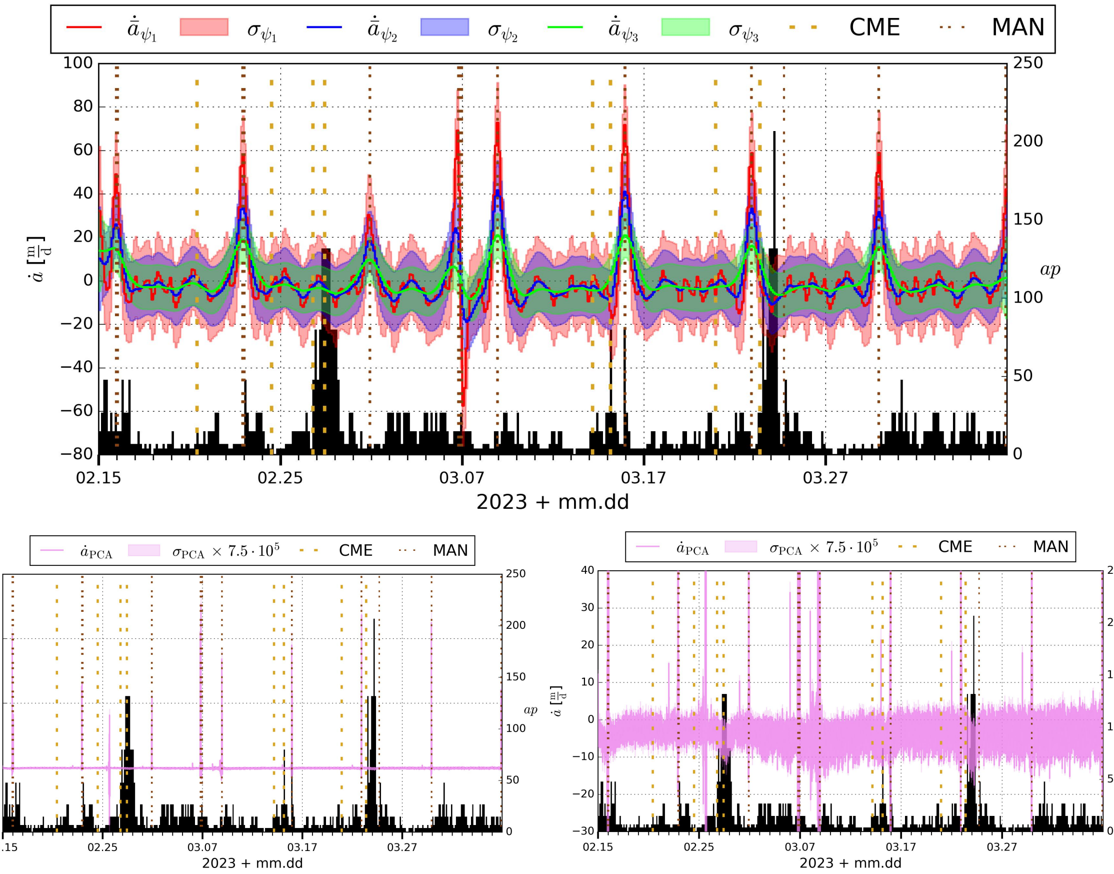

Figure 40: In the upper panel the slopes of the trend functions of the fit model are shown. In the lower left panel the slope of $a_{\mathrm{PCA}}$ is shown. In the lower right panel a vertical cut-out of the slope obtained with the Gaussian approach is shown. Vertical yellow dotted lines mark CME arrival times and black bars represent the *ap* index. Vertical brown dotted lines mark the start time of a MAN.

In Fig. 40 (top) the slope of the semi-major axis is shown for the fit model approaches, and the same is shown for the integration approach (bottom row). During the analysed time interval the values for the slope of the semi-major axis range from about 90 $\mathrm{m\,d^{-1}}$ to about $-75\,\mathrm{m\,d^{-1}}$ for the fit model approaches (errors not included) and range from about 1,250 $\mathrm{m\,d^{-1}}$ to about $-450\,\mathrm{m\,d^{-1}}$ for the Gaussian approach. During MANs peak values are reached. If MANs are excluded the values for the slope of the semi-major axis range from about 5 $\mathrm{m\,d^{-1}}$ to about $-15\,\mathrm{m\,d^{-1}}$ for the fit model approaches (errors not included) and the upper range for the Gaussian approach changes to about 400 $\mathrm{m\,d^{-1}}$. If the the date 2023-02-22 is also excluded the values range from about 35 $\mathrm{m\,d^{-1}}$ to about $-21\,\mathrm{m\,d^{-1}}$ for the Gaussian approach. The MAN on 2023-03-24 is the only one, where one day prior to it, no exceptionally large positive peak (the values range from 7.5 $\mathrm{m\,d^{-1}}$ to 35 $\mathrm{m\,d^{-1}}$) is observable in the integration approach. On the end of day 2023-03-07, which is one day prior to the MAN on 2023-03-08, there is also an exceptionally low value of $-21\,\mathrm{m\,d^{-1}}$ observable for $\dot{a}_{\mathrm{PCA}}$. The MAN on 2023-03-08 is also the only MAN where one day prior to it, there is also an exceptionally low value observable for the Gaussian approach. If now also all the peaks (positive and negative) one day prior to a MAN are excluded, the values for the slope of the semi-major axis range from about 5 $\mathrm{m\,d^{-1}}$ to about $-17.5\,\mathrm{m\,d^{-1}}$ for the Gaussian approach. Both the slopes with $\psi_1$ and $\psi_2$ occasionally reach positive values, but the slope with $\psi_3$ only reaches positive values when there is a MAN, due to the oscillations being sufficiently suppressed. A distinctive increase in orbital decay is visible during medium to high *ap* values for the Gaussian approach. Oscillations and MANs prohibit such a statement for the fit model approaches. Like for the other satellites, from 2023-03-02 to 2023-03-16 a prolonged larger orbital decay is visible for the integration method without extraordinary large *ap* values.

Figure 41 shows the time series of $\tilde{\dot{a}}_{\mathrm{PCA}}$. The mean value is $\langle \tilde{\dot{a}} \rangle = 0.82\,\mathrm{m\,d^{-1}}$. In the analysed time interval the values for the smoothed slope of the semi-major axis range from about 450 $\mathrm{m\,d^{-1}}$ to about $-50\,\mathrm{m\,d^{-1}}$. If the MAN times are not included, the largest value of 100 $\mathrm{m\,d^{-1}}$ is reached on 2023-02-24, when also the largest negative value is reached. If this day is also excluded, the values for the smoothed slope of the semi-major axis range from about 1 $\mathrm{m\,d^{-1}}$ to $-8.78\,\mathrm{m\,d^{-1}}$, the latter value reached during the geomagnetic storm starting on 2023-03-23. During the geomagnetic storm starting on 2023-02-26 the largest orbital decay reached is $-6.81\,\mathrm{m\,d^{-1}}$. If the peaks taking place one day prior to a MAN are also excluded, the upper boundary changes to $-1\,\mathrm{m\,d^{-1}}$.

To be able to form meaningful statements about the ratio to the mean of the orbital slope, at least the times when MANs take place need to be excluded (possibly it should be considered to also take out all the peaks one day prior to a MAN). During times of low geomagnetic activity the orbital decay rate is about 3 $\mathrm{m\,d^{-1}}$. Therefore, the orbital decay rate during the first geomagnetic storms is higher by a factor of about 2.3 and in the case of the second geomagnetic storm the factor is about 2.9.

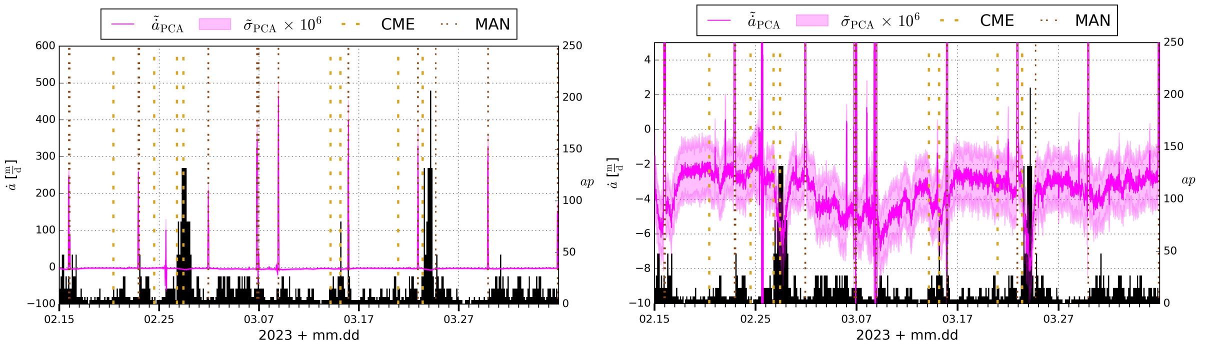

Figure 41: The smoothed slope obtained with the Integration approach is shown (left) along with a vertical zoom (right). Vertical yellow dotted lines mark CME arrival times and black bars represent the *ap* index. Vertical brown dotted lines mark the start time of a MAN.

In Fig. 42 the time series of the modelled air density and the $\beta$ angle are shown. The value of $\beta$ starts at about 84°, increases to about 87° on 2023-03-01 and then decreases to about 76°. The variation of the $\beta$ angle is not large because the orbit of Sentinel-1A is sun-synchronous. Values of $\varrho$ range from about $0.25 \cdot 10^{-13}\,\mathrm{kg\,m^{-3}}$ to about $4.25 \cdot 10^{-13}\,\mathrm{kg\,m^{-3}}$. The behaviour of the modelled air density is similar to the one of GRACE-FO-1 and Swarm-A.

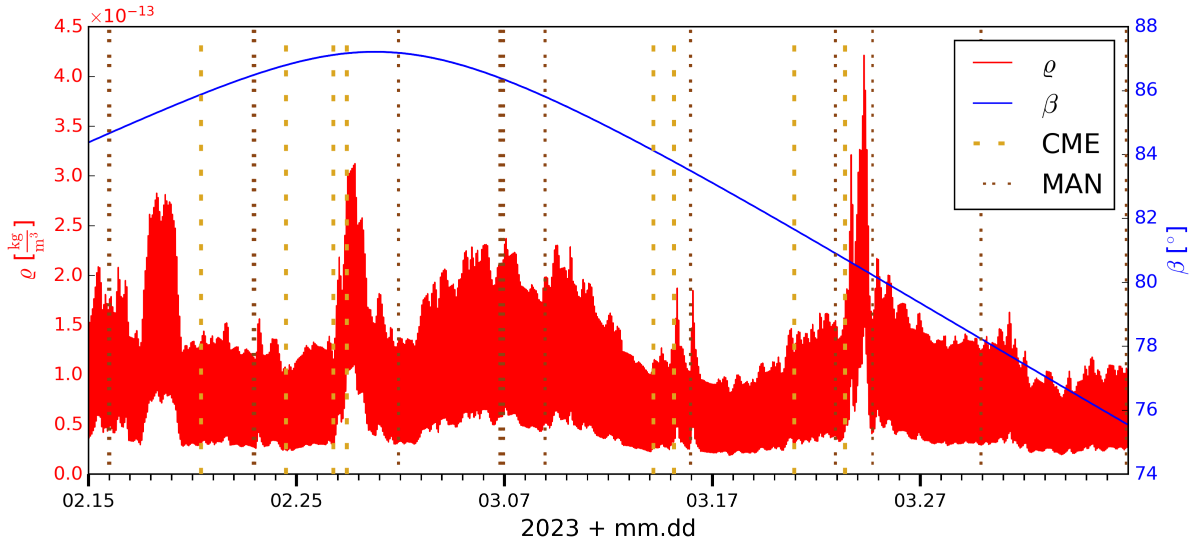

Figure 42: Time series of the modelled DTM2013 air density along the orbit and the $\beta$ angle. CME arrival times are shown as vertical yellow dotted lines. Vertical brown dotted lines mark the starting epochs of MANs.

## 5.3 Results for the Year 2024

The interval for both the fit model approach and the integration approach is chosen to be from 2024-05-01 to 2024-05-14 (14 days).

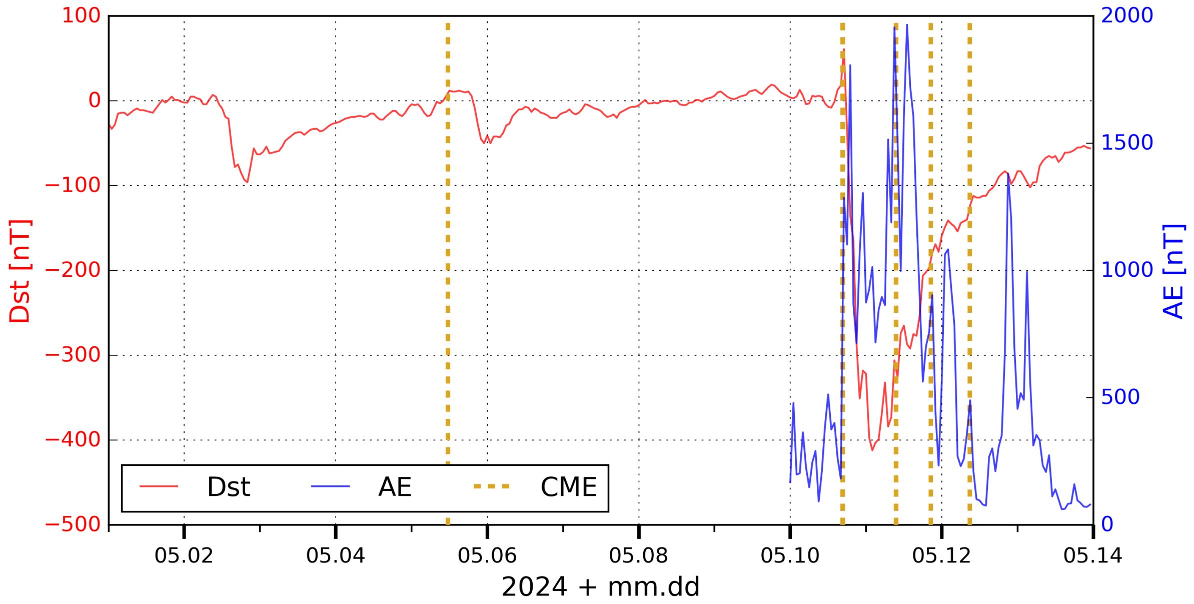

Figure 43: *Dst* and *AE* index in the 2024. CME arrival times are shown as vertical yellow dotted lines. There is no data for the *AE* index before 2024-05-10. On the days 2024-05-10 and 2024-05-11 both indices reach peak values after CME arrivals.

Figure 43 shows the time series of the *Dst* index and the *AE* index from 2024-05-01 to 2024-05-14. There is no *AE* index available before 2024-05-10. The *Dst* index drops from about 60 nT on 2024-05-10 to about −400 nT on the beginning of day 2024-05-11. Similarly, the *AE* index increases from about 200 nT on 2024-05-10 to about 1,800 nT on the same day and on 2024-05-11 it reaches a peak value of 2,000 nT. The *Dst* index reaches a value of −100 nT on 2024-05-02 without the arrival of a prior CME. It is possible that the CME on 2024-05-05 is responsible for the decrease in the *Dst* index to about

−50 nT one day later. Between 2024-05-10 and 2024-05-12 four CMEs arrive at Earth. It is during this time that both indices reach the extreme values mentioned above.

### 5.3.1 Swarm-A

Only one period $p_1 = 46.99\,\mathrm{min}$ marked in Fig. 44 (left), is modelled. The errors of the LSAs are given in the second column of Tab. 9 and range from 45.37 m to 47.36 m. For the fit model approach, the mean values of the orbital slope range from $-53.24\,\mathrm{md}^{-1}$ to $-53.30\,\mathrm{md}^{-1}$ and are given in the third column of Tab. 9. The mean orbital slope is $-53.37\,\mathrm{md}^{-1}$ for the Gaussian approach.
The spectra of each $\bar{a}_{\mathrm{Fit}}$ and the spectrum of $a_{\mathrm{PCA}}$ is shown in Fig. 44 (right). All spectra appear smooth but in the spectrum of $a_{\mathrm{PCA}}$ a small period between 90 min and 100 min is faintly sticking out.

Table 9: Errors of the LSAs of the fit model and mean slope of the semi-major axis with different constraining factors $\psi$ for Swarm-A in the year 2024.

| $\psi$ | $m_0$ [m] | $\langle\dot{a}\rangle$ $[\frac{\mathrm{m}}{\mathrm{d}}]$ |
|---|---|---|
| $\psi_1$ | 45.37 | -53.30 |
| $\psi_2$ | 45.83 | -53.26 |
| $\psi_3$ | 47.36 | -53.24 |

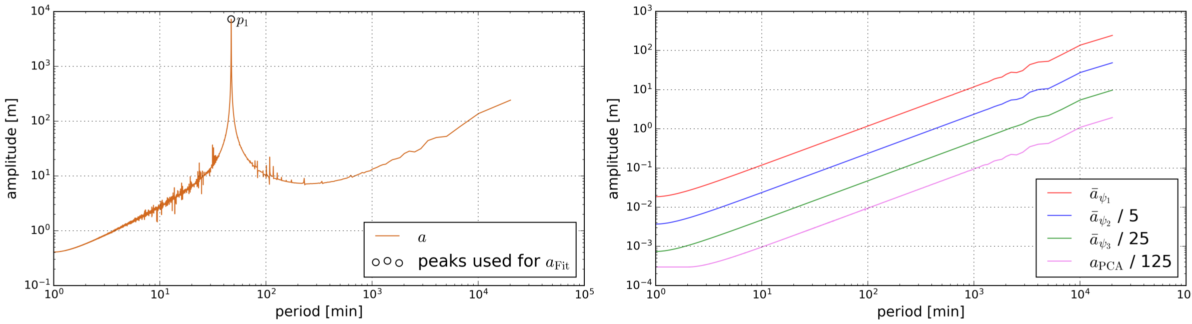

Figure 44: The spectrum of the semi-major axis is shown on the left. The marked period of 46.99 min is caused by the $C_{2,0}$ perturbation and is modelled in the LSA. On the right the spectra of the different $\bar{a}_{\mathrm{Fit}}$ and the spectrum of $a_{\mathrm{Gauss}}$ is shown. The spectra are shifted for better visibility.

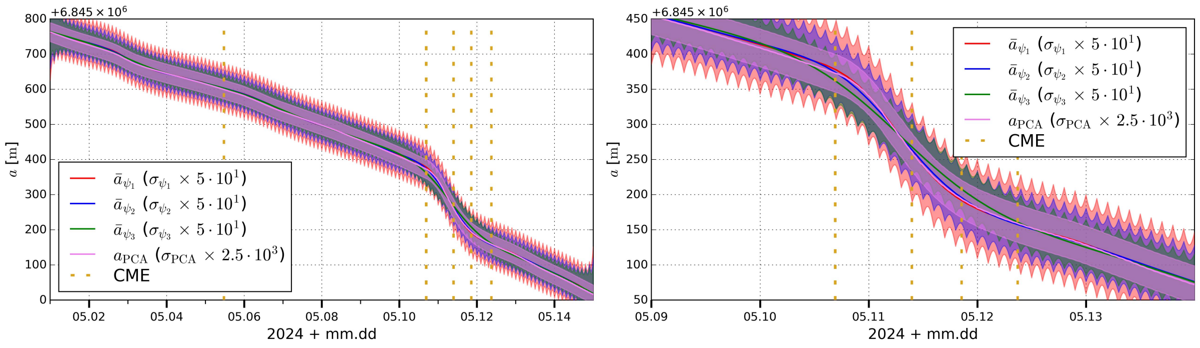

Figure 45: The semi-major axis obtained with the different approaches along with scaled errors is shown on the left. On the right a vertical zoom in is shown. CME arrival times are shown as vertical yellow dotted lines. After the arrival of the CME on 2024-05-10 the semi-major axis decreases more than usual.

The time series of $\bar{a}_{\mathrm{Fit}}$ and $a_{\mathrm{PCA}}$ are shown in Fig. 45. The curves are mostly in good agreement but during a stronger decrease between 2024-05-10 and 2024-05-12 the curves differ from each other more than usually observed in the previous sections for the other time intervals. Especially $\bar{a}_{\psi_3}$ differs from the other curves implying that the constraint are too tight for the more severe conditions. $\bar{a}_{\psi_1}$ and $\bar{a}_{\psi_2}$ almost overlap with $a_{\mathrm{PCA}}$ during the strong decrease on 2024-05-11 but they differ from $a_{\mathrm{PCA}}$ on

2024-05-10. The errors have to be scaled for visibility. The error of $\bar{a}_{\mathrm{Fit}}$ is smaller with larger $\psi$. The error of $a_{\mathrm{PCA}}$ is the smallest. The results suggest that the mean semi-major axis of Swarm-A decreased approximately 750 m during the observed time interval.

In Fig. 46 (top row) the slope of the semi-major axis and its ratio to the mean is shown for the fit model approach, and the same is shown for the integration approach (bottom row). During the analysed time interval the values for the slope of the semi-major axis range from $-25\,\mathrm{md}^{-1}$ to about $-214.81\,\mathrm{md}^{-1}$ for the fit model approaches (errors not included) and range from about $-10\,\mathrm{md}^{-1}$ to about $-290\,\mathrm{md}^{-1}$ for the Gaussian approach. During the geomagnetic storm starting on 2024-05-10 the largest orbital decays are $\dot{\bar{a}}_{\psi_1} = -214.81\,\mathrm{md}^{-1}$, $\dot{\bar{a}}_{\psi_2} = -185.48\,\mathrm{md}^{-1}$ and $\dot{\bar{a}}_{\psi_3} = -144.99\,\mathrm{md}^{-1}$. $\dot{\bar{a}}_{\psi_1}$ shows oscillations that are suppressed for higher $\psi$. Distinct increases in orbital decay are visible on 2024-05-02 and on 2024-05-11 for all methods, which is in accordance with high $ap$ values on these dates. For the Gaussian approach, increased orbital decay is also in accordance with medium $ap$ values. The increased orbital decay that takes place during 2024-05-10 to 2024-05-12 resembles a Gaussian distribution function especially for the fit model approach. A stronger constraining factor increases the width and decreases the depth of this drop in the slope. Regardless of the method the largest value of orbital decay is reached on 2024-05-11. However, $\dot{\bar{a}}_{\mathrm{Fit}}$ reaches the peak value a couple hours later than $\dot{a}_{\mathrm{Gauss}}$. This is because the length of the fitted subintervals is 2.4 h (fitting more subintervals per day and stronger constraining probably leads to better results). The orbital decay evaluated with $\dot{\bar{a}}_{\psi_1}$ is on 2024-05-11 about 4 times higher than on average. $\dot{a}_{\mathrm{PCA}}$ is on 2024-05-11 about 5.5 times larger than on average. The lowest orbital decay reached with the fit model is around $-30\,\mathrm{md}^{-1}$ on 2024-05-04.

On 2024-05-10 the values of the $ap$ index are $ap_7 = ap_8 = 400$ and on 2024-05-10 they are $ap_1 = ap_3 = ap_4 = ap_5 = 400$ ($ap_2 = 207$). It should be noted that 400 is the maximum value for the $ap$ index. This corresponds to an extreme geomagnetic storm.

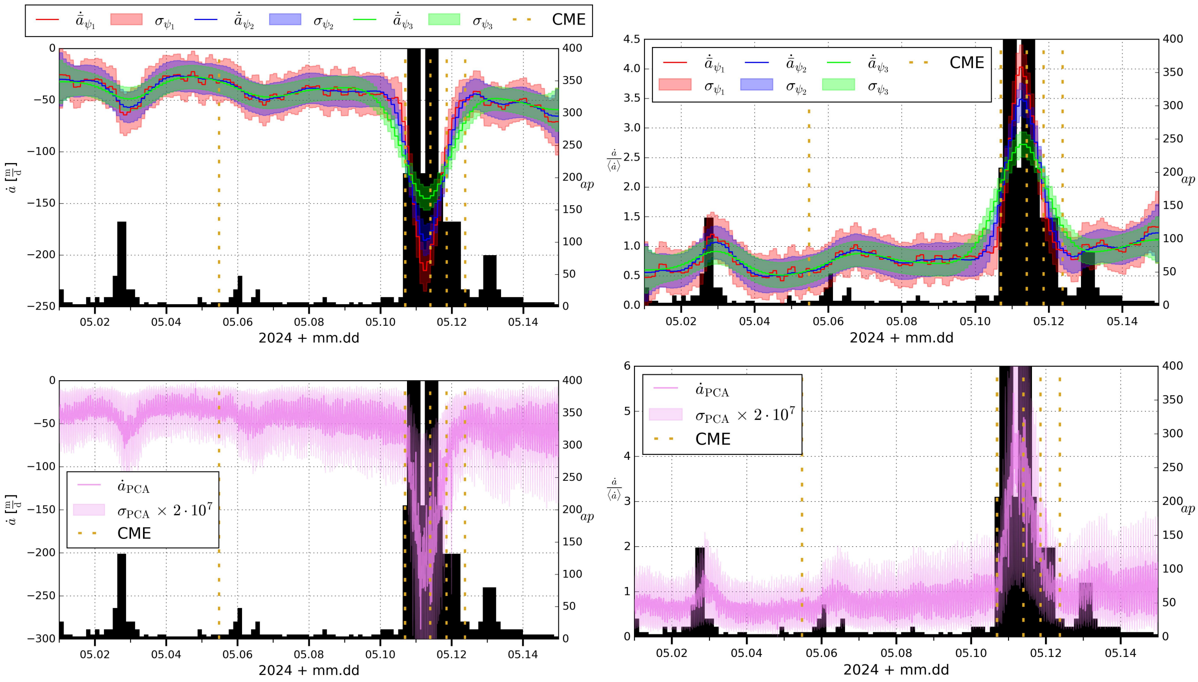

Figure 46: Resulting slope of the semi-major axis and its ratio to the mean slope are shown for the fit model approach (top row) and the Gaussian approach (bottom row). CME arrival times are marked with vertical yellow dotted lines and the $ap$ index is shown with black bars. Large orbital decay takes place at the same time as $ap$ values are at a maximum.

Figure 47 shows the time series of $\dot{\tilde{a}}_{\mathrm{PCA}}$ and the ratio to its mean value. The mean value is $\langle\dot{\tilde{a}}\rangle = -53.36\,\mathrm{md}^{-1}$. In the considered time interval the values for the smoothed slope of the semi-major axis range from about $-30\,\mathrm{md}^{-1}$ to $-224.20\,\mathrm{md}^{-1}$. The latter value is reached during the geomagnetic storm starting on 2024-05-10. $\dot{\tilde{a}}_{\mathrm{PCA}}$ is on 2024-05-11 about 4.2 times larger than on average. On 2024-05-04 there is very low geomagnetic activity and the orbital decay is about $30\,\mathrm{md}^{-1}$ on this day. This implies that the orbital decay is about 7.5 times larger during the extreme magnetic storm compared to the orbital decay during quiet times.

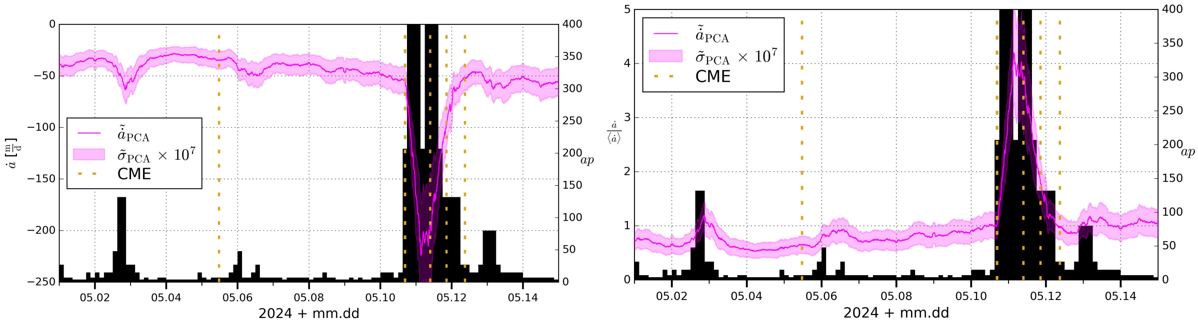

Figure 47: The left image shows the time series of the smoothed slope of the semi-major axis that is obtained with the integration approach. The image on the right shows the ratio of the smoothed slope to the mean of the smoothed slope of the semi-major axis. Vertical yellow dotted lines mark arrival times of CMEs and black bars show the *ap* index.

### 5.3.2 Sentinel-2A

Only one period $p_1 = 50.40\,\mathrm{min}$ marked in Fig. 48 (left) is modelled. The errors of the LSAs are given in the second column of Tab. 10 and range from 40.48 m to 41.17 m. For the fit model approach, the mean values of the orbital decay range from $-0.64\,\mathrm{md}^{-1}$ to $-0.77\,\mathrm{md}^{-1}$ and are given in the third column of Tab. 10. The mean orbital decay is $-0.92\,\mathrm{md}^{-1}$ for the Gaussian approach.
The spectra of each $\bar{a}_{\mathrm{Fit}}$ and the spectrum of $a_{\mathrm{PCA}}$ are shown in the Fig. 48 (right). Each spectrum is spiky above 576 min. Each $\bar{a}_{\mathrm{Fit}}$ spectrum has a certain structure centred around 144 min which repeats itself in the form of overtones for smaller periods. This structure and its overtones are damped with higher $\psi$. The spectrum of $a_{\mathrm{PCA}}$ is complicated and noisy.

Table 10: Errors of the LSAs of the fit model and mean slope of the semi-major axis with different constraining factors $\psi$ for Sentinel-2A in the year 2024.

| $\psi$ | $m_0$ [m] | $\langle \dot{a} \rangle$ $[\frac{\mathrm{m}}{\mathrm{d}}]$ |
|---|---|---|
| $\psi_1$ | 40.48 | -0.66 |
| $\psi_2$ | 40.93 | -0.64 |
| $\psi_3$ | 41.17 | -0.77 |

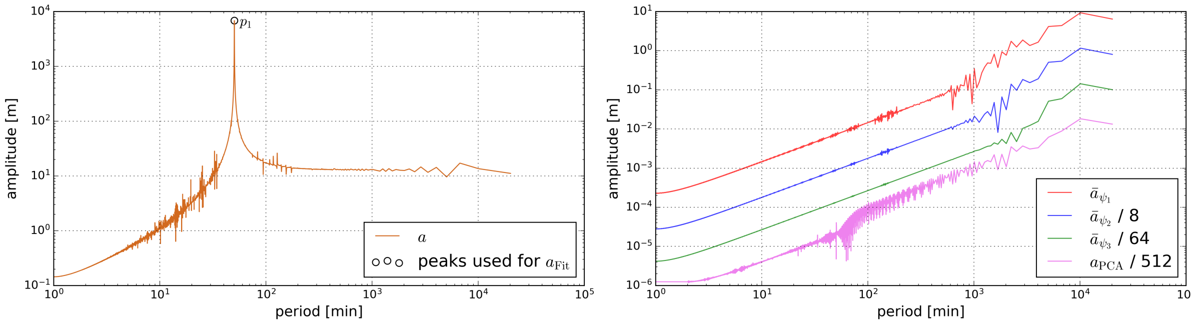

Figure 48: The spectrum of the semi-major axis is shown on the left. The period of 50.40 min, caused by the $C_{2,0}$ perturbation, is modelled in the LSA. On the right the spectra of the different $\bar{a}_{\mathrm{Fit}}$ and the spectrum of $a_{\mathrm{Gauss}}$ are shown. The spectra are shifted for better visibility.

The time series of $\bar{a}_{\mathrm{Fit}}$ and $a_{\mathrm{PCA}}$ are shown in Fig. 49 (top, left). The curves of the fit model approach are somewhat in accord but between 2024-05-08 and 2024-05-12 the reactions of the curves to an increase and subsequent decrease succeed with different response times based on the choice of $\psi$. The large increase on 2024-05-08 is a MAN and the large subsequent decrease is due to a geomagnetic storm. $a_{\mathrm{PCA}}$ is usually a couple meters below the curves of the fit model and on 2024-05-08 the curve executes a sharp jump of about 35 m. Between 2024-05-10 and 2024-05-12 an unusual strong decrease is visible for $a_{\mathrm{PCA}}$ as well. The errors have to be scaled for visibility. The error of $\bar{a}_{\mathrm{Fit}}$ is smaller with larger $\psi$. The error of $a_{\mathrm{PCA}}$ is the smallest. Kinks are visible for $a_{\mathrm{PCA}}$ at some day boundaries.

In Fig. 49 (top, right) the slope of the semi-major axis is shown for the fit model approach, and the same is shown for the integration approach (bottom row). During the analysed time interval the values for the slope of the semi-major axis range from about $80\,\mathrm{md}^{-1}$ to $-24.22\,\mathrm{md}^{-1}$ for the fit model approaches (errors not included) and range from about $1,200\,\mathrm{md}^{-1}$ to about $-300\,\mathrm{md}^{-1}$ for the Gaussian approach. If the days 2024-05-07 to 2024-05-09 are excluded, the upper boundary for the fit model approach is about $5\,\mathrm{md}^{-1}$. The slope with $\psi_1$ periodically reaches positive values while for the other choices of $\psi$ positive values are only reached between 2024-05-04 and 2024-05-05. By excluding the day 2024-05-08, $\dot{a}_{\mathrm{PCA}}$ reaches values between $20\,\mathrm{md}^{-1}$ and $-65\,\mathrm{md}^{-1}$. $\dot{\bar{a}}_{\psi_1}$ shows oscillations that are suppressed for higher $\psi$. A distinctive increase in orbital decay is visible on 2024-05-11 for all methods, which is in accordance with high *ap* values on these dates. Regardless of the method the largest value of orbital decay is reached on 2024-05-11 if the date 2024-05-08 is excluded for the integration approach. The orbital decay evaluated with $\dot{\bar{a}}_{\psi_1}$ is on 2024-05-11 about 37 times higher than on average. $\dot{a}_{\mathrm{PCA}}$ is on 2024-05-11 about 70 times larger than on average. During the geomagnetic storm starting on 2024-05-10 the largest orbital decays reached are $\dot{\bar{a}}_{\psi_1} = -24.22\,\mathrm{md}^{-1}$, $\dot{\bar{a}}_{\psi_2} = -16.96\,\mathrm{md}^{-1}$ and $\dot{\bar{a}}_{\psi_3} = -13.27\,\mathrm{md}^{-1}$.

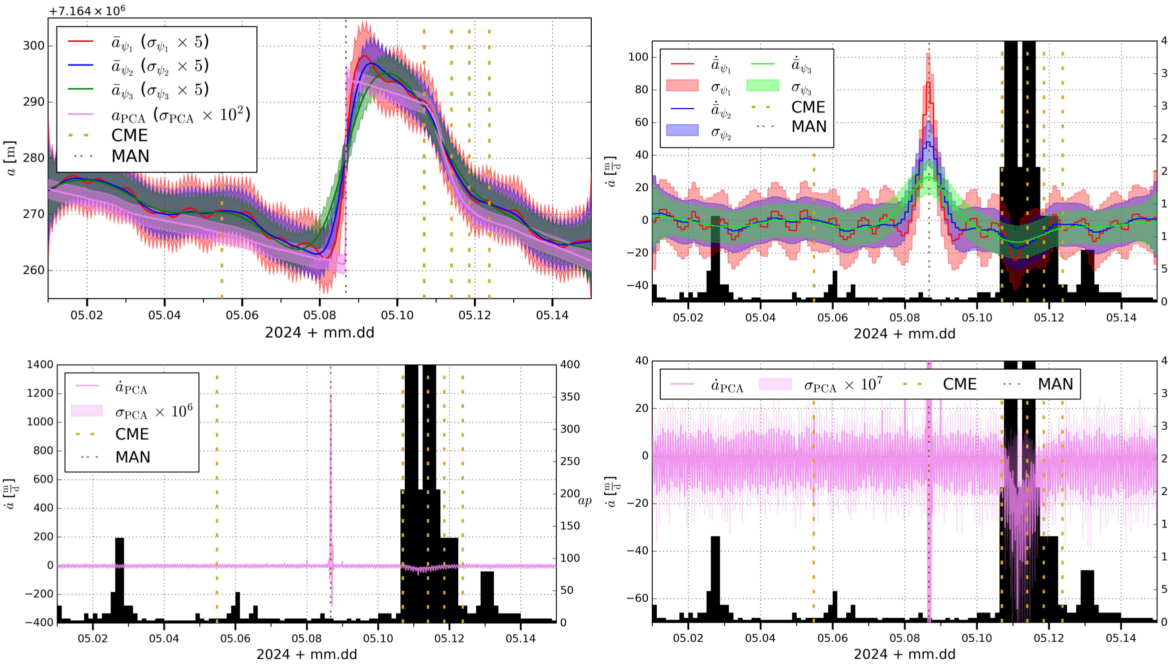

Figure 49: In the upper left panel the trend functions $\bar{a}_{\mathrm{Fit}}$ of the fit model approach and the numerically integrated semi-major axis $a_{\mathrm{PCA}}$ is shown. In the upper right panel the slopes of the trend functions of the fit model are shown. In the lower left panel the slope of $a_{\mathrm{PCA}}$ is shown. In the lower right panel a vertical cut-out of the slope obtained with the Gaussian approach is shown. Vertical yellow dotted lines mark CME arrival times and black bars represent the *ap* index. MAN times are indicated by brown vertical dotted lines.

Figure 50 shows the time series of $\tilde{a}_{\mathrm{PCA}}$. The mean value is $\langle\tilde{a}\rangle = -0.92\,\mathrm{md}^{-1}$. In the considered time interval the values for the smoothed slope of the semi-major axis range from about $490\,\mathrm{md}^{-1}$ to $-29.51\,\mathrm{md}^{-1}$, the latter value being reached during the geomagnetic storm. $\tilde{a}_{\mathrm{PCA}}$ is on 2024-05-11 about 32 times larger than on average. If the day 2024-05-08 is not included, the upper boundary is about $0\,\mathrm{md}^{-1}$. The orbital decay rate of Sentinel-2A is $-1.35\,\mathrm{md}^{-1}$ during quiet times on 2024-05-04. This means, that during the extreme geomagnetic storm on 2024-05-10 the orbital decay is 22 times larger than during quiet times.

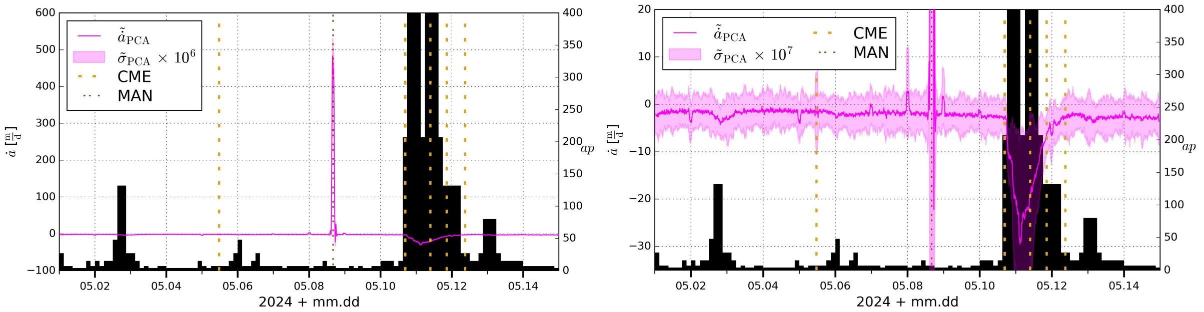

Figure 50: The smoothed slope of the semi-major axis obtained with the Gaussian approach is shown on the left. On the right a vertical zoom in is shown. CME arrival times are shown as vertical yellow dotted lines and the *ap* index is shown in the form of black bars. MAN times are indicated by brown vertical dotted lines.

### 5.3.3 Sentinel-3A

Only one period $p_1 = 50.52\,\text{min}$ marked in Fig. 51 (left) is modelled. The errors of the LSAs are given in the second column of Tab. 11 and range from 40.24 m to 40.80 m. For the fit model approach, the mean values of the orbital decay range from $-1.91\,\text{md}^{-1}$ to $-2.32\,\text{md}^{-1}$ and are given in the third column of Tab. 11. The mean orbital decay is $-2.00\,\text{md}^{-1}$ for the Gaussian approach.
The spectra of each $\bar{a}_{\text{Fit}}$ and the spectrum of $a_{\text{PCA}}$ are shown in Fig. 51 (right). All spectra are spiky above 0.4 d. The spectrum of $\bar{a}_{\psi_1}$ has a certain structure centred around 144 min which repeats itself in the form of overtones for smaller periods. For higher $\psi_2$ the structure at 144 min is also visible but the overtones are barely visible. For $\psi_3$ the structure at 144 min is barely visible and the overtones are not visible. The spectrum of $a_{\text{PCA}}$ is complicated and noisy.

Table 11: Errors of the LSAs of the fit model and mean slope of the semi-major axis with different constraining factors $\psi$ for Sentinel-3A in the year 2024.

| $\psi$ | $m_0$ [m] | $\langle\dot{a}\rangle$ [$\frac{\text{m}}{\text{d}}$] |
|---|---|---|
| $\psi_1$ | 40.24 | -2.32 |
| $\psi_2$ | 40.63 | -2.05 |
| $\psi_3$ | 40.80 | -1.91 |

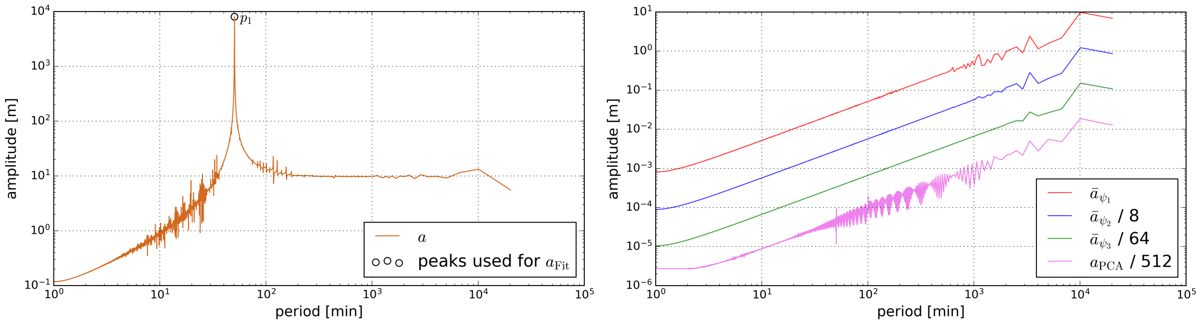

Figure 51: The spectrum of the semi-major axis is shown on the left. The marked period of $p_1 = 50.52\,\text{min}$ is induced by the $C_{2,0}$ perturbation and is modelled in the LSA. On the right the spectra of the different $\bar{a}_{\text{Fit}}$ and the spectrum of $a_{\text{Gauss}}$ is shown. The spectra are shifted for better visibility. The spectrum of the Gaussian approach significantly differs from the spectra obtained with the fit model approach.

The time series of $\bar{a}_{\text{Fit}}$ and $a_{\text{PCA}}$ are shown in Fig. 52 (top, left). The curves of the fit model approach are mostly in accord but between 2024-05-07 and 2024-05-12 the reactions of the curves to an increase and subsequent decrease succeed with different flexibility based on the choice of $\psi$. On 2024-05-08 $a_{\text{PCA}}$ executes a sharp jump of about 15 m. The large increase on 2024-05-08 is the product of a MAN and the large subsequent decrease is due to a geomagnetic storm. Between 2024-05-10 and 2024-05-12 an

unusual strong decrease is visible for $a_{\mathrm{PCA}}$ as well. The errors have to be scaled for visibility. The error of $\bar{a}_{\mathrm{Fit}}$ is smaller with larger $\psi$. The error of $a_{\mathrm{PCA}}$ is the smallest. Kinks are visible for $a_{\mathrm{PCA}}$ at some day boundaries.
In Fig. 52 (top, right) the slope of the semi-major axis is shown for the fit model approach, and the same is shown for the integration approach (bottom row). During the analysed time interval the values for the slope of the semi-major axis range from about $50\,\mathrm{md}^{-1}$ to about $-40\,\mathrm{md}^{-1}$ for the fit model approaches (errors included) and range from about $925\,\mathrm{md}^{-1}$ to about $-55\,\mathrm{md}^{-1}$ for the Gaussian approach. If the days 2024-05-07 to 2024-05-09 are excluded, the upper boundary for the fit model approach is about $25\,\mathrm{md}^{-1}$. The slope with $\psi_1$ periodically reaches positive values. Apart from the time interval 2024-05-07 to 2024-05-08, the slope with $\psi_2$ reaches positive values on 2024-05-02, on 2024-05-03, on 2024-05-06, on 2024-05-10 and on 2024-05-14 (may not be important as it is at the end of the time interval, where the fit model becomes inaccurate). Apart from the time interval 2024-05-07 to 2024-05-08 the slope with $\psi_3$ only reaches positive values on 2024-05-02. By excluding the day 2024-05-08, the upper boundary of $\dot{a}_{\mathrm{PCA}}$ is $15\,\mathrm{md}^{-1}$. $\dot{\bar{a}}_{\psi_1}$ shows oscillations that are suppressed for higher $\psi$. The largest orbital decay takes place on 2024-05-11 for all methods, which is in accordance with high *ap* values on these dates. The orbital decay evaluated with $\dot{\bar{a}}_{\psi_1}$ is on 2024-05-11 about 11 times higher than on average. $\dot{a}_{\mathrm{PCA}}$ is on 2024-05-11 about 28 times larger than on average. During the geomagnetic storm starting on 2024-05-10 the largest orbital decays reached are $\dot{\bar{a}}_{\psi_1} = -25.26\,\mathrm{md}^{-1}$, $\dot{\bar{a}}_{\psi_2} = -19.27\,\mathrm{md}^{-1}$ and $\dot{\bar{a}}_{\psi_3} = -14.16\,\mathrm{md}^{-1}$.

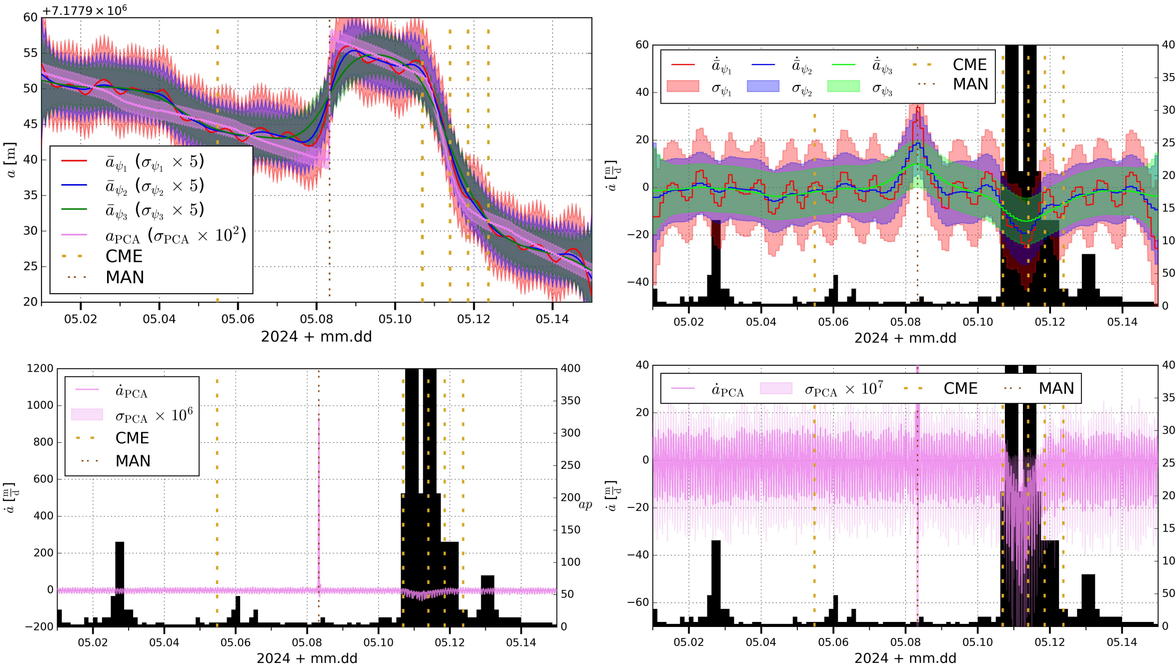

Figure 52: In the upper left panel the trend functions $\bar{a}_{\mathrm{Fit}}$ of the fit model approach and the numerically integrated semi-major axis $a_{\mathrm{PCA}}$ are shown. In the upper right panel the slopes of the trend functions of the fit model are shown. In the lower left panel the slope of $a_{\mathrm{PCA}}$ is shown. In the lower right panel a vertical cut-out of the slope obtained with the Gaussian approach is shown. Vertical yellow dotted lines mark CME arrival times and black bars represent the *ap* index. MAN times are indicated by brown vertical dotted lines.

Figure 53 shows the time series of $\tilde{\dot{a}}_{\mathrm{PCA}}$. The mean value is $\langle\tilde{\dot{a}}\rangle = -2.02\,\mathrm{md}^{-1}$. In the observed time interval the values for the smoothed slope of the semi-major axis range from about $240\,\mathrm{md}^{-1}$ to about $-26.99\,\mathrm{md}^{-1}$, the latter value being reached during the geomagnetic storm. If the day 2024-05-08 is not included, the upper boundary is about $1\,\mathrm{md}^{-1}$. The orbital decay rate of Sentinel-3A is $-1.34\,\mathrm{md}^{-1}$ during the quiet day 2024-05-04. This means that during the extreme geomagnetic storm on 2024-05-10 the orbital decay is 20 times larger than during quiet times.

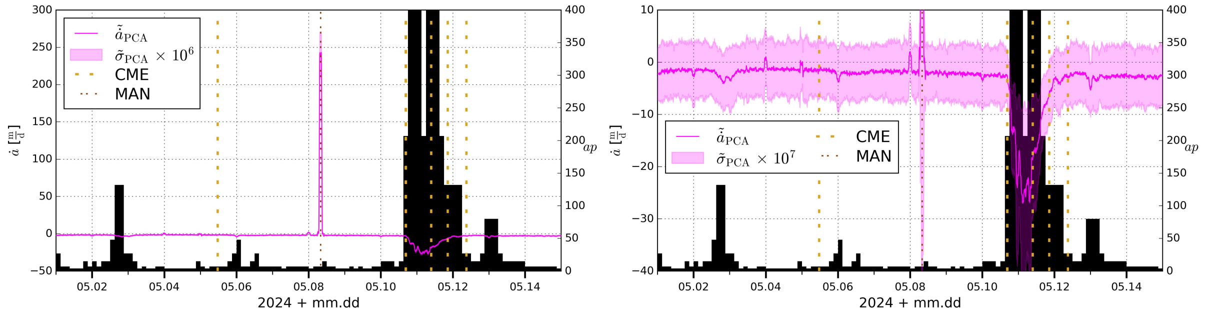

Figure 53: The smoothed slope of the semi-major axis obtained with the Gaussian approach is shown on the left. On the right a vertical zoom in is shown. CME arrival times are shown as vertical yellow dotted lines and the *ap* index is shown in the form of black bars. MAN times are indicated by brown vertical dotted lines.

## 5.4 Summary of Evaluated Orbital Decays during Geomagnetic Storms

In Tab. 12 the maximum orbital decays reached during the geomagnetic storms starting on 2018-08-26, 2023-02-26, 2023-03-23 and 2024-05-10 are summarised. For GRACE-FO-1 in 2018 the orbital decay $\dot{\tilde{a}}_{\psi_1}$ during the geomagnetic storm cannot be adequately established because the orbital decay is dominated by oscillations. Similarly for Sentinel-1A in 2023 the maximum orbital decay during a geomagnetic storm cannot be properly established with the fit model approach because of frequently performed MANs.

Table 12: Maximum orbital decays during the geomagnetic storms for different satellites. In the first column the start time of the geomagnetic storm is listed. "–" denotes that there is no data available. "≀" denotes that no value can be adequately determined because the orbital decay is dominated by oscillations. "⅄" denotes that no value can be adequately determined because the orbital decay is too distorted by MANs.

| Storm (start date) | Satellite | $\dot{\tilde{a}}_{\psi_1}$ [md$^{-1}$] | $\dot{\tilde{a}}_{\psi_2}$ [md$^{-1}$] | $\dot{\tilde{a}}_{\psi_3}$ [md$^{-1}$] | $\tilde{\dot{a}}_{\text{PCA}}$ [md$^{-1}$] | $\tilde{\dot{a}}_{\text{ACC}}$ [md$^{-1}$] | $\tilde{\dot{a}}_{\text{ACC,shifted}}$ [md$^{-1}$] |
|---|---|---|---|---|---|---|---|
| 2018-08-26 | GRACE-FO-1 | ≀ | -3.59 | -2.57 | -7.35 | -7.51 | -7.51 |
| 2023-02-26 | GRACE-FO-1 | -49.18 | -43.34 | -38.38 | -51.46 | - | - |
| | Swarm-A | -101.36 | -96.87 | -86.10 | -98.59 | - | - |
| | Sentinel-1A | ⅄ | ⅄ | ⅄ | -6.81 | - | - |
| 2023-03-23 | GRACE-FO-1 | -54.22 | -50.48 | -46.04 | -61.90 | - | - |
| | Swarm-A | -108.74 | -101.39 | -89.13 | -111.68 | - | - |
| | Sentinel-1A | ⅄ | ⅄ | ⅄ | -8.78 | - | - |
| 2024-05-10 | Swarm-A | -214.81 | -185.48 | -144.99 | -224.20 | - | - |
| | Sentinel-2A | -24.22 | -16.96 | -13.27 | -29.51 | - | - |
| | Sentinel-3A | -25.26 | -19.27 | -14.16 | -26.99 | - | - |

# 6 Discussion

## 6.1 Fit Model Approach

The fit model approach is applied to data sets which have a cadence of 30 s. In each case $n_{\text{fac}} = 10$ subintervals are fitted per day. In each case LSAs are performed with the same three different constraining factors $\psi_1 = 10^3$, $\psi_2 = 10^4$ and $\psi_3 = 10^5$. In most cases only $R = 1$ period is modelled.

A larger constraining factor leads to results being less prone to oscillations but at the cost of dynamical flexibility. A consequence is the underestimation of temporal increase in orbital decay due to a geomagnetic storm. For satellites with large orbital decay rates in general, a constraining factor $\psi_1 < \psi < \psi_2$ will produce results where the slope of the semi-major axis does not contain any oscillations, but larger orbital decay induced by medium geomagnetic activity ($ap \approx 50$) will still be visible. However, the values of larger decay will still be underestimated. For better estimation of the larger orbital decay induced by medium geomagnetic activity, a constraining factor of $\psi \leq \psi_1$ is needed. For further investigations a dynamical constraining approach may be researched. A possible strategy may be to link the constraining to geomagnetic indices. If the constraining is controlled in such a way that it decreases when geomagnetic indices signal magnetic storm activity, the increased orbital decay during a geomagnetic storm might be underestimated less.

The results of both GRACE-FO-1 and Swarm-A in 2023 and Swarm-A in 2024 show that the fit model approach is able to adequately model orbital decay of at least $-20\,\mathrm{m d^{-1}}$. Moreover, geomagnetic storms manifest themselves as unusual steep and deep drops in the orbital slope, which coincide with the arrival times of CMEs (but not all CMEs cause geomagnetic storms).
However, the results of GRACE-FO-1 in 2018 and the results of the Sentinel satellites show that the fit model approach with the aforementioned configurations cannot model low orbital decay ($\dot{\bar{a}} \gtrsim -10\,\mathrm{m d^{-1}}$) with adequate quality. The calculated slope of the semi-major axis reaches positive values frequently without the presence of MANs. Slopes obtained from LSAs performed with larger constraining factors reach positive values less frequently. Nevertheless, even with stronger constraining positive values for the slope of the semi-major axis are constantly enclosed in the error band. Only during the extreme geomagnetic storm in May 2024 temporarily no positive values are contained inside the error band of the slope of the semi-major axis for both Sentinel-2A and Sentinel-3A.

The case of GRACE-FO-1 in 2018 shows that prominent very long periods ($p \gtrsim 1\,\mathrm{d}$) that are not modelled negatively impact the results. LSAs with strong constraining are impacted less by the prominent very long periods. This suggests, that (at least in the case of low orbital decay) it is essential to model prominent very long periods to evaluate the impact of geomagnetic storms on the orbital decay. It is not clear why there is a very long period $p_2 = 5.55\,\mathrm{d}$ appearing in the analysis of GRACE-FO-1 in 2018. Its origin and evolution may yet be investigated.

The results of Sentinel-1A show that the fit model is not able to model orbital decay adequately if frequent MANs are performed. It may be possible to obtain better results, if more subintervals are fitted per day (of course this also implies that the constraining factor needs to be adjusted). Alternatively, the fit model could be modified in such a way that information about MANs is incorporated directly into the fit model.

Moreover, it may be advantageous for further research to extend the simulation in Sect. 4.2. MANs, very long periods (above 1 d), inaccurately determined prominent periods, more complex storm profiles, etc. may be added to the simulation. As mentioned in Sect. 4.1.1.2, the *L-curve criterion* may be implemented to find an optimal value for the constraining factor $\psi$. Moreover, the relationship between different $\psi$ and the peak value of orbital decay $d - h$ in the simulation may be investigated to possibly find a measure for the underestimation and the uncertainty of the peak value. Naturally, results also depend on the choice of $n_{\mathrm{fac}}$ and the sampling of the data. For future research, the importance of $n_{\mathrm{fac}}$ on the quality of the LSA may be investigated further.

With the configurations $n_{\mathrm{fac}}$, $R$ and the time sampling of the data used in the analysis of all satellites, the Gaussian approach proves to be more time efficient computing wise. But the computation time of the LSA for the fit model and the numerical integration of the Gaussian approach all heavily depend on the aforementioned variables. It may be possible, that for example, a slightly lower sampling does not heavily affect the quality of the results. For further research this may be investigated.

An advantage of the fit model approach over the Gaussian approach is that the evolution of the amplitudes and periods can be further analysed (of course, the fit model can also be applied to the results of the Gaussian approach). An analysis of the estimated amplitudes may provide further insights into the behaviour of the fit model.

It should be noted that in this work the error propagation is done in a rather “cheap” manner. For further research, the covariances of the LSA of the fit model may be taken into account.

## 6.2 Gaussian Approach

The Gaussian approach is applied for most satellites with PCAs. The PCAs are resampled to 30 s for most analyses. In the case of GRACE-FO-1 in 2018 the PCAs are resampled to 5 s to compare the results of the integration with PCAs to the results of the integration with ACC data.

With the Gaussian approach the impact of low geomagnetic activity down to $ap = 30$ can be observed in the calculated orbital decay. The Gaussian approach has in general more sensitivity regarding fluctuations in the orbital decay caused by geomagnetic activity than the fit model approach. However, compared to the fit model approach, the slope of the semi-major axis obtained with the Gaussian approach may need to be smoothed to enable better interpretation of the results.

A direct comparison between the results obtained with the integration approach with ACC data and the results obtained with the fit model approach in the analysis of GRACE-FO-1 in 2018 is not possible because the results of the latter method are not of adequate quality (low orbital decay and not modelled prominent very long periods). To get a direct comparison between the integration approach with ACC data, the integration approach with PCAs and the fit model, an analysis of GRACE-FO-1 in 2023 (or another year with a large enough orbital decay rate) needs to be performed.
Nevertheless, an indirect comparison between the Gaussian approach with ACC data and the fit model approach is still possible. The analysis of GRACE-FO-1 in 2018 shows that results of the integration approach do not differ greatly if ACC data, PCAs or even shifted ACC data are used. In this sense, it is highly probable that this would also be the case when there is larger orbital decay as there is in 2023 for example.

Even though they do not differ in the results regarding larger orbital decay due to geomagnetic activity, there are several major differences between the results obtained via the integration approach with PCAs, the results when ACC data is used or when shifted ACC data is used. Most of this differences can be explained with the help of Fig. 11 and by looking at Gauss's perturbation equation (11). One difference is the slope of the semi-major axis obtained with PCAs exhibits larger oscillations than the slope obtained with ACC data. This is because the PCAs exhibit larger oscillations in the along-track direction than the ACC data.
Another difference is that the obtained time series for the semi-major axis are not in phase with each other. This is because the along-track component of the accelerations of PCAs and ACC data are also not in phase. The reason for this is not clear and may be investigated in the future.
Another difference is that the slope obtained with the ACC data has a larger error than the one obtained with PCAs or shifted ACC data. This is because the radial component of the ACC data is larger than the radial component of the PCAs.
Another difference is that the error band of the orbital slope obtained with the shifted ACC data at the beginning is smaller and at the end larger than the error band of the orbital slope obtained with PCAs. The reason for this phenomenon has yet to be determined.
Another difference is that the quality of the PCAs suffers from day boundary problems because orbits are estimated in a daily manner. This leads to spikes in the orbital slope at day boundaries. This can also be seen in the results of the Sentinel satellites. To lessen this effect longer orbits could be estimated.

It is important that at least in the along-track direction the mean values of both datasets coincide. The reason for this is because in Gauss's perturbation equation for the semi-major axis there is no cross-track component and the radial component only corresponds to the amplitude of an oscillating term which is proportional to the eccentricity (which is small for almost circular orbits). Only the along-track component is multiplied with a linear term.

The results of the Sentinel satellites show that compared to the fit model approach, the integration approach reacts faster to MANs. However, the results of Sentinel-1A show that MANs can cause problems during the integration process resulting in a jump that is too large. In order to improve the Gaussian approach, information about the MANs could be taken into account during the orbit estimation and during integration. Alternatively, the numerical integration may be ended before a MAN and started on the next day after the MAN. This way, the MANs can be avoided. Moreover, numerical integration with an adaptive step size may be advantageous as well. If the Gaussian approach is done with ACC data, this problem does not exist, because the sampling of the ACC data is significantly higher.

The results of Sentinel-1A also show that on the start of almost each day that contains MANs there is an exceptionally large increase in the slope obtained with PCAs. These are visible as minor discrepancies in $a_{\text{PCA}}$. The main reason for this is because the phase measurement RMS of daily POD is usually larger on days that contain a MAN.

Like for the fit model approach, a more complete analysis of error propagation may be performed for the integration approach as well.

## 6.3 Further Applications

The Gaussian approach can only be applied if there is ACC data or estimated PCAs available, i.e., for satellites equipped with an on-board accelerometer and a GNSS receiver, respectively. Most satellites relying on precise orbit determination feature GNSS receivers which enables the Gaussian approach with PCAs. For space debris and inactive satellites only the fit model approach is possible in theory. If the fit model approach can be significantly improved, the application with spherical satellite laser ranging satellites may even become possible.

However, if there is observational data with adequate sampling and quality, an orbit can be estimated even without a GNSS receiver. This way the osculating semi-major axis can be obtained along with estimated PCAs (if the amount of data is sufficient). Thus, both methods can in theory also be applied to space debris and inactive satellites, if the aforementioned requirements are fulfilled. In case of a spherical laser ranging satellite only the Gaussian approach can be applied. The reason for this is that such a satellite is usually stationed at a higher LEO orbit and because of its shape and density the satellite is expected to have little orbital decay (which the fit model in its current form is not able to model adequately).

## 6.4 Indicators for Orbital Decay

For both GRACE-FO-1 and Swarm-A in 2023 there are three instances where the changes in orbital decay (Gaussian approach) do not always coincide with changes in the geomagnetic indices and the modelled air density evaluated with the DTM2013 model.
One instance is the interval from 2023-02-17 to 2023-02-19. There is low orbital decay which is in accordance with low $ap$ and low $Dst$ values. On 2023-02-17 and 2023-02-19 there are also low values of modelled air density visible. However, on the day 2023-02-18 there is increased modelled air density visible.
Moreover, after the geomagnetic storm on 2023-03-23 the orbital decay decreases, which is in accordance with a decrease in the $ap$ index and a decrease in modelled air density. On 2023-03-30 the orbital decay increases again which is also in accordance with an increase in the $ap$ index. However, the modelled air density decreases further.
Between 2023-03-02 and 2023-03-14 a prolonged increase is visible in both the orbital decay and the modelled air density but not in the $ap$ index and the $Dst$ index. The exact reason for the large orbital decay during this interval is not clear. A possible explanation may be that during this time interval several auroral substorms occurred. These substorms are better measured with the $AE$ index. Unfortunately, there is no $AE$ index data available for this time span in 2023. Alternative $AE$ indices may be analysed to investigate substorm activity during the mentioned time interval.

To correlate geomagnetic activity with orbital decay the magnetometer measurements of Swarm-A could be analysed. This would be the most direct way to investigate the correlation between orbital decay and geomagnetic activity. Moreover, the influence of the $\beta$ angle on orbital decay may also be investigated further.

# 7 Conclusion

The objective of this thesis was to investigate the orbital decay of LEO satellites during periods with space weather events. BSW is used to compute RED-DYN (NL and NG) orbits of the satellites with GPS measurements. Both the osculating semi-major axis derived from the RED-DYN orbits as well as the PCAs that are used to compensate for not explicitly modelled non-gravitational accelerations are further used. A constrained piecewise linear fit model is applied in a LSA onto the osculating semi-major axis. The fit model is composed of a time-varying trend function and time-varying amplitudes of the most dominant periodic oscillations. The trend function of the fit model is then differentiated with respect to time to obtain the orbital slope. On the other hand, PCAs and in the case of GRACE-FO-1, calibrated ACC data from the on-board accelerometer are used to numerically integrate Gauss's perturbation equation to directly obtain the orbital decay. The results of both methods as well as the simulation of the fit model approach show that based on the orbit of the satellite both approaches can be used to evaluate the orbital decay of the satellite. Furthermore, the increased orbital decay induced by geomagnetic storms that are triggered by CMEs can be measured with both methods.

The quality of the results obtained with the fit model approach decreases if there are prominent very long periods that are not or insufficiently modelled. The fit model is not able to model low orbital decay with adequate quality. Moreover, the orbital decay during a geomagnetic storm evaluated with the fit model approach is underestimated due to constraining. The quality of the Gaussian approach performed with PCAs is negatively affected by day boundary problems. Both methods suffer from frequently performed MANs. While the fit model reacts based on the constraining factor slowly to a MAN, the integration method reacts in a more "instantaneous" manner but may "overreact" due to integration problems. The results of GRACE-FO-1 obtained with using ACC data validate the use of PCAs in the Gaussian approach.
In both cases, the obtained orbital slope is mostly in accordance with strong and medium geomagnetic indices $ap$, $Dst$ and $AE$ as well as with the modelled air density evaluated with the DTM2013 model. Strong geomagnetic storms are visible as large and steep increases in orbital decay. The evaluated maximum smoothed orbital decay reached during the geomagnetic storm on 2018-08-26 for GRACE-FO-1 is $-7.35\,\mathrm{m}\mathrm{d}^{-1}$ when PCAs are used and it is $-7.51\,\mathrm{m}\mathrm{d}^{-1}$ when ACC data is used. With the Gaussian approach performed with PCAs the maximum smoothed orbital decay reached during the geomagnetic storm on 2023-02-26 is $-51.46\,\mathrm{m}\mathrm{d}^{-1}$ for GRACE-FO-1, $-98.59\,\mathrm{m}\mathrm{d}^{-1}$ for Swarm-A and $-6.81\,\mathrm{m}\mathrm{d}^{-1}$ for Sentinel-1A. The maximum smoothed orbital decay reached during the geomagnetic storm on 2023-03-23 is $-61.90\,\mathrm{m}\mathrm{d}^{-1}$ for GRACE-FO-1, $-111.68\,\mathrm{m}\mathrm{d}^{-1}$ for Swarm-A and $-8.78\,\mathrm{m}\mathrm{d}^{-1}$ for Sentinel-1A. The maximum smoothed orbital decay reached during the extreme geomagnetic storm on 2024-05-10 is $-224.20\,\mathrm{m}\mathrm{d}^{-1}$ for Swarm-A, $-29.51\,\mathrm{m}\mathrm{d}^{-1}$ for Sentinel-2A and $-26.99\,\mathrm{m}\mathrm{d}^{-1}$ for Sentinel-3A.

During the work several questions arose such as the origin of the prominent very long period of $p_2 = 5.55\,\mathrm{d}$ of GRACE-FO-1 in 2018. This along with its evolution have yet to be investigated. As mentioned above, the used methods exhibit different weaknesses but the methods have potential for improvement. For future research, the presented methods may be developed further to increase quality, efficiency and extend the possibilities for application.

# 8 Acknowledgements

I would like to thank A. Jäggi and D. Arnold for the primary supervision and guidance of this thesis. I would also like to thank V.-M. Mercea and L. Kleint for secondary supervision and for giving me insights about the space weather perspective. In particular, I would like to thank D. Arnold for showing me how to operate the BSW and for providing me with the data. Additionally, I would like to thank M. Lasser for the provision of the GRACE-FO-1 ACC data. Moreover, I would like to thank my friends J. Berchtold, A. Hauser, F. Mele, D. Schwarz, B. Seewer and Y. Steiner for the fruitful and inspiring conversations.

# References

Beutler, G. (2005). *Methods of Celestial Mechanics*. Springer. https://doi.org/10.1007/b138225

Bezděk, A., Sebera, J., & Klokočník, J. (2018). Calibration of Swarm accelerometer data by GPS positioning and linear temperature correction. *Advances in Space Research*, *62*(2), 317–325. https://doi.org/https://doi.org/10.1016/j.asr.2018.04.041

Bowman, B., Tobiska, W. K., Marcos, F., Huang, C., Lin, C., & Burke, W. (2008). A New Empirical Thermospheric Density Model JB2008 Using New Solar and Geomagnetic Indices. In *Aiaa/aas astrodynamics specialist conference and exhibit*. https://doi.org/10.2514/6.2008-6438

Branduardi-Raymont, G., Berthomier, M., Bogdanova, Y., Carter, J., Collier, M., Dimmock, A., Dunlop, M., Fear, R., Forsyth, C., Hubert, B., Kronberg, E., Laundal, K., Lester, M., Milan, S., Oksavik, K., Østgaard, N., Palmroth, M., Plaschke, F., Porter, F., . . . Yamauchi, M. (2021). Exploring solar-terrestrial interactions via multiple imaging observers. *Experimental Astronomy*, *54*(2-3), 361–390. https://doi.org/10.1007/s10686-021-09784-y

Bruinsma, S. (2015). The DTM-2013 thermosphere model. *J. Space Weather Space Clim.*, *5*, A1. https://doi.org/10.1051/swsc/2015001

Buzulukova, N., & Tsurutani, B. (2022). Space Weather: From solar origins to risks and hazards evolving in time. *Frontiers in Astronomy and Space Sciences*, *9*. https://doi.org/10.3389/fspas.2022.1017103

Cai, H., Yang, Y., Gehly, S., He, C., & Jah, M. (2020). Sensor tasking for search and catalog maintenance of geosynchronous space objects. *Acta Astronautica*, *175*. https://doi.org/10.1016/j.actaastro.2020.05.063

Dach, R. (2023). Fundamentalastronomie I. University of Bern, root number 447504.

Dach, R., Lutz, S., Walser, P., & Fridez, P. (2015). Bernese GNSS Software Version 5.2. https://doi.org/10.7892/boris.72297

Dang, T., Li, X., Luo, B., Li, R., Zhang, B., Pham, K., Ren, D., Chen, X., Lei, J., & Wang, Y. (2022). Unveiling the Space Weather During the Starlink Satellites Destruction Event on 4 February 2022 [e2022SW003152 2022SW003152]. *Space Weather*, *20*(8), e2022SW003152. https://doi.org/https://doi.org/10.1029/2022SW003152

Donlon, C., Berruti, B., Buongiorno, A., Ferreira, M.-H., Féménias, P., Frerick, J., Goryl, P., Klein, U., Laur, H., Mavrocordatos, C., Nieke, J., Rebhan, H., Seitz, B., Stroede, J., & Sciarra, R. (2012). The global monitoring for environment and security (gmes) sentinel-3 mission [The Sentinel Missions - New Opportunities for Science]. *Remote Sensing of Environment*, *120*, 37–57. https://doi.org/https://doi.org/10.1016/j.rse.2011.07.024

Drusch, M., Del Bello, U., Carlier, S., Colin, O., Fernandez, V., Gascon, F., Hoersch, B., Isola, C., Laberinti, P., Martimort, P., Meygret, A., Spoto, F., Sy, O., Marchese, F., & Bargellini, P. (2012). Sentinel-2: Esa's optical high-resolution mission for gmes operational services [The Sentinel Missions - New Opportunities for Science]. *Remote Sensing of Environment*, *120*, 25–36. https://doi.org/https://doi.org/10.1016/j.rse.2011.11.026

Dungey, J. W. (1961). Interplanetary Magnetic Field and the Auroral Zones. *Phys. Rev. Lett.*, *6*, 47–48. https://doi.org/10.1103/PhysRevLett.6.47

Eastwood, J. P., Hietala, H., Toth, G., Phan, T. D., & Fujimoto, M. (2015). What Controls the Structure and Dynamics of Earth's Magnetosphere? *188*(1-4), 251–286. https://doi.org/10.1007/s11214-014-0050-x

Friis-Christensen, E., Lühr, H., Knudsen, D., & Haagmans, R. (2008). Swarm – an earth observation mission investigating geospace. *Advances in Space Research*, *41*(1), 210–216. https://doi.org/https://doi.org/10.1016/j.asr.2006.10.008

Gopalswamy, N. (2022). The Sun and Space Weather. *Atmosphere*, *13*(11). https://doi.org/10.3390/atmos13111781

Hansen, P. C. (2001, January). The L-Curve and Its Use in the Numerical Treatment of Inverse Problems.

Heiskanen, W. A., & Moritz, H. (1967). Physical Geodesy.

Iucci, N., Levitin, A. E., Belov, A. V., Eroshenko, E. A., Ptitsyna, N. G., Villoresi, G., Chizhenkov, G. V., Dorman, L. I., Gromova, L. I., Parisi, M., Tyasto, M. I., & Yanke, V. G. (2005). Space weather conditions and spacecraft anomalies in different orbits. *Space Weather*, *3*(1). https://doi.org/https://doi.org/10.1029/2003SW000056

Jäggi, A. (2007). Pseudo-Stochastic Orbit Modeling of Low Earth Satellites Using the Global Positioning System. *Geodätisch-geophysikalische Arbeiten in der Schweiz Volume 73.*

Jäggi, A. (2022a). Astrodynamik I. University of Bern, root number 636.

Jäggi, A. (2022b). Numerische Methoden der Physik, University of Bern, root number 447303.

Jäggi, A. (2024). Astrodynamik II. University of Bern, root number 660.

Jäggi, A., & Arnold, D. (2024). Übungen zu Astrodynamik II. University of Bern, root number 447508.

Jäggi, A., Arnold, D., & Lasser, M. (2024). Specialist Course: Gravity Field Determination from Satellite Tracking Data. University of Bern, root number 447509.

Kessler, D. J., & Cour-Palais, B. G. (1978). Collision frequency of artificial satellites: The creation of a debris belt. *Journal of Geophysical Research: Space Physics*, *83*(A6), 2637–2646. https://doi.org/https://doi.org/10.1029/JA083iA06p02637

Kilpua, E., Koskinen, H. E. J., & Pulkkinen, T. I. (2017). Coronal mass ejections and their sheath regions in interplanetary space. *Living Reviews in Solar Physics*, *14*(1), Article 5, 5. https://doi.org/10.1007/s41116-017-0009-6

Koskinen, H. (2011). *Physics of Space Storms: From the Solar Surface to the Earth*. Springer-Verlag. https://doi.org/10.1007/978-3-642-00319-6

Krauss, S., Behzadpour, S., Temmer, M., & Lhotka, C. (2020). Exploring Thermospheric Variations Triggered by Severe Geomagnetic Storm on 26 August 2018 Using GRACE Follow-On Data. *Journal of Geophysical Research: Space Physics*, *125*(5). https://doi.org/https://doi.org/10.1029/2019JA027731

Landerer, F. W., Flechtner, F. M., Save, H., Webb, F. H., Bandikova, T., Bertiger, W. I., Bettadpur, S. V., Byun, S. H., Dahle, C., Dobslaw, H., Fahnestock, E., Harvey, N., Kang, Z., Kruizinga, G. L. H., Loomis, B. D., McCullough, C., Murböck, M., Nagel, P., Paik, M., ... Yuan, D.-N. (2020). Extending the Global Mass Change Data Record: GRACE Follow-On Instrument and Science Data Performance [e2020GL088306 2020GL088306]. *Geophysical Research Letters*, *47*(12), e2020GL088306. https://doi.org/https://doi.org/10.1029/2020GL088306

Lasser, M., Meyer, U., Arnold, D., & Jäggi, A. (2023). AIUB-GRACE-FO operational GRACE Follow-On monthly gravity field solutions - release 02. https://doi.org/10.5880/ICGEM.2023.004

Mao, X., Arnold, D., Girardin, V., Villiger, A., & Jäggi, A. (2021). Dynamic GPS-based LEO orbit determination with 1 cm precision using the Bernese GNSS Software. *Advances in Space Research*, *67*(2), 788–805. https://doi.org/https://doi.org/10.1016/j.asr.2020.10.012

Miteva, R., Samwel, S. W., & Tkatchova, S. (2023). Space Weather Effects on Satellites. *Astronomy*, *2*(3), 165–179. https://doi.org/10.3390/astronomy2030012

Picone, J. M., Hedin, A. E., Drob, D. P., & Aikin, A. C. (2002). NRLMSISE-00 empirical model of the atmosphere: Statistical comparisons and scientific issues. *Journal of Geophysical Research: Space Physics*, *107*(A12), SIA 15-1-SIA 15–16. https://doi.org/https://doi.org/10.1029/2002JA009430

Pistillo, C. (2023). Introduction to Programming and Computational Physics - with Exercises. Phil.-nat faculty, University of Bern, root number 8725.

Pontin, D. I., & Priest, E. R. (2022). Magnetic reconnection: MHD theory and modelling. *Living Reviews in Solar Physics*, *19*(1), Article 1, 1. https://doi.org/10.1007/s41116-022-00032-9

Savitzky, A., & Golay, M. J. E. (1964). Smoothing and differentiation of data by simplified least squares procedures. *Analytical Chemistry*, *36*, 1627–1639. https://doi.org/10.1021/ac60214a047

Stix, M. (2002). *The Sun: An Introduction, Second Edition*. Springer Berlin, Heidelberg. https://doi.org/10.1007/978-3-642-56042-2

Torres, R., Snoeij, P., Geudtner, D., Bibby, D., Davidson, M., Attema, E., Potin, P., Rommen, B., Floury, N., Brown, M., Traver, I. N., Deghaye, P., Duesmann, B., Rosich, B., Miranda, N., Bruno, C., L'Abbate, M., Croci, R., Pietropaolo, A., ... Rostan, F. (2012). Gmes sentinel-1 mission [The Sentinel Missions - New Opportunities for Science]. *Remote Sensing of Environment*, *120*, 9–24. https://doi.org/https://doi.org/10.1016/j.rse.2011.05.028

Vallado, D. A., & McClain, W. D. (2013). *Fundamentals of Astrodynamics and Applications, Fourth Edition*.

Vourlidas, A., Lynch, B. J., Howard, R. A., & Li, Y. (2013). How Many CMEs Have Flux Ropes? Deciphering the Signatures of Shocks, Flux Ropes, and Prominences in Coronagraph Observations of CMEs. *Solar Physics*, *284*(1), 179–201. https://doi.org/10.1007/s11207-012-0084-8

Wurz, P. (2022). Anleitung zum Physikpraktikum I. University of Bern, root number 652.

# A Appendix: Smoothing Process

## A.1 Moving Average

The time series of $\dot{a}_{\text{Gauss}}$ obtained from numerically solving Gauss's perturbation Eq. (11) as well as its error $\sigma_{\text{Gauss}}$, primarily exhibit short-periodic oscillations. Trends (and longer periods) in these elements are better visible if the periods that create those oscillations are smoothed out. In this work, a moving average filter is applied for smoothing.

Let $E \in \{\dot{a}_{\text{Gauss}}, \sigma_{\text{Gauss}}\}$. By choosing an averaging period $\Delta t$ (window length), the mean variable $\tilde{E}(t; \Delta t(t))$ at the epoch $t$ is defined as:

$$\tilde{E}(t; \Delta t(t)) = \frac{1}{\Delta t} \int_{t-\frac{\Delta t}{2}}^{t+\frac{\Delta t}{2}} E(t')\mathrm{d}t'. \tag{62}$$

By choosing the averaging period $\Delta t$ as a prominent short period, that causes oscillations in $E$, this period is filtered out. However, if the averaging period $\Delta t$ is not chosen carefully, it is possible that false signals are generated which are not of physical origin.

It is possible that there are multiple prominent short periods causing oscillations. In this case, there are two ways, to choose an appropriate $\Delta t$: Either $\Delta t$ is chosen significantly longer than those short periods or $\Delta t$ is set as an integer multiple of the short periods:

$$\Delta t \gg \tau \qquad \vee \qquad \Delta t = n \cdot \tau \qquad\qquad \forall \tau \in \mathbb{T},\ \forall n \in \mathbb{N}_+, \tag{63}$$

where $\mathbb{T}$ is the set of the (prominent) short periods.

If the amplitudes of the prominent short periods are too large relative to faint local trends, the latter are not visible. The faint local trends become distinguishable, if the prominent short periods are filtered out (when the oscillations are filtered out, the plot can be rescaled which makes the drifts better visible). But if the averaging period is set far longer than the duration of these short fluctuations in the trend, the smoothing is too strong and the detection of short fluctuations in the trend fails (a short bulge gets flattened out by smoothing). It is therefore favourable to choose $\Delta t$ as the smallest integer multiple of the prominent short periods. This way, regional fluctuations, e.g., due to geomagnetic activity, in $\dot{a}_{\text{Gauss}}$ can be detected.

To categorise a period as being prominent, a spectral analysis has to be performed. If the amplitude of the period is relatively large compared to other periods in an amplitude spectrum, it may be categorised as a prominent period.

Theoretically, this procedure can also be used to filter out longer term periods. For example, a large amplitude long-term period in $\dot{a}_{\text{Gauss}}$ could cause $\dot{a}_{\text{Gauss}}$ to take on positive values periodically. This would mean that the satellite periodically gains height on average locally, which would not make sense physically and is a false signal. However, for the three aforementioned elements, no such long-term periods, that hindered the analysis and interpretation of results, are encountered.

Originally, a SG filter of arbitrary degree was implemented and used. However, it turns out, that a SG filter of degree 0 sufficiently meets the requirements. A SG filter of degree 0 is equivalent to a moving average filter. For this reason, the implementation of the SG filter is further discussed in Sect. A.3.

## A.2 Determination of an Optimal Period for Smoothing

In addition to condition (63), another (obvious) condition emerges due to the fact, that the data set is finite. The averaging period $\Delta t$ has to be smaller than the duration of the time interval covered by the data:

$$\Delta t < t_K - t_1, \tag{64}$$

where $t_1$ is the starting epoch of the interval and $t_K$ is the end epoch of the interval.

Because the data set is discrete, the integration in Eq. (62) has to be executed numerically. The following statements also hold true for smoothing with a SG filter of any polynomial degree. For the following discussion a data set with equidistant distributed measurements is assumed. Let $\delta t$ be the temporal distance between two measurements, then the averaging period $\Delta t$ has to be an integer multiple of $\delta t$ with $n$ being the integer. At the epoch of the $m$-th measurement the mean variable is

$$\tilde{E}(t_m; \Delta t) = \frac{1}{n} \sum_{k=m-\frac{n-1}{2}}^{m+\frac{n-1}{2}} E(t_k), \qquad \Delta t = n \cdot \delta t. \tag{65}$$

This is only meaningful if $n$ is an uneven integer and greater than 1. Thus, with $n \to 2 \cdot n + 1$, this condition is added to the previous conditions (63) and (64):

$$\Delta t = (2 \cdot n + 1) \cdot \delta t, \qquad n \in \mathbb{N}_+. \tag{66}$$

The following discussion is only relevant, if the second condition in (63) is considered (for the first condition in (63) everything is trivial). Conditions (63) and (66) can not be fulfilled simultaneously if there exists at least one prominent period $\tau$ that is irrational relative to the temporal distance $\delta t$. This problem enforces a weaker condition, which replaces the conditions (63) and (66) by

$$\Delta t = (2 \cdot n + 1) \cdot \delta t = l(\tau) \cdot \tau + \epsilon(\tau) \qquad \forall \tau \in \mathbb{T},\ \forall l(\tau) \in \mathbb{N}_+,\ n \in \mathbb{N}_+,\ \forall \epsilon(\tau) \in \mathbb{R}, \tag{67}$$

where $|\epsilon(\tau)|$ should be small relative to $\delta t$:

$$|\epsilon(\tau)| \ll \delta t. \tag{68}$$

Code was written for both the detection of the set of the prominent periods $\mathbb{T}$ and the automatic determination of $n$.

For the automatic determination of $n$ the algorithm works under the assumption that at least the most prominent period $\tau_0$ (the prominent period with the largest amplitude) is much larger than the temporal distance $\delta t$ between two measurements. First, all the other prominent periods are sorted from highest amplitude to lowest amplitude and a value for $\epsilon_{\max}$, which sets the accuracy of $\Delta t$, is chosen. Then, $l_0$ is established such that $|l_0 \cdot \tau_0 - l_1 \cdot \tau_1| < \epsilon_{\max}$ for $l_1 \in \mathbb{N}_+$. $l_0 \cdot \tau_0$ is some sort of least common multiple of $\tau_0$ and $\tau_1$. Setting $\tau_0 = l_0 \cdot \tau_0$ this process is repeated for the other prominent periods. The process ends when $l_0 \cdot \tau_0$ becomes larger than a maximum predefined value than preferred or no further prominent periods are left to repeat the process with. $\frac{l_0 \cdot \tau_0}{\delta t}$ rounded to the nearest uneven integer then yields $2n$.

## A.3 Savitzky-Golay Filter

The principle behind the SG filter is to assign each time epoch $t_m$ the value of a polynomial $\zeta^{(q)}(t)$ of degree $q$ at the corresponding epoch, where the $\zeta^{(q)}(t)$ is obtained by fitting all data points located inside a window with length $\Delta t$ centered around $t_m$ in a LSA. The filtering process is executed by moving this window. Let us assume for the following discussion that the data set has an equidistant sampling without any data gaps.

According to condition (67) the window contains $2n + 1$ data points. Thus the functional model reads:

$$\vec{F}(\vec{x}) = \begin{pmatrix} \zeta^{(q)}(t_{m-n}) \\ \cdots \\ \zeta^{(q)}(t_m) \\ \cdots \\ \zeta^{(q)}(t_{m+n}) \end{pmatrix} = \begin{pmatrix} x_0 + x_1 t_{m-n} + x_2 t_{m-n}^2 + \cdots + x_q t_{m-n}^q \\ \cdots \\ x_0 + x_1 t_m + x_2 t_m^2 + \cdots + x_q t_m^q \\ \cdots \\ x_0 + x_1 t_{m+n} + x_2 t_{m+n}^2 + \cdots + x_q t_{m+n}^q \end{pmatrix}, \qquad \vec{x} = \begin{pmatrix} x_0 \\ x_1 \\ x_2 \\ \cdots \\ x_q \end{pmatrix} \tag{69}$$

To set-up an efficient scheme which is independent from the concrete location of the filter window, relative units of $\delta t = t_{i+1} - t_i$ shall be used and $t_m$ should be set as the origin $t_m = 0$. The functional model can be written in a linearised form with a design matrix $\boldsymbol{D}$ (in units of $\delta t$) as

$$\vec{F}(\vec{x}) = \boldsymbol{D} \cdot \vec{x}, \qquad \boldsymbol{D} = \begin{pmatrix} 1 & -n & (-n)^2 & \cdots & (-n)^q \\ & & \cdots & & \\ 1 & 0 & 0^2 & \cdots & 0^q \\ & & \cdots & & \\ 1 & n & n^2 & \cdots & n^q \end{pmatrix}. \tag{70}$$

With $\vec{L}$ containing the observations, the parameters are obtained with

$$\vec{x} = \hat{\boldsymbol{D}} \cdot \vec{L}, \qquad \hat{\boldsymbol{D}} = \left(\boldsymbol{D}^{\mathrm{T}} \cdot \boldsymbol{D}\right)^{-1} \cdot \boldsymbol{D}^{\mathrm{T}}. \tag{71}$$

Because $t_m = 0$, the value of the polynomial at $t_m$ is $\zeta^{(q)}(t_m) = x_0$ and therefore only the first row of $\hat{\boldsymbol{D}}$ has to be multiplied as a covector with $\vec{L}$ to obtain the improved value at $t_m$. To apply the SG filter, $\tilde{\boldsymbol{D}}$ has to be evaluated and then applied to each window with center epoch $t_m$, $n < m < K - n$. For the values at epochs $t \in [t_1, \cdots, t_n] \cup [t_{K-n}, \cdots, t_K]$ it is not possible to create such a window. In this work, the improved values at these epochs are obtained by evaluating the polynomial $\zeta^{(0)}(t)$ with its coefficients obtained in a LSA at $t_{n+1}$ and at $t_{K-n-1}$ respectively.

### A.3.1 Smoothing in Results

For GRACE-FO-1 in the year 2018: To determine the optimal smoothing period $\Delta t$, the spectrum of each data set is analysed and the smoothing period is determined according to Sect. A.2 with $\mathbb{T}$ set to contain only the period with the largest amplitude. For all three data sets an optimal smoothing period of $\Delta t = 94.47$ min is evaluated and applied. The spectra of all three $\dot{a}_{\text{Gauss}}$ and all three $\tilde{\dot{a}}_{\text{Gauss}}$ are shown in Fig. 54.

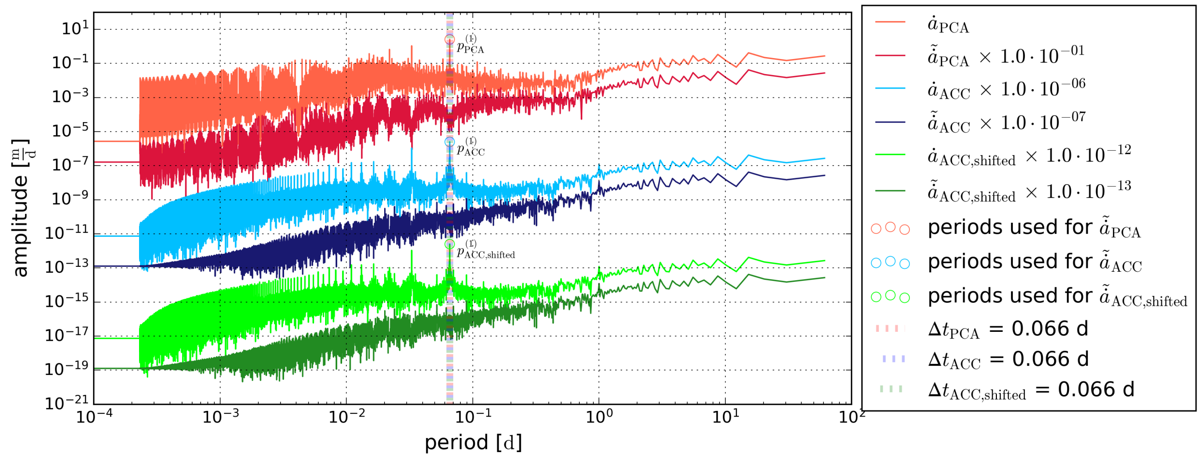

Figure 54: Spectra of $\dot{a}_{\text{Gauss}}$ and $\tilde{\dot{a}}_{\text{Gauss}}$ for all three data sets.

For GRACE-FO-1 in the year 2023: The spectrum of the time series of the slope obtained with the integration approach is shown in Fig. 55. It contains a prominent period $p^{(1)}_{\text{PCA}} = 94.48$ min that is marked in the spectrum. An optimal smoothing period of $\Delta t_{\text{PCA}} = 94.99$ min is evaluated and shown as well. The spectrum of the smoothed slope $\tilde{\dot{a}}_{\text{PCA}}$ is shown as well.

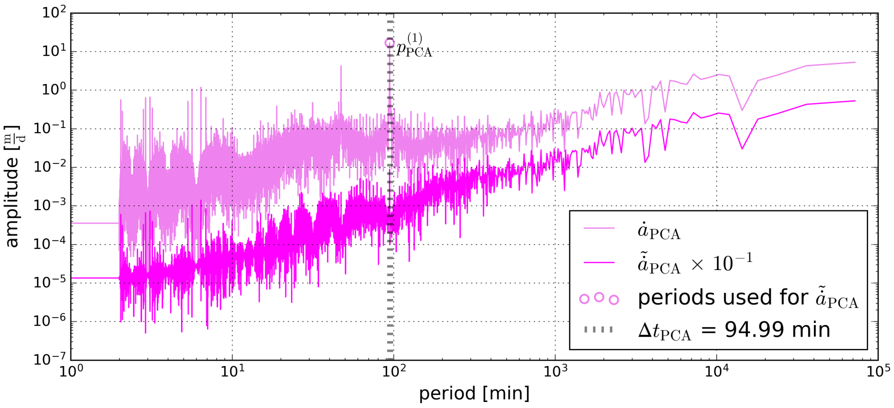

Figure 55: Spectra of $\dot{a}_{\text{Gauss}}$ and $\tilde{\dot{a}}_{\text{Gauss}}$.

For Swarm-A in the year 2023: The spectrum of the time series of the slope obtained with the integration approach is shown in Fig. 56. It contains a prominent period $p_{\mathrm{PCA}}^{(1)} = 93.74\,\mathrm{min}$ that is marked in the spectrum. An optimal smoothing period of $\Delta t_{\mathrm{PCA}} = 92.99\,\mathrm{min}$ is evaluated and shown as well. The spectrum of the smoothed slope $\tilde{\dot{a}}_{\mathrm{PCA}}$ is also shown.

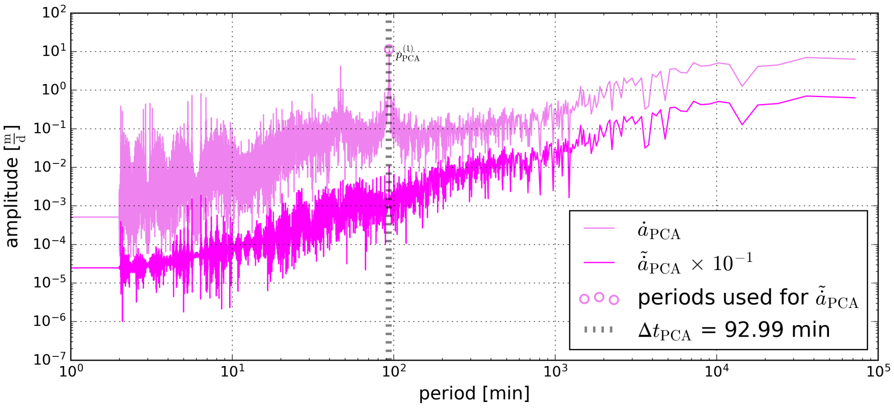

Figure 56: Spectra of $\dot{a}_{\mathrm{Gauss}}$ and $\tilde{\dot{a}}_{\mathrm{Gauss}}$.

For Sentinel-1A in the year 2023: The spectrum of the time series of the slope obtained with the integration approach is shown in Fig. 57. It is heavily distorted due to the MANs not occurring periodically. For this reason, the spectrum of a four day long interval starting at 2023-03-17 is generated. The slope in this interval is denoted as $\overset{\frown}{\dot{a}}_{\mathrm{PCA}}$. Both spectra exhibit similar tendencies below 14.4 min. The spectrum of $\overset{\frown}{\dot{a}}_{\mathrm{PCA}}$ contains a prominent period $p_{\mathrm{PCA}}^{(1)} = 99.30\,\mathrm{min}$. An optimal smoothing period of $\Delta t_{\mathrm{PCA}} = 98.99\,\mathrm{min}$ is evaluated. This smoothing period is also used for the regular $\dot{a}_{\mathrm{PCA}}$. The smoothed spectra of both variables is shown as well. They exhibit similar tendencies already below 57.6 min.

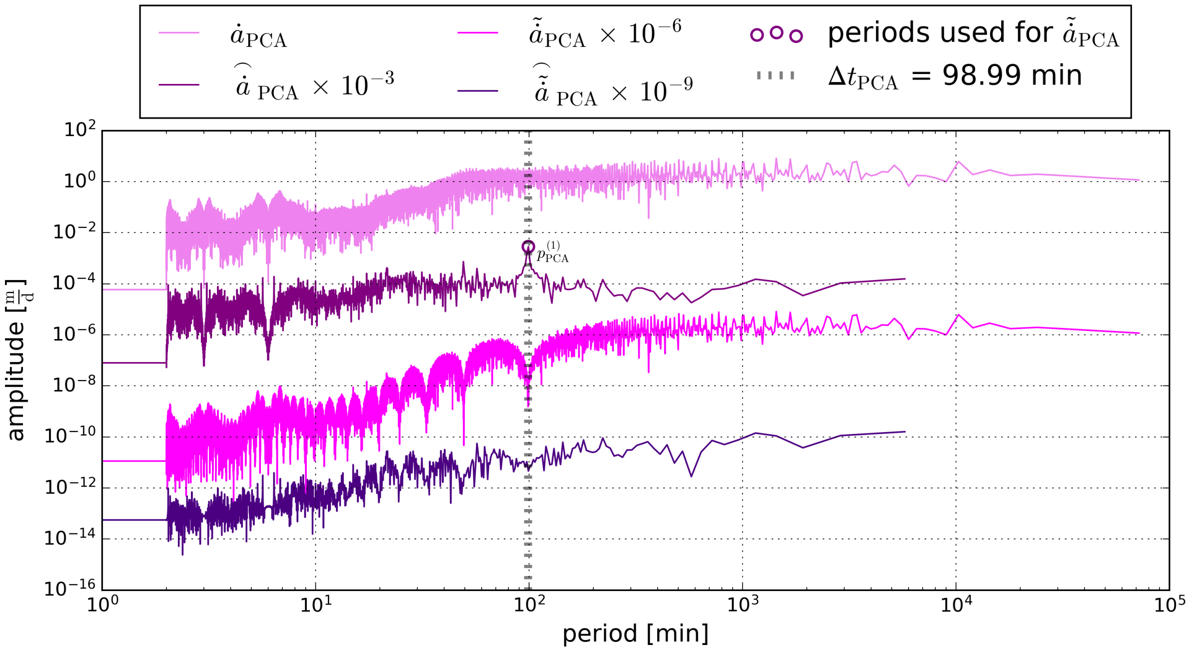

Figure 57: Spectra of $\dot{a}_{\mathrm{Gauss}}$ and $\tilde{\dot{a}}_{\mathrm{Gauss}}$.

For Swarm-A in the year 2024: The spectrum of the time series of the slope obtained with the integration approach is shown in Fig. 58. It contains a prominent period $p_{\mathrm{PCA}}^{(1)} = 94.20\,\mathrm{min}$ that is marked in the spectrum. An optimal smoothing period of $\Delta t_{\mathrm{PCA}} = 94.99\,\mathrm{md}^{-1}$ is evaluated and shown as well. The spectrum of the smoothed slope $\tilde{\dot{a}}_{\mathrm{PCA}}$ is shown as well.

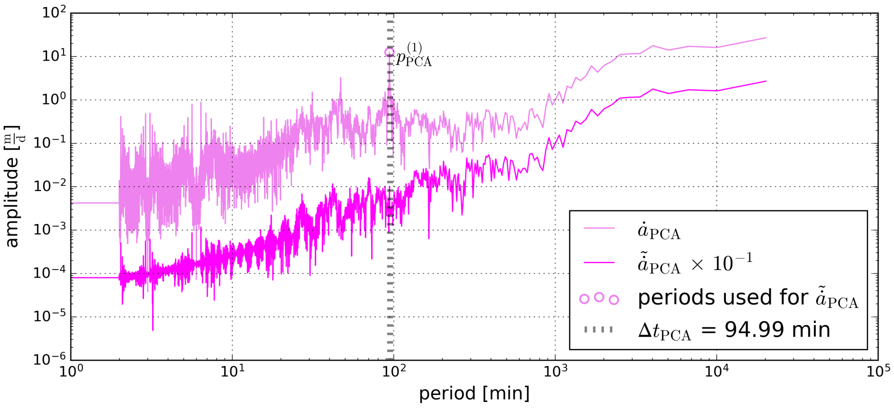

Figure 58: Spectra of $\dot{a}_{\mathrm{Gauss}}$ and $\tilde{\dot{a}}_{\mathrm{Gauss}}$.

For Sentinel-2A in the year 2024: The spectrum of the time series of the slope obtained with the integration approach is shown in Fig. 59. It contains a prominent period $p^{(1)}_{\mathrm{PCA}} = 100.70\,\mathrm{min}$ that is marked in the spectrum. An optimal smoothing period of $\Delta t_{\mathrm{PCA}} = 100.99\,\mathrm{min}$ is evaluated and shown as well. The spectrum of the smoothed slope $\tilde{\dot{a}}_{\mathrm{PCA}}$ is also shown.

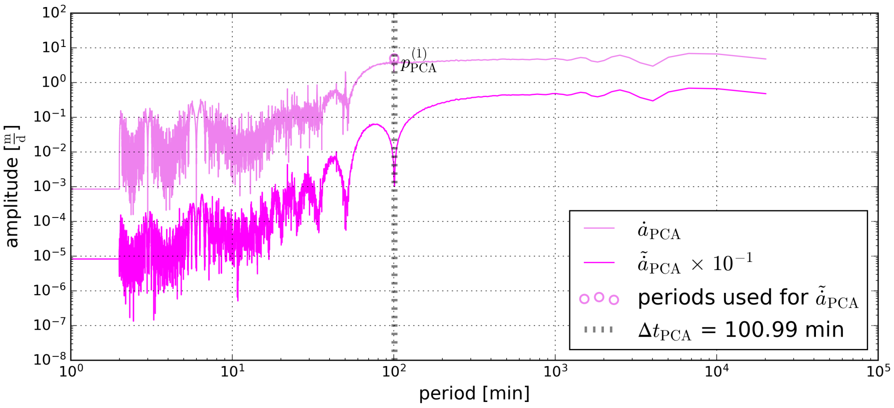

Figure 59: Spectra of $\dot{a}_{\mathrm{Gauss}}$ and $\tilde{\dot{a}}_{\mathrm{Gauss}}$.

For Sentinel-3A in the year 2024: The spectrum of the time series of the slope obtained with the integration approach is shown in Fig. 60. It contains a prominent period $p^{(1)}_{\mathrm{PCA}} = 100.79\,\mathrm{min}$ that is marked in the spectrum. An optimal smoothing period of $\Delta t_{\mathrm{PCA}} = 100.99\,\mathrm{min}$ is evaluated. The spectrum of the smoothed slope $\tilde{\dot{a}}_{\mathrm{PCA}}$ is also shown.

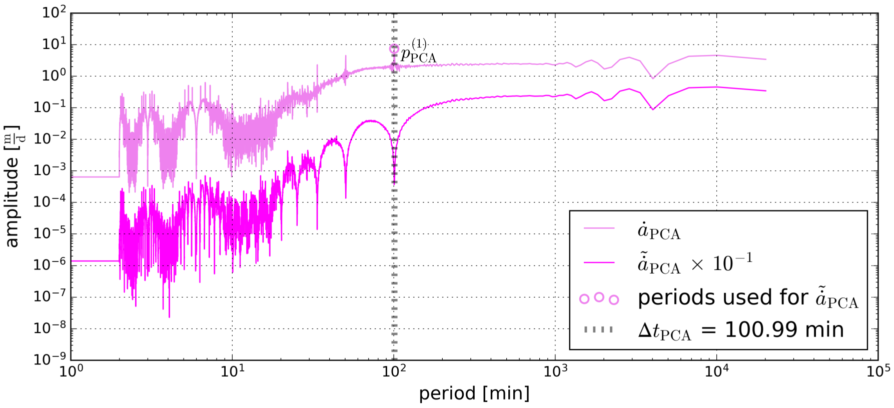

Figure 60: Spectra of $\dot{a}_{\mathrm{Gauss}}$ and $\tilde{\dot{a}}_{\mathrm{Gauss}}$.